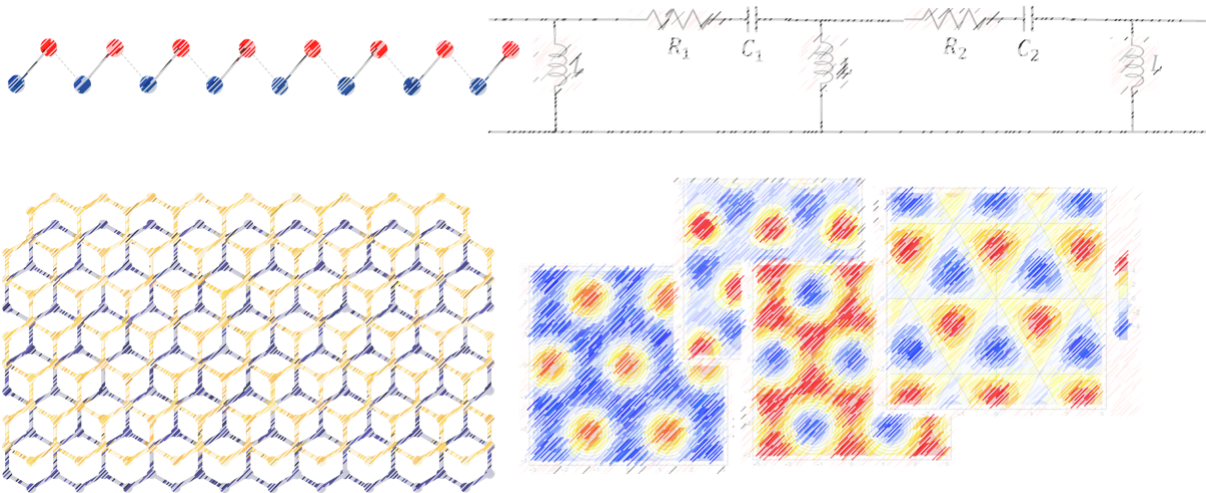UNIVERSIDAD DE ANTIOQUIA

FACULTAD DE CIENCIAS EXACTAS Y NATURALES

INSTITUTO DE FÍSICA

Topological properties of Hermitian and non-Hermitian periodic systems

PHD THESIS

DAVID ANDRÉS GALEANO GONZÁLEZ

Advisor: Dr. Jorge Mahecha

Medellín, july 2021

Universidad de Antioquia

Universidad de Antioquia

Facultad de Ciencias Exactas y Naturales

Instituto de Física

Topological properties of Hermitian and non-Hermitian periodic systems

PhD Thesis

DAVID ANDRÉS GALEANO GONZÁLEZ

Advisor: Dr. Jorge Mahecha

Approved by   Date:.

(Signature)

. . . .

Dr. Jorge Mahecha

(Signature)   *(Signature)*   *(Signature)*

. . . .

Dr. Johans Restrepo   Dr. Rodrigo Acuña   Dr. Melquiades Leyva

Medellín, july 2021

Abstract

In this work we study some topological properties of Hermitian and non-Hermitian periodic systems with physical importance.

For the Hermitian system, we have studied the behavior of 1, 2 and 3 layers of graphene aligned on boron nitride (BN) substrate to analyze how the effective moiré potential and the number of graphene layers affects the Chern number. Our contribution focuses on the calculation of the Chern diagrams of N-layer ($N = 1, 2, 3$) ABC graphene boron nitride moire superlattices, the respective analysis of the potential function and the rol of the pseudomagnetic moiré vector potential to try to find a theoretical explanation for recent experimental results.

It is important to emphasize that our calculations confirm recent results, where the maximum magnitude of the topological invariant (Chern number) coincides with the number of graphene layers. However, the effective moiré potential in the low energy model allows Chern number magnitudes smaller than the number of layers. The Chern diagrams that we calculated have practical importance, because prior to any experimental implementation, the topological properties of the material can be known. This issue is relevant to applications on nano-devices.

On the other hand, the non-Hermitian system that we have studied is new type of Su-Schrieffer-Heeger (SSH) model with complex hoppings, where we propose its correspondence with an electrical circuit model to represent the topological behavior and some quantum properties. Our model can be configured so that the hoppings between sites of the chain are independently parameterized and related to RLC circuit elements, which makes it useful to find and analyze topological properties. Our non-Hermitian circuit model opens the door to new topological material designs based on RLC circuit components.

Keywords

SSH, graphene, moiré patterns, Hermitian, non-Hermitian, topolectric circuits, topology.

To my wife, my mother and all my family and friends for all your support and patience.

Acknowledgements

I would like to thank to:

- Each member of my family, especially my wife Carolina and my mother Olga for their patience and support on this journey.

- My advisor, Dr. Jorge Mahecha, because he was key to successfully completing this project. His advice, guidance and patience were essential to not give up.

- University of Antioquia and especially to the Research Group of "Física Atómica y Molecular" for supporting me academically, and financially for the internship in Korea.

- University of Seoul and especially to Professor Jeil and Postdoc Bheema, for allowing me to do the internship at that university and to get actively involved in their research.

- Professor Ronny Thomale from University of Würzburg for very relevant suggestions in the research.

- Each of the co-authors of the papers published for their contributions and learning.

To all of them, a deep and sincere thanks.   (모두 감사합니다!, Vielen Dank)

Medellín, july 2021

David Andrés Galeano González

Abbreviations

$\boldsymbol{a_i}$	Vector i of Bravais lattice
a_0	Bohr radius
A_μ	μ component of electromagnetic four potential
$\mathcal{A}$	Berry connection
$\boldsymbol{A}$	Vector potential
$\boldsymbol{b_i}$	Vector i of reciprocal lattice
B	Magnetic field
C	Electrical capacitor *or* Chern number
CS	Chern-Simons invariant
$\mathcal{C}$	Chiral operator
d	Physical dimension of the material *or* distance between atoms
D	Physical dimension of a topological defect
D_μ	Covariant derivative
e	Electron charge
E	Energy eigenstate
E_F	Fermi Energy
EP	Exceptional point
F	Berry flux
$\mathcal{F}$	Berry curvature
FK	Fu-Kane invariant
$\boldsymbol{G}_1$	Moiré pattern harmonics
G_m	Moiré reciprocal lattices
H	Hamiltonian
$\mathcal{H}_0$	Bloch Hamiltonian for graphene
H_N^{R}	Remote hopping term corrections for N-layers
H_ξ^M	The scalar moiré potential term
H_A	The vector moiré potential term
I	Electric current
$\mathcal{K}$	Complex conjugation operator
L	Electric inductor
$\mathcal{L}$	Laplacian Matrix
M	Magnetization in a ferromagnet *or* term for inversion-symmetry-breaking on-site in Haldane model
N	Number on unit cells in the crystal *or* number of graphene layers
$N_{-/+}$	Number of bands below/above the Fermi energy

n	Energy levels or Landau levels *or* integer number *or* cell index
n_e	Electron density
P	Spectral projector
$\mathcal{P}$	Particle-hole operator *or* parity operator
q	Charge of a particle
$\boldsymbol{r}$	Position operator
R	Electric resistance
$\mathbf{R}$	Lattice vector
R_A	Anomalous resistance
R_H	Hall resistance
R_0	Ordinary Hall coefficient
S_i	Orbital angular momentum operator in direction i
t_1	Hopping energy between nearest neighbor on different sublattice
t_2	Hopping energy between second neighbor site in the same sublattice
t_{AB}	Intracell hopping energy
t_{BA}	Intercell hopping energy
$\mathcal{T}$	Time reversal operator
$|u_m(\boldsymbol{k})\rangle$	Bloch function
V_H	Hall voltage
WN	Winding number (in text)
Y	Electrical admittance
$\mathcal{Y}$	Admittance matrix
Y_L	Electrical admittance of an inductor branch
Y_{RC}	Electrical admittance of a RC series branch
Z	Impedance
Z_L	Impedance of an inductor L
Z_{RC}	Impedance of a RC series branch
$\mathbb{Z}$	Topological integer number
$\mathbb{Z}_2$	Topological number with only two possible values
α	Rashba term
$\boldsymbol{\beta_i}$	Vector i of second neighbors
$\boldsymbol{\delta_i}$	Vector i of first neighbors
Δ	Mass term *or* gap between bands
$\epsilon_{\mu\nu\rho}$	Order-3 Levi-Civita tensor
$\hbar$	Planck constant
γ	Berry phase
$\boldsymbol{\Gamma}$	Time reversal invariant moment
λ	Number of eigenstates
Λ	Sum of the admittances that converge at each node
μ	Specifies direction in the space where is defined Ψ *or* winding number
ω	Angular frequency *or* normal frequency modes of oscillation
ω_c	The cyclotron frequency
∂S	Loop around which a parallel transport is carried out

ϕ	Phase of elements acquired by t_2 elements in Haldane model *or* electric potential
Φ_0	Quantum flux
Φ	Wannier function
Ψ	Wave function
$\lvert\Psi\rangle$	Eigenvector
ρ_e	Density of the charge carriers
σ_H	Hall conductance
σ_S	Spin Hall conductance
σ_j	j-Pauli matrix, with $j = \{x, y, z\}$
ν	Filling factor
υ_0	Fermi velocity
ξ	Parity eigenvalue from the lowest energy states at the TRIM *or* alignments between the layers of graphene and BN

Contents

Part I

Introduction

Chapter 1

Introduction

Although topology is a branch of mathematics, physicists have found in this branch a way to describe many phenomena. Important theoretical physicists like Thomson, Maxwell, Helmholtz, to name but a few, have used these mathematical concepts for their research [1–3]. The Hall effect, and all its derivations (ordinary, anomalous, quantum, quantum anomalous, spin and quantum spin Hall effects), marked important points in the development of topology in quantum physics [4–7].

Specifically, in condensed matter, topological invariants, such as the first Chern number (or TKNN) [7], has been used to characterize the behavior of bulk, in addition to its relationship with the edge, in what is known in the literature as the bulk edge correspondence.

The study of the Hall effect in all versions, and its theoretical structuring using topological tools, has allowed theorizing and experimenting with new materials, such as topological insulators [8, 9], Weyl semimetals [10], topological superconductors [11], topological spin models [12], magnetic skyrmions [13], vortices [14], topological helium [15], among others.

In this thesis, we will use some theoretical tools of topology to study the behavior of Hermitian and non-Hermitian materials. In the Hermitian Hamiltonian case, we analyzed a structure of graphene sheets aligned with a boron nitride substrate to form moiré patterns. We propose Chern diagrams of great experimental utility for phase transitions and, in addition, we do theoretical analyzes of the way in which moiré potentials affect the topological properties of the material.

For the non-Hermitian case, we take the quantum SSH model (which is Hermitian) and we propose a non-Hermitian classical circuital correspondence that emulates various quantum and topological phenomena. Our model allows us to analyze phase transitions, emulate the skin effect, find new topological invariants and propose a representation that links electrical engineering with materials science.

These works have been presented at two international events (2021 APS March Meeting and 2021 KPS Spring Meeting[1]) and one national event (1st Postgraduate Symposium of the University of Antioquia[2]). In addition, three papers have been published, two of them in Q1 category journals[3].

This report has the following structure. In part II, we do a theoretical background in which we introduce some concepts of topology in physics. Additionally, given the importance of the concept

---

[1]Nominated in the category "Excellent Presentation Prize"
[2]Winner of 1st place in the presentation of the research work
[3]Physical Review B and Science China Physics, Mechanics & Astronomy

of tight-binding in systems that we analyzed, in this part we also make a brief introduction to the subject using some calculations that are made for graphene as an example.

We have divided part III in two. In the first one, we explain the main theoretical and development aspects of the Hermitian model made up of graphene sheets in the boron nitride substrate, whose results are presented in the first section of part IV. Likewise, in the second part of section III, we present the theoretical preliminaries of the non-Hermitian SSH circuit model. Results are presented in the second part of section IV.

Additionally, in section IV we show the summary of three papers published during the development of this thesis and that are related to the results shown here and. Here we also refer to international scientific events where we have shown the results of this work. Finally, we make a summary and an outlook for the results.

Part II

Theoretical background

Chapter 2

Topological concepts in physics

2.1 Continuous deformations and topological equivalence classes

In mathematical topology two objects are equivalent if one of them can be continuously deformed in the other [16]. In physics this concept have been used to explain interesting properties of matter and specifically, some quantum behaviors.

From a topological point of view, there are two kinds of objects: with holes and without holes. Thus, an object with N holes can only be continuously deformed into another with N holes. The number of holes is an example of a topological invariant: a quantity that is maintained despite continuous deformations and only changes when something drastic happens, such as a new hole.

It is important to understand that there is no guarantee that two objects with the same topological invariant belongs to the same equivalence class. Figure 2.1 shows that a circle can be deformed into multiple figures while maintaining the same topological invariant (number of holes). Although all the graphs in Figure 2.1 have a hole (same topological invariant), not all of them belong to the same class: the last figure belongs to a different class from the other three because it is crossed by a thread. Therefore, a topological invariant is a necessary, but not sufficient condition, to ensure that two objects have a common topology [16].

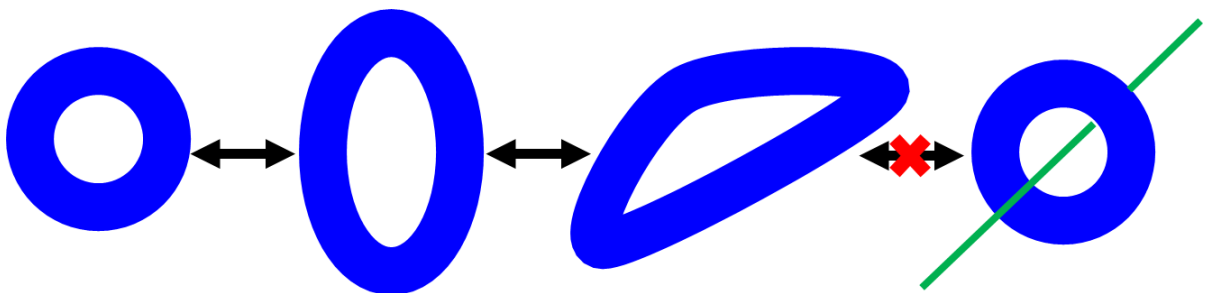Figure 2.1: *All graphs have the same topological invariant (number of holes). The rightmost graph belongs to a different class because it is crossed by a thread that avoid it from being deformed in any of the other three.*

Until now, we have considered that objects are embedded in a three-dimensional space. However, in an N-dimensional space, the classes depend not only on the object but on the space where it is embedded [17].

2.2 Topological invariant in physics

In section 2.1, we exposed an intuitive concept of topological invariance. Here we will make a mathematical description of this concept, and its application in physics.

We will start with the definition of a Hermitian Hamiltonian. A Hamiltonian H is Hermitian if satisfies $H^\dagger = H$ and its eigenvalues are real. A system described by a Hermitian Hamiltonian, evolves in a deterministic way, and if it is time independent, energy is conserved.

A widely used topological invariant is the first Chern number, which is related to the curvature of the complex fiber bundle, whose integral on the manifold allows its calculation [16]. Under the assumption that H is an $n \times n$ matrix and it is Hermitian (and therefore diagonalizable with real eigenvalues), we define a set of n eigenvectors $|\Psi^{(\lambda)}(\boldsymbol{k})\rangle$ for each point in the reciprocal space. Here λ is the index that lists the eigenstates. Next, we will introduce the concept of connection. For this, we consider Ψ as a plane wave

$$\Psi(\boldsymbol{k}, \boldsymbol{r}) = Ce^{i\boldsymbol{k}\cdot\boldsymbol{r}}, \tag{2.1}$$

where $C \in \mathbb{C}$ and $|C|^2 = 1$ [16]. In gauge theory, C becomes a function of $\boldsymbol{r}$ coordinate. Regarding the phase, this is used to introduce the concept of covariant derivative. Therefore, a change of phase α in (2.1) implies a change in the expression of its derivative [16]. Indeed, if

$$\begin{aligned} Ce^{i\boldsymbol{k}\cdot\boldsymbol{r}} &\to Ce^{i\boldsymbol{k}\cdot\boldsymbol{r}-i\alpha(\boldsymbol{r})}, \\ \partial_\mu &\to \partial_\mu + i\partial_\mu\alpha(\boldsymbol{r}) = \partial_\mu + i\mathcal{A}_\mu. \end{aligned} \tag{2.2}$$

Therefore ∂_μ is the partial derivative respect to loops in the planes spanned by arbitrary basis vectors that we called μ, while $D_\mu = \partial_\mu + i\mathcal{A}_\mu$ is known as the covariant derivative and $i\mathcal{A}_\mu = i\partial_\mu\alpha(\boldsymbol{r})$ is the connection.

The formal definition of a connection is beyond the scope of this thesis. It is enough to indicate that a connection can be seen as a quantity that makes zero the covariant derivative of the eigenvectors of H [18]

$$D_\mu|\Psi^{(\lambda)}\rangle = \left(\partial_\mu + i\mathcal{A}_\mu^{(\lambda)}\right)|\Psi^{(\lambda)}\rangle = 0, \tag{2.3}$$

where μ specifies the direction in the space where Ψ is defined. $\mathcal{A}_\mu^{(\lambda)}$ can be written as

$$\mathcal{A}_\mu^{(\lambda)} = -\text{Im}\left(\langle\Psi^{(\lambda)}|\partial_\mu\Psi^{(\lambda)}\rangle\right) \tag{2.4}$$

and it is known as the Berry connection. However, it is possible that the connection can be defined differently from the gradient of a global scalar function: parallel transport around a closed loop can lead to a phase shift [19]. Indeed, from Stokes' theorem, the phase acquired when transported around a loop is calculated as $\int_S \mathcal{F}dS$, where

$$\mathcal{F}_{\mu\nu} = \partial_\mu\mathcal{A}_\nu - \partial_\nu\mathcal{A}_\mu, \tag{2.5}$$

and S is an area element with the loop as boundary. This is called the Berry Curvature and the

phase picked up by the transport around the loop is known as the Berry phase. This is written as

$$\gamma = \int_S \mathcal{F}_{\mu\nu} dS. \tag{2.6}$$

It is important to mention the relationship between the Berry phase and the adiabatic evolution of the system. For the berry phase to be different from zero under adiabatic changes, it is necessary that there is more than one time-dependent parameter in the Hamiltonian and also that the Hamiltonian can generate imaginary or complex eigenfunctions as solutions to the Schrödinger equation. However, more than the explicit dependence of time on the Hamiltonian, what is relevant is a dependence of the Hamiltonian on its parameters. The obtained phase has a contribution from the evolution of the state and from the variation of the eigenstate with the change of the Hamiltonian [16, Sec. 10,6]. The Berry phase can be calculated over a Bloch function $|u_m(\boldsymbol{k})\rangle$ as

$$\gamma_m = \oint i\langle u_m|\boldsymbol{\nabla}_{\boldsymbol{k}}|u_m\rangle \cdot d\boldsymbol{k}. \tag{2.7}$$

When Berry's curvature is multiplied by $i/2\pi$, it becomes what is known as the first Chern class [20]. Considering this factor in (2.6) or (2.7) integrals, such that S is taken to be the whole manifold, the first Chern number is calculated. This is a topological invariant for the fiber bundle. From the Berry phase, the calculation of the Berry flux [21] is immediate as

$$F_m = \boldsymbol{\nabla}_{\boldsymbol{k}} \times i\langle u_m|\boldsymbol{\nabla}_{\boldsymbol{k}}|u_m\rangle. \tag{2.8}$$

There is a Chern number that can be seen as the total Berry flux at the Brillouin zone, or in terms of the Berry curvature,

$$C = \frac{1}{2\pi} \int d^2\mathbf{k} F_m,$$

where C is an integer. However, a natural question arises, under which deformations does the Chern number remain invariant? The answer to this question is that the Chern number remains invariant under small changes of parameters contained in H, i.e. changes which "do not alter the topology of H".

2.3 Topological band theory

Band theory provides a simple explanation of how crystalline materials have electrical insulating behavior, even when electrons jump from one atom to the other. In insulating materials, the insulating band is completely filled and separated by an energy gap from the conduction band. The gap represents the minimum energy to move the electrons from one band to the other. In contrast, conductors are materials with partially filled bands. To introduce the concept of bands, lets suppose the Hamiltonian

$$H = \begin{bmatrix} \Delta & \Xi \\ \Xi^* & -\Delta \end{bmatrix}, \tag{2.9}$$

whose energy eigenvalues are given by $E = \pm\sqrt{|\Xi|^2 + \Delta^2}$. Thus, there are two hybridized states coupled by an interaction of strength Ξ between them and whose two levels are split with an

energy difference 2Δ. At the limit, when $\Delta \to 0$ the hybridization is very strong and keeps the two levels separated by $2|\Xi|$ (complete degeneracy with $\Delta = 0$). On the other hand, when $\Delta \gg \Xi$ the hybridization is negligible and therefore, any coupling between energy levels will tend to split them, especially degenerate ones.

Notwithstanding the aforementioned about the coupling of the bands in the Hamiltonian (2.9), the coupling of the bands is possible through the addition of terms. For example, if we emulate a Zeeman term [22], then $\Delta \to \tilde{\Delta} + |\boldsymbol{k}^2|$, and therefore the energy of (2.9) would be given by

$$E = \pm\sqrt{|\Xi|^2 + (\tilde{\Delta} + |\boldsymbol{k}|^2)^2}. \tag{2.10}$$

However, this is just one example of how a slight modification of the Hamiltonian produces a coupling between the bands.

One of the uses of band theory is to be able to characterize phases of matter. Appealing to the topology concepts developed in Section 2.2, and after this short introduction, we will explore the notion of topological equivalence based on the adiabatic continuity, that is, the system remains in its instantaneous eigenstate if any disturbance acting on it is slow enough [23].

Taking up the concepts with which we started in Section 2.1, two insulators are equivalent if when converting one into the other through an adiabatic deformation in the Hamiltonian, it always remains in the ground state. In other words, if there is an adiabatic path connecting the two insulators along an energy gap that remains finite [24]. If the above is not true, then there is a phase transition.

2.3.1 Bulk-boundary correspondence

Until now, we have talked about classifying systems that have a gap. However, another objective of topological band theory is to characterize gapless states. Besides, the bulk-boundary correspondence talks about the relationship between the topological invariants in the bulk and the edge states.

To understand this concept, we will take the energy (2.10) (from Hamiltonian (2.9) where $\Delta \to \tilde{\Delta} + |\boldsymbol{k}|^2$) and assume that a part of the material has a value $\tilde{\Delta} > 0$ and another part $\tilde{\Delta} < 0$ in direct space, as we illustrate in Figure 2.2. For both, positive and negative values of $\tilde{\Delta}$, there is a gap. According to the magnitude of these values, a Dirac cone can be formed at the interface. That's where the bulk-edge correspondence comes from.

Under the argument presented above, if $\tilde{\Delta} \to \infty$, there is a vacuum at one side and the rest of the material has $\tilde{\Delta} < 0$. Then, in the polarity change of $\tilde{\Delta}$, there will be gapless edge states [21], as we show in Figure 2.3.

Therefore, we can conclude that the bulk-edge correspondence refers to the fact that changing some parameters of the bulk, it gives us information regarding the boundary of the system.

2.3.2 Edge states

While the arguments given in section 2.3.1 about bulk-edge correspondence are correct, they are based on the assumption of a slow change in the sign of $\tilde{\Delta}$, that is, there is no abrupt change in sign. However, what happens if there is an abrupt change in the parameters of the material?.
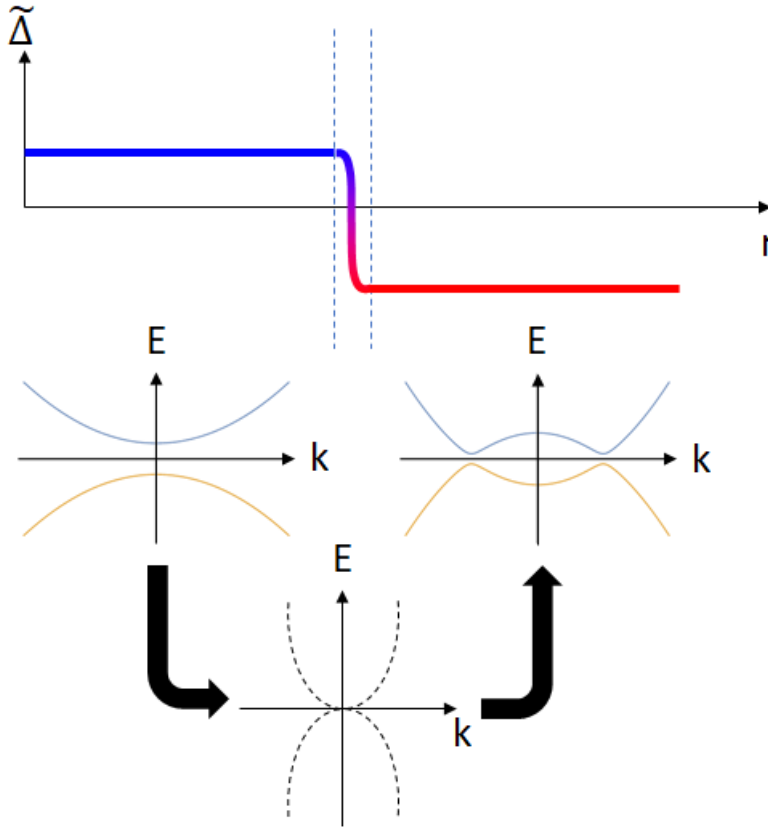
Figure 2.2: *Material with a value $\tilde{\Delta} > 0$ (left side), $\tilde{\Delta} < 0$ (right side) and a Hamiltonian (2.9) where $\Delta \to \tilde{\Delta} + |\mathbf{k}|^2$. At the bottom, we show the corresponding energy bands for $\tilde{\Delta}$ values. With dotted lines we show the interface where there is a slow change in polarity of $\tilde{\Delta}$ (crossing through zero). Dirac cones are formed at the interface.*

To illustrate this, we will assume the Hamiltonian of the Rashba effect [25], with $|\mathbf{k}|^2 = k_x^2 + k_y^2$ and considering a factor α (called as Rashba term) as an experimental factor in a heterojunction [26, 27], then

$$H = \begin{bmatrix} \tilde{\Delta} + k_x^2 + k_y^2 & (k_y + ik_x)\alpha \\ (k_y - ik_x)\alpha & -\tilde{\Delta} - k_x^2 - k_y^2 \end{bmatrix},$$ (2.11)

and the energy is given by

$$E = \pm\sqrt{\alpha^2(k_x^2 + k_y^2) + (\tilde{\Delta} + k_x^2 + k_y^2)^2}.$$

Taking into account Figure 2.3, we assume an interface at $x = 0$, such that $\tilde{\Delta}(x) = \tilde{\Delta}\,\mathrm{sgn}(x)$. For low energy, that is, $k_x^2, k_y^2 \to 0$ and making the Fourier transform in the x direction, we obtain a space and momentum hybrid Hamiltonian,

$$H = \begin{bmatrix} \tilde{\Delta}(x) & \alpha(\partial_x + k_y) \\ -\alpha(\partial_x - k_y) & -\tilde{\Delta}(x) \end{bmatrix}.$$ (2.12)
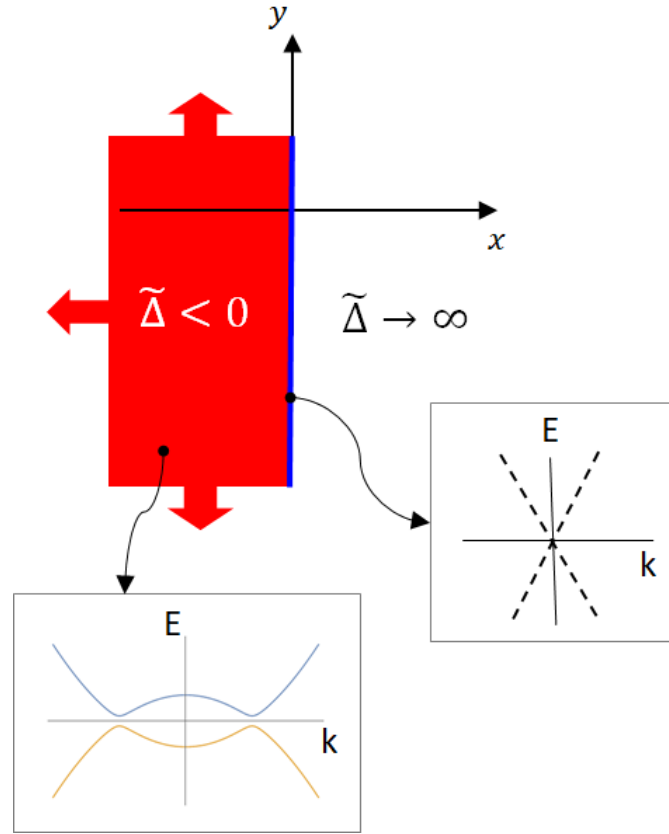
Figure 2.3: *Two-dimensional material with $\tilde{\Delta} < 0$ in the bulk and edge that borders with the vacuum ($\tilde{\Delta} \to \infty$) in $x = 0$. The bands in the bulk maintain a gap between them while at the edge they close in Dirac cones.*

Then, we make a separation of variables $H = H_x + H_y$,

$$H = \begin{bmatrix} \tilde{\Delta}(x) & \alpha\partial_x \\ -\alpha\partial_x & -\tilde{\Delta}(x) \end{bmatrix} + \begin{bmatrix} 0 & \alpha k_y \\ \alpha k_y & 0 \end{bmatrix}.$$

Then, we require that the eigenstate be a zero energy contribution eigenstate of the partial eigenvalue problem $H_x|\Psi\rangle = 0$. The solution of this problem is given by [21, 28]

$$\Psi_{k_y}^{(-)} = \frac{1}{\sqrt{2}} \begin{pmatrix} 1 \\ i \end{pmatrix} e^{-\int_0^x \frac{\tilde{\Delta}(x')}{\alpha} dx'}. \tag{2.13}$$

From equation (2.13), we noticed that if $x > 0$ the integrand is positive and if $x < 0$ the integrand is negative. Thus, the exponential is decreasing as we move away from the edge and therefore, the state is tied to the surface. If we apply this state to H_y, it can be proved that $E(k_y) = -\alpha k_y$, where we can notice that $E(k_y)$ is half of a Dirac cone. On the other hand, the solution

$$\Psi_{k_y}^{(+)} = \frac{1}{\sqrt{2}} \begin{pmatrix} 1 \\ -i \end{pmatrix} e^{\int_0^x \frac{\tilde{\Delta}(x')}{\alpha} dx'} \tag{2.14}$$

is not valid because the integrand increases as we move away from the edge, which makes no physical sense.

26

Therefore, dividing H into H_x and H_y, it can be understood as the sum of a dispersive energy (H_y) and a location energy (H_x). Therefore, the edge states are located at the edge. In section 2.4, we will see that this phenomenon is linked to the Hall effect.

However, changing $\tilde{\Delta}(x) \to \tilde{\Delta}(-x)$ in (2.13), it produces another possible solution with a physical sense. Thus, the other side of the material locates a state where the change in the mass gap occurs in the opposite direction. This is shown schematically in Figure 2.4.
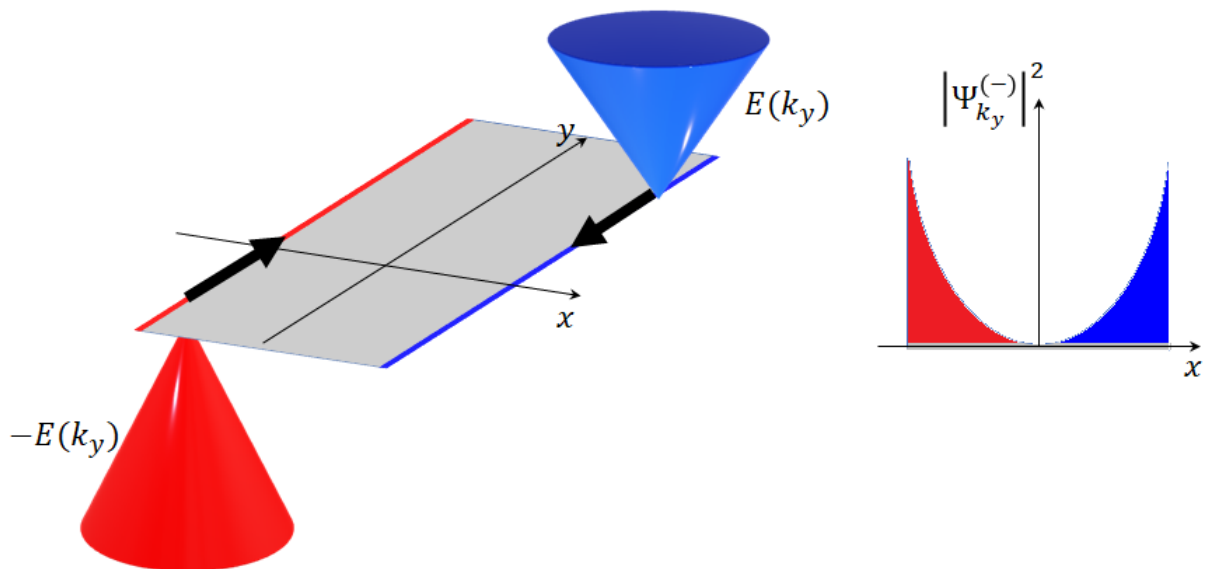

Figure 2.4: *Dispersion in edge states along an infinite strip in the y-direction. (Left) The strip is shown in real space. The two channels exhibit currents in opposite directions with $E(k_y)$ energy in the form of Dirac cones. (Right) Density probability of the $\Psi_{k_y}^{(-)}$ wave function at each edge.*

Therefore, it can be concluded that the system described by the Hamiltonian (2.11) has a spin propagation $\frac{1}{\sqrt{2}}(1, i)^T$ along the edge with dispersion $E(k_y) = -\alpha k_y$. If Hamiltonian $H^*(\boldsymbol{k})$ is considered a spin state $\frac{1}{\sqrt{2}}(1, -i)^T$, it is found with a dispersion relation $E(k_y) = \alpha k_y$.

2.4   Hall effect

The Hall effect is a family of effects that relate charge currents, spin currents, magnetization and magnetic fields in different materials. Each of them, has associated specific topological properties. The first Hall effect was theorized by Edwin Hall [4] in 1879 and is known as the ordinary Hall effect. Later, other Hall effects were discovered. In Table 2.1, we show a summary of those Hall effects and in the following subsections we will delve into each of them.

2.4.1   Ordinary Hall effect

The ordinary Hall effect [4] is a phenomenon in which a transverse potential difference V_H is generated in an electrical conductor when a magnetic field $\boldsymbol{B}$ is applied perpendicular to the surface through which an electric current I circulates, as we show in Figure 2.5.

	Main characteristics	Experimental discovery
Ordinary Hall effect	$B \neq 0$	1879
Anomalous Hall effect	$B = 0,\ M \neq 0$	1880
Quantum Hall effect	$\sigma_H = n\frac{e^2}{h}$	1980 - 1982
Quantum Anomalous Hall effect	$\sigma_H = \frac{e^2}{h}$	2013
Spin Hall effect	$B = 0,\ M = 0$	2004 - 2006
Quantum spin Hall effect	$\sigma_s = \frac{e}{4\pi}$	2007

Table 2.1: *Hall effect classes, main characteristics and year of experimental discovery. B refers to the magnetic field and M to the magnetization in a ferromagnet. σ_H is the Hall conductance and σ_S is the spin Hall conductance [4, 29–33].*
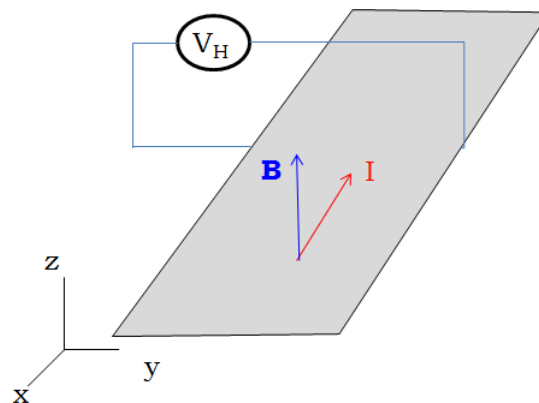

Figure 2.5: *Schematic representation of the Hall effect.*

Thus, the ratio of Hall voltage and electric current is known as the Hall resistance,

$$R_H = \frac{V_H}{I} = \frac{B}{q\rho_e} = R_0 B,$$

where q is the charge of the particle, ρ_e is the density of the charge carriers and R_0 is the ordinary Hall coefficient. Therefore, R_H has units of de m^3/C u $\Omega cm/G$. For later discussions, it is important to note the proportionately between the magnetic field, the Hall voltage, and the Hall resistance.

2.4.2 Anomalous Hall effect

Hall demonstrated that the resistance of ferromagnetic materials or even paramagnetic metals in the presence of an external magnetic field has an additional term [29], given by

$$R_H = R_0 B + R_A M,$$

where M represents the intrinsic magnetization of the material and R_A the anomalous coefficient [34]. Although the phenomenon was not fully understood at the beginning (since it is not explained from the Lorentz law on which the ordinary Hall effect is based), later works [35, 36] showed that this effect is due to the topologic band structure in solids.

In this phenomenon, the electrons acquire an additional group velocity that is parallel to the surface, adding a contribution to the Hall conductance. This phenomenon is also achieved when a paramagnetic material is subjected to an electric field perpendicular to the surface [37].

This phenomenon can have extrinsic or intrinsic origin. The phenomenon is said to be extrinsic due the disorder of spin-dependent scattering of the charge carriers or intrinsic due to the spin-dependent conduction band structure, which can be expressed in terms of the Berry phase. In other words, it is necessary the coupling between the orbital movement of electrons and its spin.

Due to the Lorentz force, the electrons with spin-up deflect in one direction and the electrons with spin-down do so in the other. However, due to the magnetization of the ferromagnetic materials, a charge imbalance will appears between the edges and this produces the anomalous Hall voltage, see Figure 2.6.

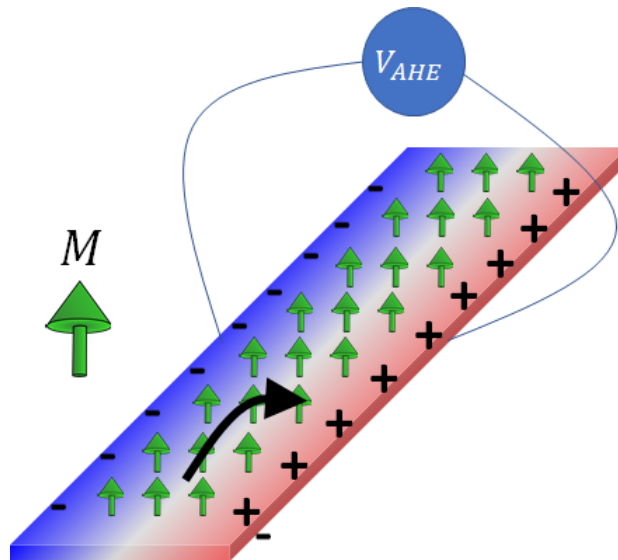Figure 2.6: *Schematic representation of the anomalous Hall effect.*

2.4.3 Quantum Hall effect

To understand the quantum Hall effect, it is important to know that the motion of a charged particle in a uniform magnetic field could be equivalent to a simple harmonic oscillator in quantum mechanics, where the energy levels are quantized as $\left(n + \frac{1}{2}\right)\hbar\omega_c$, with $\omega_c = eB/m$ as the cyclotron

frequency and n as the energy or Landau quantum number. In other words, all the electrons in the bulk are localized and the electrons near the edge form a series of conductive channels [30]. We sketch this effect in Figure 2.7.
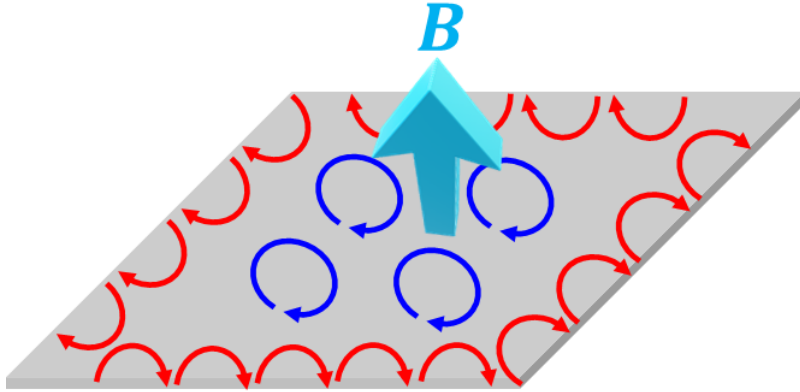

Figure 2.7: *Schematic representation of the quantum Hall effect.*

In 1980 [5] it was experimentally discovered that in a two-dimensional electron gas with a heterojunction subjected to a strong magnetic field, the longitudinal conductance tends to zero while the quantum plateau of the conductance Hall appeared at exact multiples of $\nu e^2/h$, where $\nu = 1, 2, 3, \cdots$ is known as the filling factor. This phenomenon is also known as integer quantum Hall effect and occurs especially in topological insulators [21], i.e, the two-dimensional electron gas configurations, graphene at room temperature [38], GaAs [39], $ZnO-Mg_xZn_{1-x}$ heterostructures [40], among others

An interesting property of ν is that it is insensitive to variations in geometry or interaction between electrons and is defined as a topological invariant [7]. So, if Hall conductance is calculated as $\sigma_H = \nu e^2/h$, the magnetic field takes the value

$$B = \frac{2\pi \hbar n_e}{\nu e^2} = \frac{n_e}{\nu} \Phi_0, \tag{2.15}$$

where n_e is the electron density and $\Phi_0 = 2\pi \hbar/e^2$ is the "quantum of flux". Figure 2.8 shows the relationship between the magnetic field and the quantized Hall resistance $R_H = \sigma_H^{-1}$. Each of the plateaus occurs when the magnitude of the magnetic field takes the value described by the equation (2.15).

Besides, in 1982 [42] it was observed that for larger magnetic fields (greater mobility), quantum plateaus appeared with fractional filling factors $\nu = \frac{1}{3}, \frac{2}{3}, \frac{1}{5}, \frac{2}{5}, \frac{3}{5}, \frac{12}{5} \cdots$. This is known as the fractional quantum Hall effect.

This effect is explained by the electron-electron interaction in addition to the Landau quantization. The quasiparticles in a condensate carry fractional charge $e/3$ due to the strong Coulomb interaction. Today, it is widely accepted that the fractional quantum Hall effect is a topological quantum phase of composed fermions, which breaks the time reversal symmetry [43].
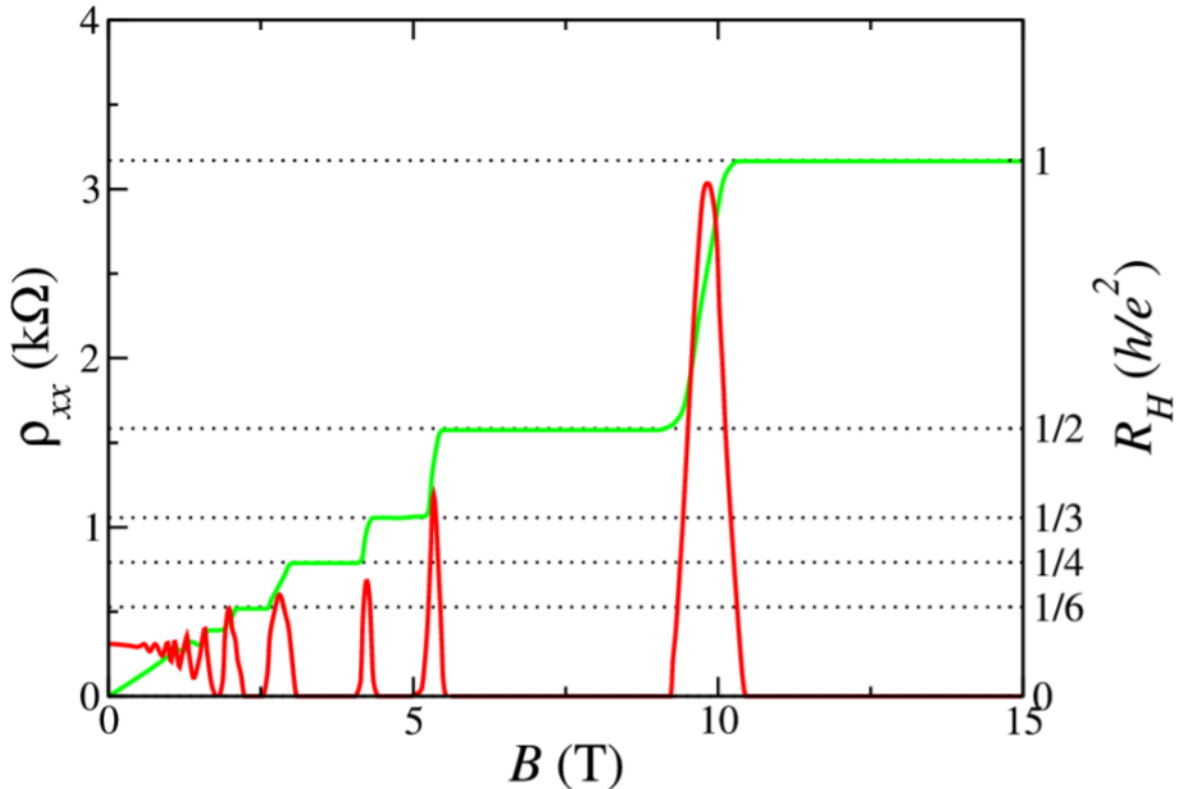
Figure 2.8: *Integer quantum hall effect. Magnetic field (B) in Teslas (T). The red line shows the longitudinal resistivity as a function of the magnetic field. This longitudinal resistivity spikes when there is a level change in the Hall resistivity (green line). Image source: [41]*

2.4.4 Quantum anomalous Hall effect

A very important theoretical description of this effect was carried out by Haldane, who demonstrated that the integer quantum Hall effect can be presented in a lattice of spinless electrons in the presence of a magnetic flux. Although the total magnetic flux is zero, the electrons form a conducting edge channel [31]. Because this effect occurs without an external magnetic field, the Hall conductance originates from the band structure of the electrons in the lattice rather than from the discrete Landau levels in the strong magnetic field. The Figure 2.9 shows a diagram that represents the quantum anomalous Hall effect.

The anomalous Hall conductance is expressed in terms of the integral of the Berry curvature over the moment space or by means of the Chern number. This effect was first observed experimentally in 2013 at Tsinghua University with thin films of chromium-doped $(Bi,Sb)_2Te_3$, a magnetic topological insulator with strong spin-orbit coupling [44].

2.4.5 Spin Hall effect

This phenomenon was proposed by the Dyakonov and Perel in 1971 [32, 45]. Unlike the Hall anomalous effect in which the resistance vanishes in the absence of a magnetic field or without the magnetization in a paramagnetic metal, in this phenomenon the spin-dependent deflected motion of particles may still be an observable effect, as we show in Figure 2.10.

The spin Hall effect occurs when there is a Zeeman splitting and a spin-orbit coupling that allow
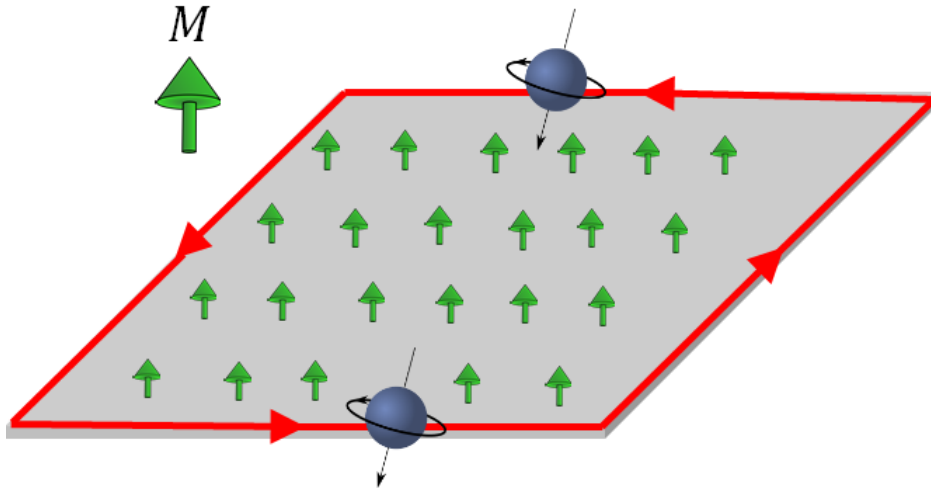
Figure 2.9: *Schematic representation of the quantum anomalous Hall effect*

a resonant spin effect, in which small currents can induce finite spin current and spin polarization. In other words, this phenomenon refers to the accumulation of spins at the border of a conductor that carries electrical current for which the sign of the spin at one border will be opposite to the spin at the opposite border.

This phenomenon has been widely theorized in graphene films, although the low spin-orbit coupling makes difficult to detect it experimentally. In Figure 2.10, we show schematically the spin Hall effect and the inverse spin Hall effect. In the first one, a charge current circulates through a two-dimensional material with the appropriate topological characteristics (such as graphene). It is divided into two spins, and accumulates it in each edge. Thus, a spin current transverse to the charge current is generated.

In the inverse spin Hall effect, a spin current flows through a two-dimensional material and due to its topological configuration, a transverse charge current circulation occurs. Due to charge flow, the charges at each edge of the material are separated, as shown on the right side of Figure 2.10. In 2003, spin-orbit coupling in electron band structure was experimentally observed and it was evident that it was the cause of the effect [46,47]. Later experimental work has realized the effect, in semiconductors such as GaAs, InGaAs [48] and heterostructures of (Al,Ga)As/GaAs [49].

The spin Hall effect is also present in geometries other than 2D. Specifically, it has been observed in 3D bulk states of the Bi_2Te_2Se platelets [50] and, in general, in metal and semiconductor systems with spin-orbit coupling [51,52].

2.4.6 Quantum spin Hall effect

This effect is the quantum version of the spin Hall effect or the spin version of the quantum Hall effect. Thus, this effect can be seen as the combined version of two quantum anomalous Hall effects of spin up and spin down, as shown in Figure 2.11. A fundamental aspect of this effect is that there are spin-dependent edge states with spin-up electrons moving in one direction while spin-down electrons move in the opposite direction, forming a pair of helical edge states.

An important aspect to highlight is that this effect does not have charge Hall conductance, but a spin Hall conductance different from zero. The theoretical explanation for this effect was
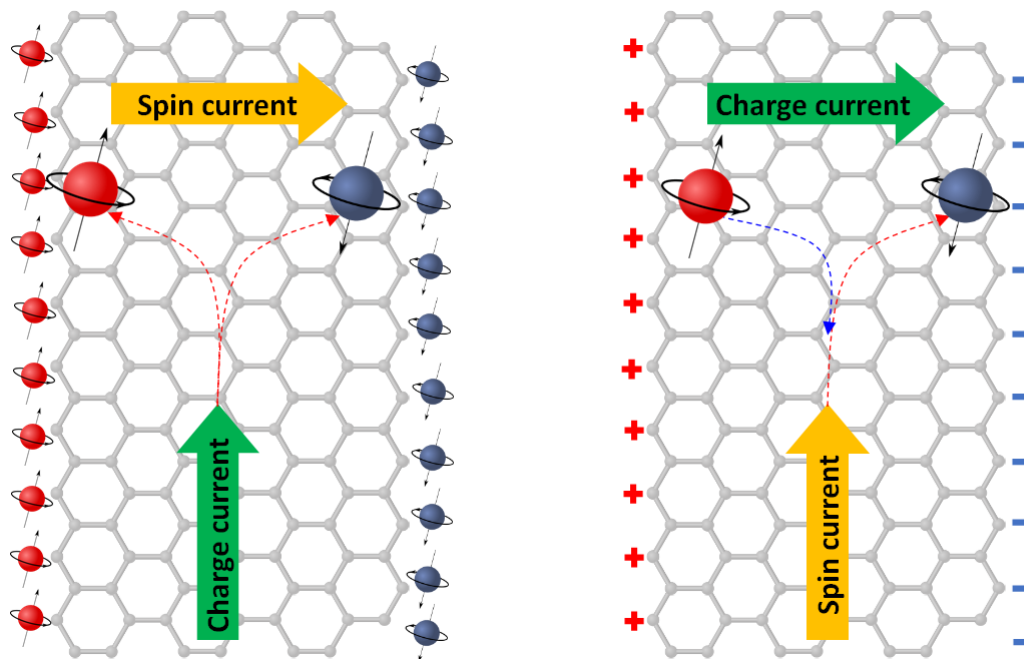
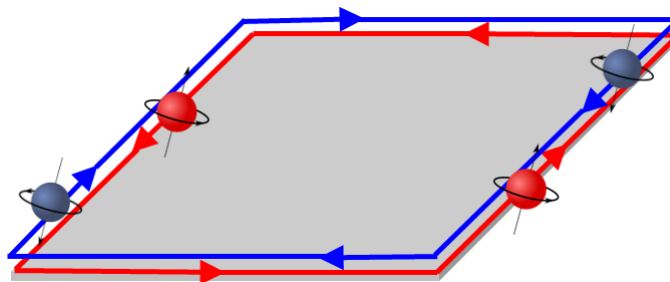Figure 2.10: *Schematic representation of the spin Hall effect (left) and inverse spin Hall effect (right)*

Figure 2.11: *Schematic representation of the quantum spin Hall effect*

provided by Kane and Mele [33] in 2005, when they generalized Haldane's model as a lattice with 1/2 spin electrons and a strong spin-orbit coupling that replaces periodic magnetic flux in the Haldane model.

The time reversal symmetry (see Sec. 2.5.1) is preserved in this effect and the edge states are robust against impurities or disorders due to the fact that electron backscattering in the two edge channels is prohibited due to symmetry.

Because the low spin-orbit coupling in graphene, the phenomenon is difficult to observe experimentally, however, in 2006 it was experimentally tested in a CdTe/HgTe/CdTe quantum well [53].

From the theoretical description and subsequent experimental confirmation of this effect, variations have been proposed, such as the topological Anderson insulator, in which all the electrons in the bulk are located by impurities, while a pair of conductive helical edge channels is formed [54]. Similarly, strong Coulomb interaction can cause the quantum spin Hall effect in Mott insulator [55].

2.5 Topological symmetries

Near absolute zero temperature, the matter presents exotic behaviors related with the quantum entanglement that have been theoretically described as quantum phases of matter. Physicists considered that with the help of Landau's symmetry-breaking theory [56], all the possible quantum phases of matter and its transitions can be described [57].

However, some works of the late 80's and early 90's identified a chiral spin state that breaks the parity and time reversal symmetry. Therefore Landau's symmetry-breaking theory was not enough to explain the quantum phases [58, 59].

There are spatial and non-spatial symmetry topological protected modes. Since non-spatial symmetries have boundary modes that are topologically protected, we are interested on this kind of symmetries that are basically summarized in time reversal symmetry, particle-hole symmetry and chiral symmetry [60]. From now on, for each m band we consider Bloch states that are eigenstates of the Bloch Hamiltonian $H(\boldsymbol{k})$ [61]

$$H(\boldsymbol{k})|u_m(\boldsymbol{k})\rangle = E_m(\boldsymbol{k})|u_m(\boldsymbol{k})\rangle. \tag{2.16}$$

The two-band model provides a useful tool to describe the physics of each of the topological classes. Therefore, we will use the 2×2 Bloch Hamiltonian [62]

$$H(\boldsymbol{k}) = d_0(\boldsymbol{k})I + d_x(\boldsymbol{k})\sigma_x + d_y(\boldsymbol{k})\sigma_y + d_z(\boldsymbol{k})\sigma_z, \tag{2.17}$$

where I is the 2×2 matrix identity, σ_i, $i = x, y, z$ are the Pauli matrices, and d_i, $i = 0, x, y, z$ are the related functions of $\boldsymbol{k}$ vector.

2.5.1 Time-reversal symmetry (TRS)

First, we introduce the antiunitary time reversal (TR) operator $\mathcal{T}$. If we consider a vector $|\Psi\rangle$, we say that $\mathcal{T}|\Psi\rangle$ is the time-reversed state. A system exhibits TR symmetry if $\mathcal{T}$ commutes with the Hamiltonian, $[H, \mathcal{T}] = 0$ [63]. It is easy to verify that $\mathcal{T}^2 = -1$ for half-integer spins system and it implies double degeneracy (Kramers theorem) [61, Appendix A]. If $\mathcal{T}^2 = 1$ it means a integer spin system and all entries of the Hamiltonian are real.

Specifically, in 1/2-spin system, $\mathcal{T} = i\sigma_y\mathcal{K} = e^{-i\pi S_y/\hbar}\mathcal{K}$ [63, Appendix B], where $\mathcal{K}$ is the complex conjugation, $S_y = (\hbar/2)\sigma_y$ is the spin angular momentum operator and σ_y is the y-Pauli matrix. In band theory [64, 65]

$$\mathcal{T}H(\boldsymbol{k})\mathcal{T}^{-1} = H(-\boldsymbol{k}). \tag{2.18}$$

Therefore, for a 2×2 general Hamiltonian defined by (2.17), the fulfillment of the time-reversal symmetry, as we expressed it in equation (2.18), implies that $d_0(\boldsymbol{k}) = d_0(-\boldsymbol{k})$ (symmetric function) and $d_i(\boldsymbol{k}) = -d_i(-\boldsymbol{k})$ (antisymmetric function) where $i = \{x, y, z\}$. The eigenvalues and normalized eigefunctions of Hamiltonians $H(\boldsymbol{k})$ that present this kind of symmetry are, respec-

tively,

$$E_\pm = d_0 \pm \sqrt{d_x^2 + d_y^2 + d_z^2} \quad \text{and} \quad \Psi_\pm = \begin{bmatrix} \frac{\sqrt{\frac{1}{2} - \frac{d_z}{2\sqrt{d_x^2+d_y^2+d_z^2}}}\left(\sqrt{d_x^2+d_y^2+d_z^2}+d_z\right)}{d_x+id_y} \\ \sqrt{\frac{1}{2} - \frac{d_z}{2\sqrt{d_x^2+d_y^2+d_z^2}}} \end{bmatrix}. \tag{2.19}$$

2.5.2 Particle-hole symmetry (PHS)

The particle-hole operator $\mathcal{P}$ is anti-unitary and anti-commutes with the Hamiltonian, it is to say $[H,\mathcal{P}] \neq 0$. The particle-hole symmetry can be expressed as [64,65]

$$\mathcal{P}H(\boldsymbol{k})\mathcal{P}^{-1} = -H(-\boldsymbol{k}), \tag{2.20}$$

where in the two-bands model approximation, $\mathcal{P} = \sigma_x\mathcal{K}$ with $\mathcal{K}$ the complex conjugation operator. It is easy to verify that $\mathcal{P}^2 = \pm 1$ if there is a particle-hole symmetry. The $\mathcal{P}^2$ sign means the winding number (w) is clockwise ($-$) or counterclockwise ($+$) direction [63]. In two band model, it has PHS if $d_z(\boldsymbol{k}) = d_z(-\boldsymbol{k})$ (symmetric function) and $d_i(\boldsymbol{k}) = -d_i(-\boldsymbol{k})$ (antisymmetric function) where $i = \{0, x, y\}$.

2.5.3 Chiral symmetry (CS)

The chiral operator $\mathcal{C}$ is a unitary operator which anti-commutes with the Hamiltonian, it is to say, $[H,\mathcal{C}] \neq 0$. It is important to note that combining TRS with PHS yields a chiral symmetry [65,66]. If there is chiral symmetry, then $\mathcal{C}^2 = 1$.

If $\mathcal{C} = \mathcal{T} \cdot \mathcal{P}$, then it is easy to prove that

$$\mathcal{C}H(\boldsymbol{k})\mathcal{C} = -H(\boldsymbol{k}), \tag{2.21}$$

where it follows that

$$\mathcal{C} = \begin{bmatrix} 1 & 0 \\ 0 & -1 \end{bmatrix}, \tag{2.22}$$

and therefore, the Hamiltonian

$$H_{CS} = \begin{bmatrix} 0 & -d_x(\boldsymbol{k}) \\ -d_x(\boldsymbol{k}) & 0 \end{bmatrix} \tag{2.23}$$

has the CS and his eigenvalues are $E_\pm = \pm d_x(\boldsymbol{k})$, and its autofunctions are

$$\Psi_\pm = \begin{bmatrix} \mp 1 \\ 1 \end{bmatrix}. \tag{2.24}$$

2.5.4 Relationship between topological invariants and symmetries

We define a quantity s as even if the Hamiltonian has non-chiral symmetry or odd if the Hamiltonian has chiral symmetry. In Table 2.2 we summarize the topological invariants in relation

to the presence (s is odd) or absence (s is even) of chiral symmetry.

The presence of topological defects [67] in a material allows to characterize the presence or absence of symmetries related to spatial adiabatic variations for a topological classification of the material [68] according to the Altland-Zirnbauer symmetry classes [69]. Although in this work we will not delve into the topic of topological defects, it is important to know that from now on d-dimension refers for the dimension of the material and D-dimension for the dimension of a topological defect. Also, it is important to say that in Table 2.2 $\mathbb{Z}$ means a topological integer number $(0, \pm 1, \pm 2, \cdots)$ and $\mathbb{Z}_2$ denotes a topological number with only two possible values: $\mathbb{Z}_2 = \{0, 1\}$ or $\mathbb{Z}_2 = \pm 1$. However, the topological numbers $\mathbb{Z}_2$ have two classes that are called "descendants", which we will explain later.

	$\mathbb{Z}$	$\mathbb{Z}_2^{(1)}$	$\mathbb{Z}_2^{(2)}$
Non-Chiral	CN	CS	FK
Chiral	WN	FK	CS

Table 2.2: *Topological invariants for chiral and non-chiral symmetries where CN: Chern number, CS: Chern-Simons invariant, FK: Fu-Kane invariant, WN: winding number.*

Chern number invariant

As we show in Table 2.2, the Chern number is used in gapped topological phases and non-chiral classes. It is important to note that it is only defined when $d + D$ is even [70]. If $\delta = d - D = 2n + 2, (n = 0, 1, 2, \cdots)$ the $(n+1)$th Chern number is defined in terms of the Berry curvature as [64]

$$C_{n+1} = \int_{BZ^d \times M^D} \frac{1}{(n+1)!} \text{Tr} \left(\frac{i\mathcal{F}}{2\pi} \right)^{n+1} \in \mathbb{Z}. \tag{2.25}$$

In two-dimensional lattice with $D = 0$, it is defined in the mth band

$$C_1 = \frac{i}{2\pi} \int_{BZ^2} \mathcal{F}_m(\boldsymbol{k}) d\boldsymbol{k}, \tag{2.26}$$

and this is the Thouless, Kohomoto, Nightingale and den Nijs (TKNN) integer [7]. This Chern number gives the quantized Hall conductance σ_H. This invariant has a special characteristic, it defines a class of materials called *"Chern insulators"*: a two-dimensional material with non-zero Chern number and without net magnetic field. This material class exhibit the quantum anomalous Hall effect explained in section 2.4.4.

Winding number invariant

The winding number can be defined only in presence of chiral symmetry. In chiral symmetry $N_+ = N_-$, where $N_{-/+}$ are the number of bands below/above the Fermi energy. If $d + D = 2n + 1$, the winding number μ, is defined as [70]

$$\mu_{2n+1}[k] = \int_{BZ^d \times M^D} \frac{(-1)^n n!}{(2n+1)!} \left(\frac{i}{2\pi} \right)^{n+1} \text{Tr} \left[\left(\frac{dk}{k} \right)^{2n+1} \right]. \tag{2.27}$$

Specifically, when $d = 1$ and $D = 0$ it is shown that

$$\mu_0 = \frac{1}{2\pi} \int_{-\pi}^{\pi} \left(k \frac{\boldsymbol{d}(k)}{|\boldsymbol{d}(k)|} \times \frac{d}{dk} \frac{\boldsymbol{d}(k)}{|\boldsymbol{d}(k)|} \right)_z dk, \tag{2.28}$$

where $\boldsymbol{d}(\boldsymbol{k})$ represents the bulk momentum-space Hamiltonian as $H = \boldsymbol{d}(k) \cdot \boldsymbol{\sigma}$. The winding number is related to the number edge of states in the SSH model [28].

Chern-Simons invariant

In general terms, this is a not quantized invariant (unlike Chern number) and it is defined when $d + D$ is odd. Mathematically, it is defined as [71]

$$CS_{2n+1}[\mathcal{A}] = \frac{1}{n!} \left(\frac{i}{2\pi} \right)^{n+1} \int_{BZ^d \times M^D} \int_0^1 dt \mathrm{Tr}(\mathcal{A}\mathcal{F}_t^n), \tag{2.29}$$

with $n = (d + D + 1)/2$ and $\mathcal{F}_t = td\mathcal{A} + t^2\mathcal{A}^2 = t\mathcal{F} + (t^2 - t)\mathcal{A}^2$. In Table 2.2 we can see that CS invariant apply in chiral and non-chiral symetries with different descendants [70].

For CS-First descendant ($\mathbb{Z}_2^{(1)}$), the result of (2.29) is a number such that, if $CS_{2n+1} \in \mathbb{Z}$ then the $\mathbb{Z}_2$ topology is trivial, but if $CS_{2n+1} \in \frac{1}{2}\mathbb{Z}$ the topology is non-trivial.

The CS-second descendant ($\mathbb{Z}_2^{(2)}$) is typical of systems that exhibit chiral symmetry. As the first descendant, the CS-second descendant $\mathbb{Z}_2^{(2)}$ is given by $CS_{2n+1} \in \mathbb{Z}$. Specifically, it is said that $\mathbb{Z}_2$ is trivial if CS_{2n-1} is even and non-trivial if CS_{2n-1} is odd.

Fu-Kane invariant

If we assume $N_{-/+}$ as the number of bands below/above the Fermi energy and the set of filled Bloch wavefunctions as $\{|u^\alpha(\boldsymbol{k})\rangle\}$ where $\alpha = 1, 2, \cdots, N_\pm$, then, we define the *spectral projector* as [70]

$$P(\boldsymbol{k}, \boldsymbol{r}) = \sum_{\alpha=1}^{N_-} |u^\alpha(\boldsymbol{k}, \boldsymbol{r})\rangle\langle u^\alpha(\boldsymbol{k}, \boldsymbol{r})|, \tag{2.30}$$

and the Q-Matrix by

$$Q(\boldsymbol{k}, \boldsymbol{r}) = 1 - 2P(\boldsymbol{k}, \boldsymbol{r}), \tag{2.31}$$

where $q(\boldsymbol{k}, \boldsymbol{r})$ are the unit matrices that make up $Q(\boldsymbol{k}, \boldsymbol{r})$. Taking the above, the Fu-Kane invariant is defined in terms of Berry curvature as [72]

$$FK_n = \frac{1}{n!} \left(\frac{i}{2\pi} \right)^n \int_{BZ_{1/2}^d \times M^D} \mathrm{Tr}(\mathcal{F}^n) - \oint_{\partial BZ_{1/2}^d \times M^D} Q_{2n-1} \tag{2.32}$$

with $n = (d + D)/2$.

As it is shown in Table 2.2, the FK invariant has two descendants. The FK-first descendant ($\mathbb{Z}_2^{(1)}$) is isomorphically to the $\mathbb{Z}_2^{(2)}$ descendant in non-chiral classes [70]. These descendants can be written as [72,73]

$$FK = \prod_K \frac{\mathrm{Pf}[\tilde{w}(K)]}{\sqrt{\det[\tilde{w}(K)]}}, \tag{2.33}$$

where K runs over the dimensional TR fixed momenta and the components α and β of $\tilde{w}(K)$ are given by

$$\tilde{w}^{\alpha\beta}(k,r) = \langle u^\alpha(-k,r)|\mathcal{T}u^\beta(k,r)\rangle = \text{constant}, \qquad (2.34)$$

and $|u^{\alpha,\beta}\rangle$ are the Bloch wavefunctions. Fu and Kane [72] show that if $FK = 1$ the phase is trivial and $FK = -1$ the phase is topological.

2.5.5 Topological classification

Taking into account that the square value of the symmetry operators take the values $\mathcal{T}^2 = \pm 1$, $\mathcal{P}^2 = \pm 1$ and $\mathcal{C}^2 = 1$, in Table 2.3 we show the symmetry classes for different δ-dimensions, where $\delta = d - D$, that are related to topological invariants. In this table, there is a division between cases A and AIII with the other cases. This is because the Hamiltonian of the symmetries A and AIII are complex symmetry classes (The complex symmetry classes do not have TRS nor PHS), whereas the Hamiltonians of the other symmetries belongs to real symmetry classes.

s	Class	$\mathcal{C}$	$\mathcal{P}$	$\mathcal{T}$	Spin	Dyson Name	Topological invariant	$\delta=0$	1	2	3	4	5	6	7
	A				I or HI	chiral unitary	$\mathbb{Z}\to$CN	$\mathbb{Z}$		$\mathbb{Z}$		$\mathbb{Z}$		$\mathbb{Z}$	
	AIII	1			I or HI	unitiary	$\mathbb{Z}\to$WN		$\mathbb{Z}$		$\mathbb{Z}$		$\mathbb{Z}$		$\mathbb{Z}$
0	AI			1	I	orthogonal	$\mathbb{Z}\to$CN, $\mathbb{Z}_2^{(1)}\to$CS, $\mathbb{Z}_2^{(2)}\to$FK	$\mathbb{Z}$				$2\mathbb{Z}$		$\mathbb{Z}_2^{(2)}$	$\mathbb{Z}_2^{(1)}$
1	BDI	1	1	1	I	chiral orthogonal	$\mathbb{Z}\to$WN, $\mathbb{Z}_2^{(1)}\to$FK, $\mathbb{Z}_2^{(2)}\to$CS	$\mathbb{Z}_2^{(1)}$	$\mathbb{Z}$				$2\mathbb{Z}$		$\mathbb{Z}_2^{(2)}$
2	D		1		I or HI	BdG	$\mathbb{Z}\to$CN, $\mathbb{Z}_2^{(1)}\to$CS, $\mathbb{Z}_2^{(2)}\to$FK	$\mathbb{Z}_2^{(2)}$	$\mathbb{Z}_2^{(1)}$	$\mathbb{Z}$				$2\mathbb{Z}$	
3	DIII	1	1	-1	HI	BdG	$\mathbb{Z}\to$WN, $\mathbb{Z}_2^{(1)}\to$FK, $\mathbb{Z}_2^{(2)}\to$CS		$\mathbb{Z}_2^{(2)}$	$\mathbb{Z}_2^{(1)}$	$\mathbb{Z}$				$2\mathbb{Z}$
4	AII			-1	HI	symplectic	$\mathbb{Z}\to$CN, $\mathbb{Z}_2^{(1)}\to$CS, $\mathbb{Z}_2^{(2)}\to$FK	$2\mathbb{Z}$		$\mathbb{Z}_2^{(2)}$	$\mathbb{Z}_2^{(1)}$	$\mathbb{Z}$			
5	CII	1	-1	-1	HI	chiral symplectic	$\mathbb{Z}\to$WN, $\mathbb{Z}_2^{(1)}\to$FK, $\mathbb{Z}_2^{(2)}\to$CS		$2\mathbb{Z}$		$\mathbb{Z}_2^{(2)}$	$\mathbb{Z}_2^{(1)}$	$\mathbb{Z}$		
6	C		-1		I or HI	BdG	$\mathbb{Z}\to$CN, $\mathbb{Z}_2^{(1)}\to$CS, $\mathbb{Z}_2^{(2)}\to$FK			$2\mathbb{Z}$		$\mathbb{Z}_2^{(2)}$	$\mathbb{Z}_2^{(1)}$	$\mathbb{Z}$	
7	CI	1	-1	1	I	BdG	$\mathbb{Z}\to$WN, $\mathbb{Z}_2^{(1)}\to$FK, $\mathbb{Z}_2^{(2)}\to$CS				$2\mathbb{Z}$		$\mathbb{Z}_2^{(2)}$	$\mathbb{Z}_2^{(1)}$	$\mathbb{Z}$

Table 2.3: *Altland-Zirnbauer (AZ) symmetry classes.* $\delta = d - D$ *where d is the space dimension and D is the dimension of defects. If* $D = 0$ *it corresponds to the tenfold classification of gapped bulk topological insulators and superconductors [69]. The superscript of* Z_2 *means the descendant. In the column titled spin, "I" means integer and "HI" means half integer [74]*

Regarding Table 2.3, in the Figure 2.12 we show the change of topological class keeping the same type of topological invariant ($\mathbb{Z}$, $2\mathbb{Z}$ or $\mathbb{Z}_2$) by the addition (subtraction) of one dimension in the Hamiltonian. It is to say, a Hamiltonian which belongs to a specific symmetry class can be continuously transformed into each other without closing the gap.

2.6 Topology in non-Hermitian systems

Due to the notable interest in topological materials and their associated symmetry in recent years, some authors have explored the topological properties of non-Hermitian systems. By definition, a non-Hermitian Hamiltonian is related to dissipative systems.

Like the Hermitian systems of Section 2.5, non-Hermitian systems also exhibit time reversal symmetry when the operator $\mathcal{T}$ satisfies $[H, \mathcal{T}] = 0$ such that in the moment space $\mathcal{T}H^*(\boldsymbol{k})\mathcal{T}^{-1} = H(-\boldsymbol{k})$. On the other hand, the particle-hole symmetry is related to the conjugation of the charge such that $\mathcal{P}H^T(\boldsymbol{k})\mathcal{P}^{-1} = -H(-\boldsymbol{k})$, and the chiral symmetry, as in the Hermitian case, is a combination of both symmetries, such that $\mathcal{C}H^\dagger(\boldsymbol{k})\mathcal{C}^{-1} = -H(\boldsymbol{k})$. Specifically, chiral symmetry

particle-hole symmetry

Figure 2.12: *Bott periodicity [75]. Grey zones are chiral classes ($\mathcal{C} = 1$). The arrows show the classes that have the same topological classification adding a dimension $d \rightarrow d + 1$, as is showed in Table 2.3. s labels the Altland-Zirnbauer symmetry classes*

in non-Hermitian systems implies that the eigenvalues appear in pairs, which is fundamental for protected zero-energy edge states.

Although in Hermitian systems the degeneration of the bands play a fundamental role in topological phases, in non-Hermitian systems the exceptional points (EP) are those that become fundamental. To define the EP, consider a 2×2 Hamiltonian H where a pair of eigenstates is obtained, which we will call right (R) and left (L), such that n is the eigenvalue index,

$$H|\Psi_n^R\rangle = E_n|\Psi_n^R\rangle,$$
$$H^\dagger|\Psi_n^L\rangle = E_n^*|\Psi_n^L\rangle.$$

EP's are defined by the complex energy $E_n(\boldsymbol{k}) = 0$ whose states $|\Psi_n^R\rangle$ and $|\Psi_n^L\rangle$ are joined and therefore become orthogonal, that is, $\langle\Psi_n^L|\Psi_n^R\rangle = 0$ and the Hamiltonian becomes non-diagonalizable [76, 77]. Later in this section, when we talk about the winding number, we will come back to this issue.

Berry's complex phase for non-Hermitian Hamiltonians is defined as [78]

$$\gamma_n^{\alpha\beta} = i \oint_C \langle\Psi_n^L(\boldsymbol{k})|\boldsymbol{\nabla}_{\boldsymbol{k}}|\Psi_n^R(\boldsymbol{k})\rangle \cdot d\boldsymbol{k}. \tag{2.35}$$

It is important to note that the meaning and origin of equation (2.35) is the same as for Hermitian systems that we explained in section 2.2 with equations (2.6) and (2.7). Because

contour C encloses the EP's, the winding number is finite and the amount of winding numbers is determined by the number of EP within the contour [79]. Note that now $\gamma_n^{\alpha\beta}$ is a complex number. Therefore, the real part indicates the usual geometric phase that the system acquires in each cycle and this is a topological invariant. The imaginary part indicates the decay of the probability and it is not necessarily a topological invariant.

When the contour C of equation (2.35) is a surface and $d\boldsymbol{k}$ is replaced by an area element, the corresponding topological invariant is known as the Chern number. This number is written as [78, 80]

$$C_n^{LR} = \frac{1}{2\pi} \int_{BZ} \epsilon_{\mu\nu\rho} \mathcal{F}_{n,\mu\nu}^{LR} dS_\rho, \tag{2.36}$$

where $\epsilon_{\mu\nu\rho}$ is the order-3 Levi-Civita tensor, with $\mu, \nu, \rho = x, y, z$ and $\mathcal{F}_n^{LR} = \nabla_k \times \mathcal{A}_n^{LR}$ is the Berry curvature, with $\mathcal{A}_n^{LR} = i\langle\Psi_n^L|\nabla_{\boldsymbol{k}}|\Psi_n^R\rangle$ as the Berry connection. The term dS_ρ in equation (2.36) refers to the area section through which the Berry flux is considered. We emphasize that, in general terms, C_n^{LR} is also a complex number.

For symmetric Hamiltonians, that is, $H = H^T$, then $|\Psi_n^L\rangle$ is the conjugate complex of $|\Psi_n^R\rangle$ and therefore the Berry phase and the Chern number are real.

Now, let's consider the Hamiltonian $H = h_x\sigma_x + h_y\sigma_y$, where, in general h_x, h_y are complex, for which we have the eigenstates $|\Psi_\pm^R\rangle = \frac{1}{\sqrt{2}}\left(e^{-i\phi(k)}, \pm 1\right)^T$ and $|\Psi_\pm^L\rangle = \frac{1}{\sqrt{2}}\left(e^{i\phi(k)}, \pm 1\right)^T$ where $\phi(k) = \tan^{-1}(h_y/h_x)$. Thus, when k varies from 0 to 2π, the winding number is generalized in the parameter space as [81]

$$\begin{aligned}\mu &= \frac{1}{2\pi}\oint_C \frac{h_x dh_y - h_y dh_x}{h_x^2 + h_y^2} \\ &= \frac{1}{2\pi}\int_0^{2\pi} dk \frac{h_x \partial_k h_y - h_y \partial_k h_x}{h_x^2 + h_y^2}.\end{aligned} \tag{2.37}$$

From equation (2.37) it can be seen that the EPs are given by $h_x^2 + h_y^2 = 0$. The winding number can be written as

$$\mu = \frac{1}{2\pi}\oint_C \partial_k\phi \, dk. \tag{2.38}$$

Since in general terms h_x and h_y are complex, then ϕ is complex and it can be written as $\phi = \phi_r + i\phi_i$. It can be proved that $\oint_C \partial_k\phi_i dk = \phi_i(2\pi) - \phi_i(0) = 0$ and therefore the imaginary part of ϕ has no effect on the integral of the winding number. On the other hand, ϕ_r can be written as $\tan 2\phi_r = (\tan\phi_1 + \tan\phi_2)/(1 - \tan\phi_1\tan\phi_2)$ where $\tan\phi_1 = (h_{yr} + h_{xi})/(h_{xr} - h_{yi})$ and $\tan\phi_2 = (h_{yr} - h_{xi})/(h_{xr} + h_{yi})$. Therefore it can be proved that the winding number can be written as [81]

$$\mu = \frac{1}{4\pi}\oint dk\left(\partial_k\phi_1 + \partial_k\phi_2\right). \tag{2.39}$$

A fundamental condition for a non-Hermitian Hamiltonian to have topological invariants (like the winding number) is that in the range of parameters where there is a gap, at least an EP is allowed to be enclosed.

Although the importance of EP has already been emphasized in the topological analysis of non-Hermitian Hamiltonians, experimentally its importance has also been evidenced [82–84]. Although there was controversy a few years ago about bulk-boundary correspondence in non-Hermitian sys-

tems, from different experiments and theoretical analyzes, it is known that when chiral symmetry is present, edge states are localized with zero energy without dissipation.

Chapter 3

Tight binding approximation

The concept of tight binding will be used in Chapter 4 to model the topological phases in N-layer ABC-graphene boron-nitride in moiré superlattices and in Chapter 5 to build the non-Hermitian topolectric circuit model that emulates a new type of complex hop SSH model.

Tight binding is an approximate method used for calculating the electronic structure of bands based on a set of wave functions that overlap localized isolated atoms for each atomic site. The fundamental basis of tight-binding approximation is that electrons are located in one atomic position and the probability of finding it in another position vanishes. Thus, the Bloch wave function in the crystal is assumed as a linear combination of the local Wannier function $\Phi(\boldsymbol{r} - \boldsymbol{R})$ centered at the lattice vector $\boldsymbol{R}$,

$$\Psi_{\boldsymbol{k}}(\boldsymbol{r}) = \frac{1}{\sqrt{N}} \sum_{\boldsymbol{R}} e^{i\boldsymbol{k}\cdot\boldsymbol{R}} \Phi(\boldsymbol{r} - \boldsymbol{R}), \tag{3.1}$$

where N is the number of unit cells in the crystal. According to Bloch's theorem, to represent electrons in a perfect crystal, there is a basis for wavefunctions such that each is an energy eigenstate. Also, each of those wavefunctions is a Bloch wave. Therefore, the Ψ wavefunction can be written as

$$\Psi(\boldsymbol{r}) = e^{i\boldsymbol{k}\cdot\boldsymbol{r}} u(\boldsymbol{r}), \tag{3.2}$$

where $u(\boldsymbol{r})$ has the same periodicity as the crystal's atomic structure. Konschuh [85] verifies the Bloch Theorem on crystals by shifting the wavefunction by a translation vector.

3.1 Tight binding in graphene systems

Graphene is a layer of carbons in which the conduction and valence band touch each other at two distinct points of Brillouin zone. The simplest description of graphene employs two band model for p_z orbitals on the two equivalent atoms in the unit cell [21].

In the following sections, we will take the concept of tight-binding approach to analyze the graphene. Initially, we will make an analysis of the geometry and the tight-binding concept to do some topological analysis.

3.1.1 Graphene geometry

In Figure 3.1, we show a Bravais lattice. In particular $\boldsymbol{a_1} = d(0, -1)$, $\boldsymbol{a_2} = \frac{d}{2}(-1, \sqrt{3})$, with d as the distance between sites. It is important to note that the Bravais lattice encloses the entire crystalline lattice and it has the property of repeating itself throughout the direct space.
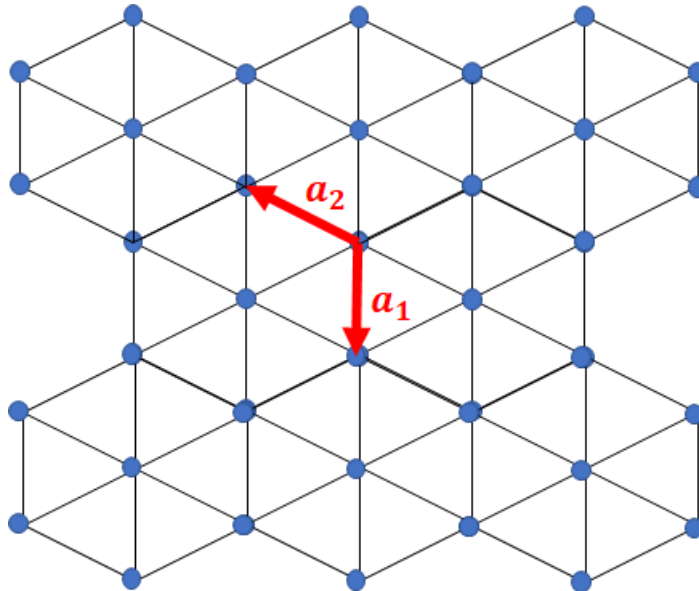

Figure 3.1: *The Bravais lattice of a honeycomb hexagonal lattice.*

Conveniently, for graphene lattice we selected a Bravais lattice with second neighbors, as we show in Figure 3.2, with $\boldsymbol{a_1} = (\sqrt{3}d, 0)$ and $\boldsymbol{a_2} = \frac{\sqrt{3}d}{2}(1, \sqrt{3})$ and $d \approx 1.42\text{Å}$ [86].
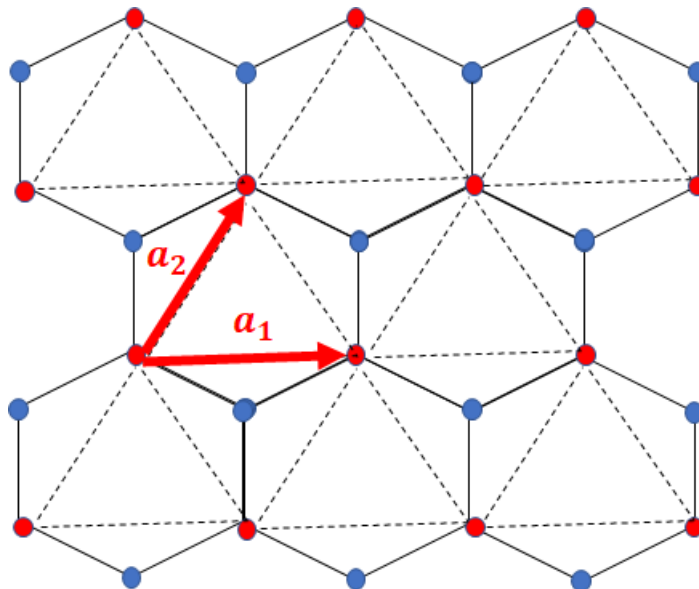

Figure 3.2: *The Bravais lattice of a honeycomb hexagonal lattice with second neighbors.*

The reciprocal network is a consequence of the translational symmetry of functions that describe periodic physical quantities in the Bravais lattice. A Bravais lattice defined in the reciprocal space is the set of $\boldsymbol{K}$-wave vectors that can be calculated from the translation of vectors according

to $e^{i\boldsymbol{K}\cdot\boldsymbol{R}} = 1$, therefore,

$$\boldsymbol{K}\cdot\boldsymbol{R} = 2\pi\eta, \qquad \eta = \sum_i n_i h_i \Rightarrow \eta \in \mathbb{Z}. \tag{3.3}$$

The $\boldsymbol{K}$-vectors can be written as

$$\boldsymbol{K} = \sum_{j=1}^{2} h_j \boldsymbol{b_j}; \qquad h_j \in \mathbb{Z}, \tag{3.4}$$

and the reciprocal lattice vectors $\boldsymbol{b_1}, \boldsymbol{b_2}$ are defined by $\boldsymbol{a_i}\cdot\boldsymbol{b_j} = 2\pi\delta_{ij}$. Therefore, in graphene $\boldsymbol{b_1} = \frac{2\pi}{3d}(\sqrt{3}, -1)$ and $\boldsymbol{b_2} = \frac{4\pi}{3d}(0, 1)$. This concept is useful to define the Brillouin zone, as we show in Figure 3.3 in the blue hexagon.
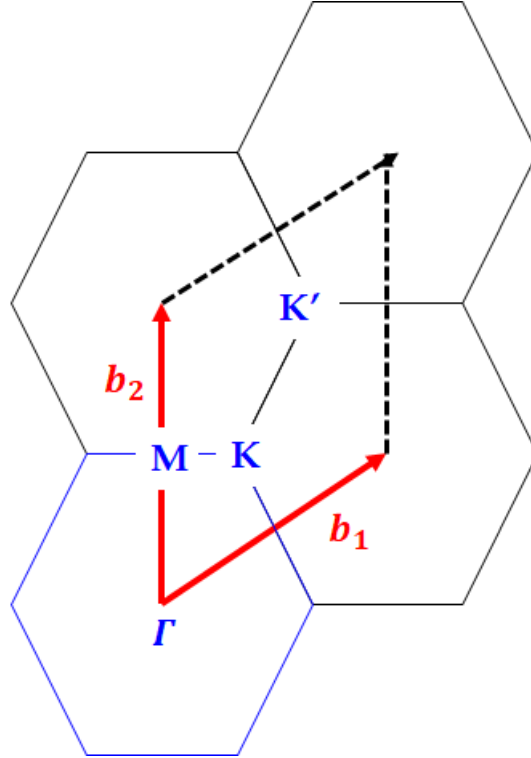

Figure 3.3: *Reciprocal lattice vectors $\boldsymbol{b_1}$ and $\boldsymbol{b_2}$. The Brilloine zone (blue hexagon) and the special points $\boldsymbol{\Gamma} = 0\boldsymbol{b_1} + 0\boldsymbol{b_2}$, $\boldsymbol{M} = \frac{1}{2}\boldsymbol{b_1} + 0\boldsymbol{b_2}$, $\boldsymbol{K} = \frac{1}{3}\boldsymbol{b_1} + \frac{1}{3}\boldsymbol{b_2}$ and $\boldsymbol{K'} = \frac{2}{3}\boldsymbol{b_1} + \frac{2}{3}\boldsymbol{b_2}$*

According Figure 3.2, we define the vectors of first neighbors as $\boldsymbol{\delta_1} = d(0, -1)$, $\boldsymbol{\delta_2} = \frac{1}{2}d\left(\sqrt{3}, 1\right)$, $\boldsymbol{\delta_3} = \frac{1}{2}d\left(-\sqrt{3}, 1\right)$, and the second neighbors as $\boldsymbol{\beta_1} = \frac{1}{2}d\left(\sqrt{3}, -3\right)$, $\boldsymbol{\beta_2} = d\left(\sqrt{3}, 0\right)$, $\boldsymbol{\beta_3} = \frac{1}{2}d\left(\sqrt{3}, 3\right)$, $\boldsymbol{\beta_4} = \frac{1}{2}, d\left(-\sqrt{3}, 3\right)$, $\boldsymbol{\beta_5} = d\left(-\sqrt{3}, 0\right)$, $\boldsymbol{\beta_6} = \frac{1}{2}d\left(-\sqrt{3}, -3\right)$, where here we took $d = 2.6833a_0$ with $a_0 = 5.29 \times 10^{-11}m$ as the Bohr radius, as is shown in Figure 3.4.

3.1.2 Electronic properties of graphene

From tight-binding model with nearest-neighbor hopping, the Bloch Hamiltonian for graphene [87] is given by

$$\mathcal{H}_0(\boldsymbol{k}) = \begin{bmatrix} \frac{\Delta}{2} & t_1 f(\boldsymbol{k}) \\ t_1 f^*(\boldsymbol{k}) & -\frac{\Delta}{2} \end{bmatrix} = t_1[\text{Re}(f(\boldsymbol{k}))\sigma_x + \text{Im}(f(\boldsymbol{k}))\sigma_y] + \frac{\Delta}{2}\sigma_z = \boldsymbol{h}\cdot\boldsymbol{\sigma}, \tag{3.5}$$
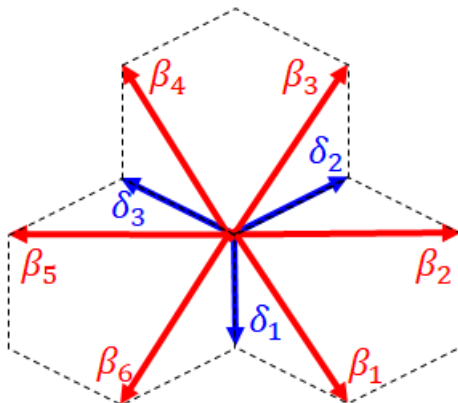
Figure 3.4: *Graphene first neighbor vectors (blue arrows) and second neighbor vectors (red arrows)*

where t_1 is the first neighbor hopping, Δ is the so called mass term that is present whenever there is a sublattice symmetry breaking perturbation and it is assumed to vanish in the case of freestanding graphene [87], and $f(\boldsymbol{k}) = 1 + e^{i\boldsymbol{k} \cdot a_1} + e^{i\boldsymbol{k} \cdot a_2}$ is the form factor associated to first neighbor hopping in the honeycomb lattice. The graphene energy bands are Dirac cones described by

$$E_\pm(\boldsymbol{k}) = \pm \sqrt{\left| \frac{\Delta}{2} \right|^2 + |t_1 f(\boldsymbol{k})|^2}. \tag{3.6}$$

Therefore, we can write the Bloch states of graphene as two component spinors $(\phi_1, \phi_2)^T$. It is reasonable to consider $|\phi_1| = |\phi_2|$. Then, those states are analogous to eigenstates of a pseudo-spin under the influence of a magnetic field in plane, as Haldane's Model [31]. That model was motivated by the Quantum Hall effect without a magnetic field per unit cell and without the Landau level structure [62]. The Haldane Hamiltonian is defined by

$$H = 2t_2 \cos\phi \sum_i \cos(\boldsymbol{k} \cdot \boldsymbol{\beta}_i) I + t_1 \sum_i \left[\cos(\boldsymbol{k} \cdot \boldsymbol{\delta}_i)\sigma_x + \sin(\boldsymbol{k} \cdot \boldsymbol{\delta}_i)\sigma_y\right] + \left[M - 2t_2 \sin\phi \sum_i \sin(\boldsymbol{k} \cdot \boldsymbol{\beta}_i)\right]\sigma_z$$

$$= \begin{bmatrix} M + 2t_2 \left[\cos\phi \sum_i \cos(\boldsymbol{k} \cdot \boldsymbol{\beta}_i) - \sin\phi \sum_i \sin(\boldsymbol{k} \cdot \boldsymbol{\beta}_i)\right] & t_1 \sum_i \left[\cos(\boldsymbol{k} \cdot \boldsymbol{\delta}_i) - i \sin(\boldsymbol{k} \cdot \boldsymbol{\delta}_i)\right] \\ t_1 \sum_i \left[\cos(\boldsymbol{k} \cdot \boldsymbol{\delta}_i) + i \sin(\boldsymbol{k} \cdot \boldsymbol{\delta}_i)\right] & -M + 2t_2 \left[\cos\phi \sum_i \cos(\boldsymbol{k} \cdot \boldsymbol{\beta}_i) + \sin\phi \sum_i \sin(\boldsymbol{k} \cdot \boldsymbol{\beta}_i)\right] \end{bmatrix}, \tag{3.7}$$

where σ_i are Pauli matrices, M is the inversion-symmetry-breaking on-site, t_1 is a real hopping between nearest neighbor on different sublattice and t_2 is a real hopping term between second neighbor site in the same sublattice. The ϕ angle is the phase acquired by t_2 elements. δ_i is the displacements from a site to its three nearest-neighbor sites, and β_i is the set of displacements to the six second neighbors, as Haldane expose in Figure 3.5.

The eigenvalues of each band of Haldane's model is given by

$$E_\pm(\boldsymbol{k}) = \mp \sqrt{\begin{aligned} &t_1{}^2 \left(\cos \frac{\sqrt{3}dk_x}{2} \cos \frac{3dk_y}{2} + 2\cos\sqrt{3}dk_x + 3 \right) + M^2 + \\ &4t_2 \cos\phi \left(\cos \frac{d\left(\sqrt{3}k_x + 3k_y\right)}{2} + \cos \frac{d\left(\sqrt{3}k_x - 3k_y\right)}{2} + \cos\sqrt{3}dk_x \right) \end{aligned}}, \tag{3.8}$$
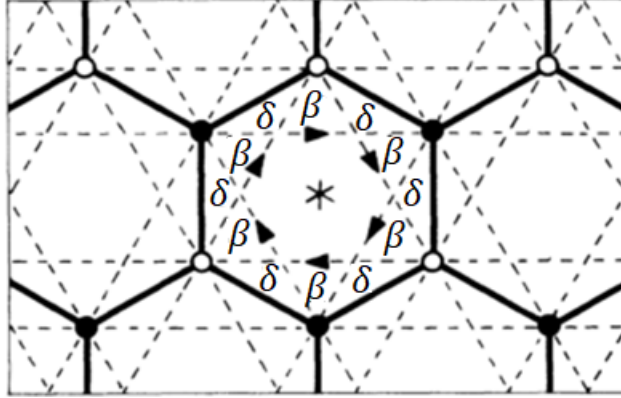
46

Figure 3.5: *The graphene lattice according the Haldane model. Nearest-neighbor bonds (solid lines) and second-neighbor bonds (dashed lines). Image source: adapted from Haldane [31]*

and the eigenvalues are given by

$$\Psi_{\pm}(\boldsymbol{k}) = \left[\begin{array}{c} \dfrac{M \mp \sqrt{4t_1{}^2 \cos \frac{\sqrt{3}dk_x}{2} \cos \frac{3dk_y}{2} + 2t_1{}^2 \cos \sqrt{3}dk_x + M^2 + 3t_1{}^2}}{t_1\left(2\cos \frac{\sqrt{3}dk_x}{2}\left(\cos \frac{dk_y}{2} + i\sin \frac{dk_y}{2}\right) - i\sin dk_y + \cos dk_y\right)} \\[20pt] \dfrac{M \pm \sqrt{4t_1{}^2 \cos \frac{\sqrt{3}dk_x}{2} \cos \frac{3dk_y}{2} + 2t_1{}^2 \cos \sqrt{3}dk_x + M^2 + 3t_1{}^2}}{t_1\left(2\cos \frac{\sqrt{3}dk_x}{2}\left(\cos \frac{dk_y}{2} + i\sin \frac{dk_y}{2}\right) - i\sin dk_y + \cos dk_y\right)} \end{array} \right] \tag{3.9}$$

Haldane showed that, at the Fermi level and zero-temperature limit of a 2D periodic electron gap system, the transverse conductivity has a behavior quantized by $\sigma_H = \nu e^2/h$ where ν takes integer values. If $|t_2/t_1| < \frac{1}{3}$ and $|M/t_2| < 3\sqrt{3}|\sin \phi|$, there is a quantum Hall effect phases, it is to say, $\nu = \pm 1$. Therefore, the diagonal terms of are zero. On the other hand, if $\nu = 0$ the graphene behaves like a normal semiconductor (see Figure 3.6(a)).
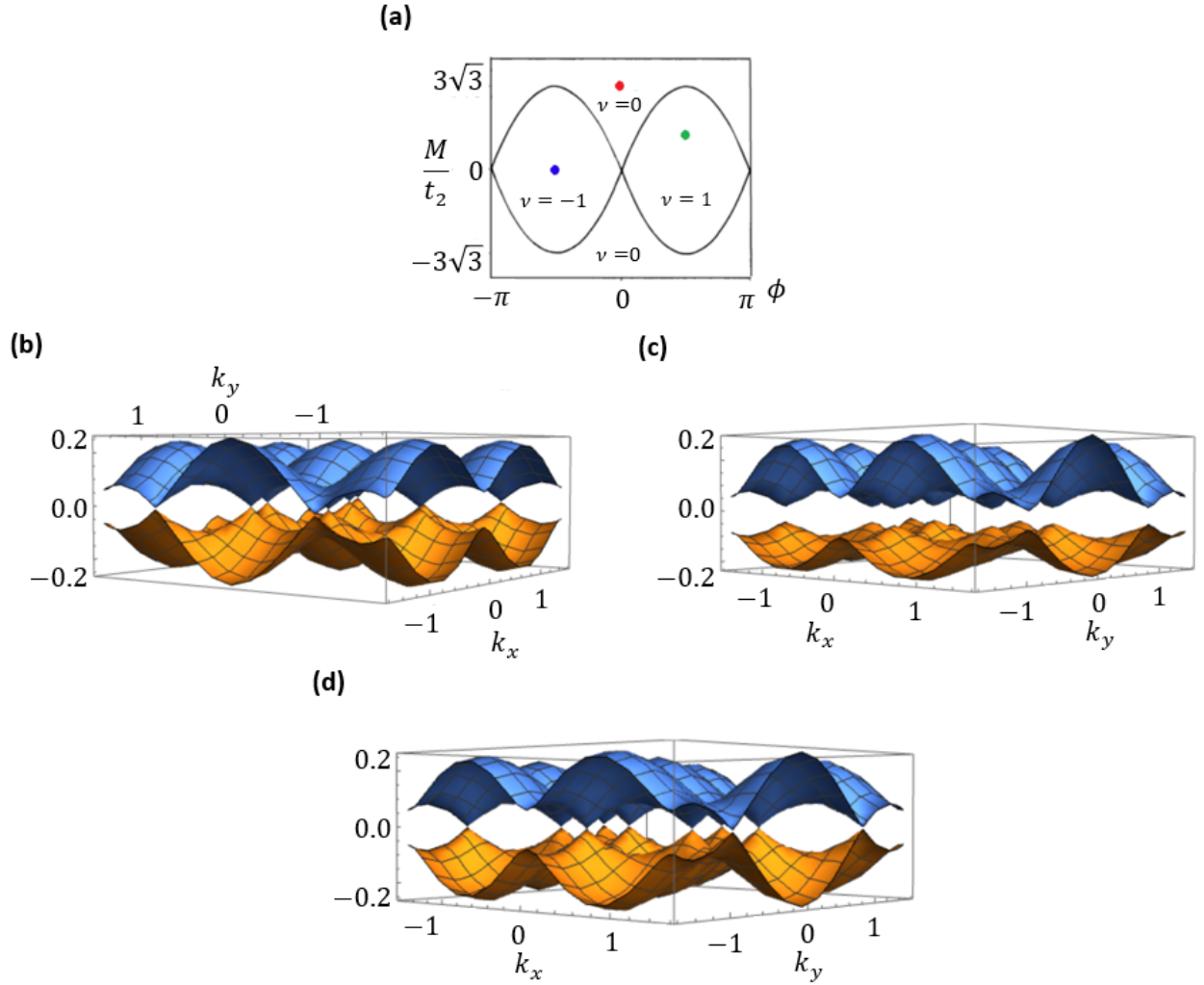
Figure 3.6: *(a) Phase diagram assuming $|t_2/t_1| < \frac{1}{3}$ where zero-field quantum Hall effect phases are shown as $\nu = \pm 1$ region. The $\nu = 0$ region is related to normal semiconductor phase. (Image source: Haldane [31]). (b) Blue point in sketch (a). Eigenvalues of (3.7) with $M/t_2 = 0$ and $\phi = -\pi/2$. (c) Red point in sketch (a). Eigenvalues of (3.7) with $M/t_2 = 3\sqrt{3}$ and $\phi = 0$. (d) Green point in sketch (a). Eigenvalues of (3.7) with $M/t_2 = \sqrt{3}$ and $\phi = \pi/2$. In all cases, there are 6 Dirac points in the reciprocal lattice.*

Part III

Method development

Chapter 4

Topological phases in N-layer ABC-graphene boron-nitride moiré superlattices

The formation of moiré patterns is due to the overlap of two or more periodic crystals with slightly different lattice constants or simply with a twist among the layers, as we show in Figure 4.1. The electronic properties of van der Walls crystalline heterostructures [88,89] can be modified by moiré superlattice potentials.
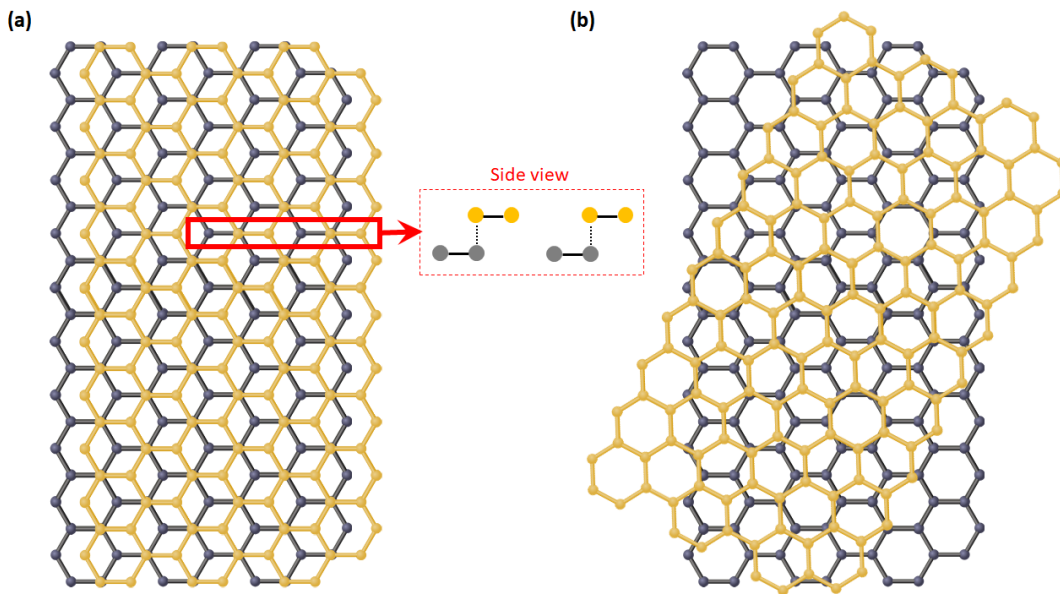

Figure 4.1: *Example of two kind of moiré patterns:* ***(a)*** *the translation of a hexagonal layer on another layer of the same geometry and* ***(b)*** *under the rotation.*
.

The appearance of magic angles in twisted bilayer graphene has shown the formation of correlated insulating phases and the appearance of high temperature superconductivity [88,90,91]. In the case of two overlapping graphene layers, the coupling becomes stronger when the angle between them becomes smaller [92]. However, in another view, the Fermi velocity vanishes at a "magic angle", leading to appeareance of flat bands and stronger conductivity [93].

Interestingly, the twisted graphene layers with the presence of Van Hove singularities [94] allow the existence of new phases such as magnetism, superconductivity or charge density waves. It is convenient to say that the electronic structure varies with the twist angle [95]. On the other hand,

the electrical properties of multiple graphene layers can be altered by an in-plane magnetic field, out-of-plane electric field and to the applied bias voltage along with the twist angle [96,97].

Heterostructures of various materials have widely studied from the point of view of their electronic properties, such as MoS_2-MoS_2 and WS_2-WS_2 [98], germanium [99], monolayers of WS_2-MoS_2 [100], $MoSe_2-WSe_2$ [101]. Each of these structures has topological properties that could lead to the development of new materials from the identification of topological invariants [102,103].

We studied the behavior of Chern numbers in heterostructures of graphene (monolayer (G), bilayer (BG) or trilayer (TG))/hexagonal-boron-nitride (hBN) moiré superlattices. The main object of our work is to identify the different valley Chern phases that appear in this kind of superlattices as a function of the number of graphene layers and the dependence of scalar and vector moiré vector potentials.

There are different properties of rhombohedral N-layer of graphene on other substrates that have been discussed widely in the literature, such as SiC [104], Ni [105], SiO_2 [106]. However, the study of the interaction of an hBN sheet on 1, 2 or 3 layers of graphene opens the study to understand the interactions with other substrates. Our work shows the importance of the scalar and magnetic vector potential to generate topological phases in superlattices without making rotations, which in practice can be complicated.

Song et $al.$ [107] showed experimentally that the lattice mismatch between the graphene and hBN generate moiré superlattices whose topological bands and the Berry curvature of the Bloch topological bands are highly sensitive to the location of boron-nitride respect to the graphene layer, and the sub-lattice interaction. Therefore, the electronic topology of the crystal can be controlled by the proper alignment of the crystal axes.

In BG/BN case, recent experiments have shown that for certain magical angles the anomalous Hall effect appears. In addition, the valence and conduction bands appear with Chern numbers $C = \pm 1$ [108]. The possible explanation is that the 3/4-filling of the spin-valley polarized ferromagnetic insulator leading to electrons fill a Chern band. It is interesting to note that twisted G/BN and BG/BN systems also have shown flat bands [109,110] and are relevant building blocks of ongoing experiments that must be fully understood because they can be the origin of coupled topological bands.

Recent experiments by Feng et $al.$ [102], have shown the existence of a correlated Chern insulator in the TG/BN moiré superlattice from changes in the magneto-transport by reversing the vertical direction of the applied electric field. The TG/BN case has been theoretically studied [111] and it provides an attractive platform to explore Chern insulators because it has almost flat moiré minibands with an electrically tunable Chern number that depends on the valley. It is because the Chern weights that add up to zero or finite integer value arise due to the primary and secondary gaps depending on the choice of sub-lattice interaction.

It is further also revealed that, based on the structure of the moiré Hamiltonian, such as the inclusion of off-diagonal terms, different Chern numbers can be configured due to unequal electron-hole Chern weights. In a study of the G/BN [112], it is showed that the off-diagonal terms have an important implication in the miniband spectra and therefore in the Berry connection.

According to the models explained in Section 6, for the calculation of the different Chern diagrams for G/BN, BG/BN and TG/BN, the off-diagonal Hamiltonian terms are of fundamental

importance. These terms refer to gauge potential and mass terms, as will be seen in the model.

To understand the nomenclature that we will use in this chapter, in Figure 4.2, we show the geometry of two stacked honeycomb lattices, where one moves over the other.
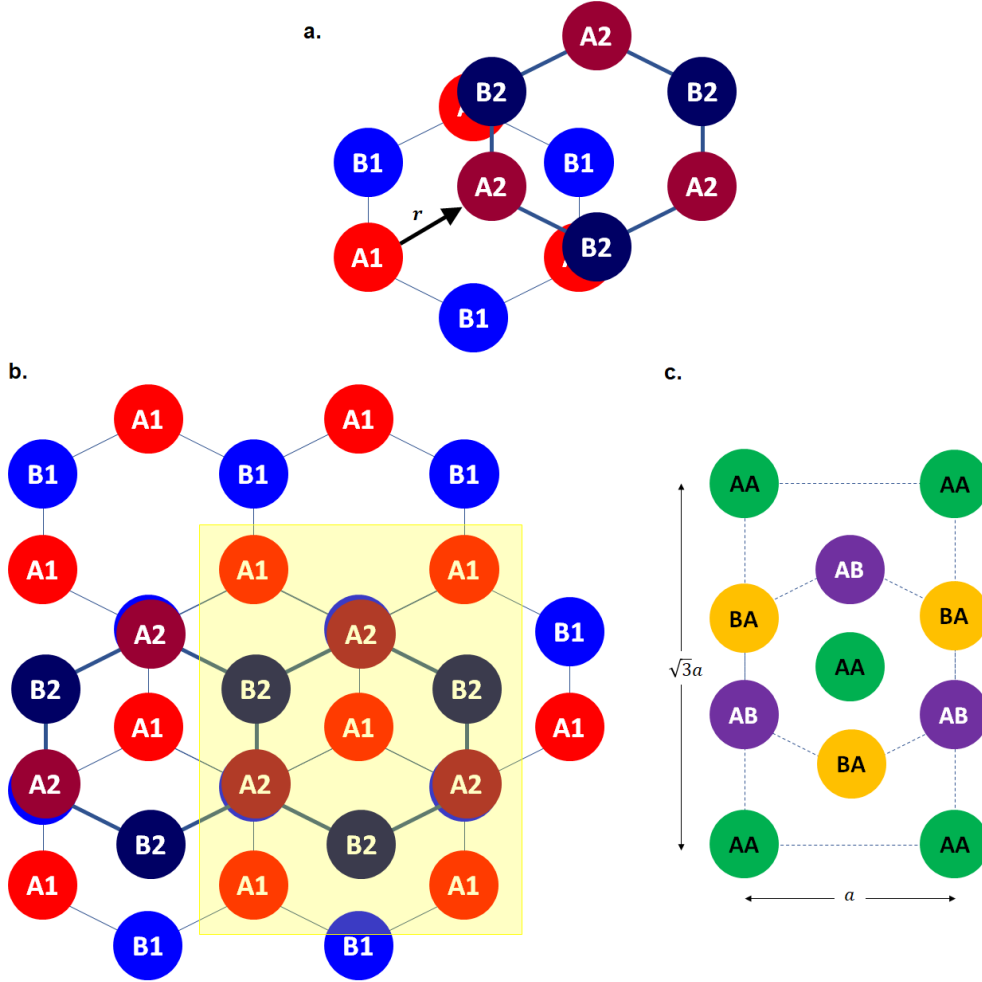

Figure 4.2: *Schematic representation of two honeycomb layers with the top layer sites marked by $A2$ and $B2$ and the bottom layer sites marked by $A1$ and $B1$. Figure **a.** shows the displacement in the $\boldsymbol{r}$ direction of one layer over the other. In Figure **b.**, we show the displacement $\boldsymbol{r} = (0, a/\sqrt{3})$ of the top layer over the bottom layer to form an AB stacking arrangement that is explained in Figure **c.** from the shaded yellow area in Figure **b.***

In Figure 4.2**a.** we show the displacement $\boldsymbol{r}$ of the top layer (which we have named with sites $A2$ and $B2$) on the bottom layer (named by sites $A1$ and $B1$). Figure 4.2**b.** shows a displacement $\boldsymbol{r} = (0, a/\sqrt{3})$ of the top layer on the bottom layer to configure an AB stacking, in which site $A2$ is over site $B1$. Finally, Figure 4.2**c.** shows the AA, AB and BA stacking arrangements that form in the yellow shaded area in Figure 4.2**b.** It is easy to see that under an AB arrangement you can also configure BB stacking arrangement, if the displacement of layer 2 on layer 1 is in direction $\boldsymbol{r} = (0, -a/\sqrt{3})$ or equivalently, rotate 60° one sheet over the other.

4.1 Hamiltonian model

The Hamiltonian model to build the moiré patterns is based on symmetry and coupling co-efficients of symmetric and anti-symmetric inversion terms [113]. Other method is based on the transformation to the complex form, with amplitude C_μ and phase ϕ_μ factors of the sublattice interaction parameters [114]. Here, we follow the later form of representation.

Based on the periodicity of the moiré potential [115], the effective K-valley Hamiltonian for rhombohedral N-layer graphene coupled to an hBN layer is given by [111]

$$H_N^\xi = \frac{v_0^N}{(-t_1)^{N-1}} \begin{bmatrix} 0 & (\pi^\dagger)^N \\ \pi^N & 0 \end{bmatrix} + \Delta\sigma_z + H_N^R + H_\xi^V + H_\xi^A, \tag{4.1}$$

where $\xi = \pm 1$ distinguishes the two types of possible alignments ($0°$ and $60°$) between the layers of graphene and BN, taking as a reference the side view of Figure 4.1(a) and the displacements explained in figure 4.2, where the moiré pattern affect the low energy A (bottom) or B (top) sites in the graphene layer contacting BN, as is shown in figure 4.3(b) and (c) [116].
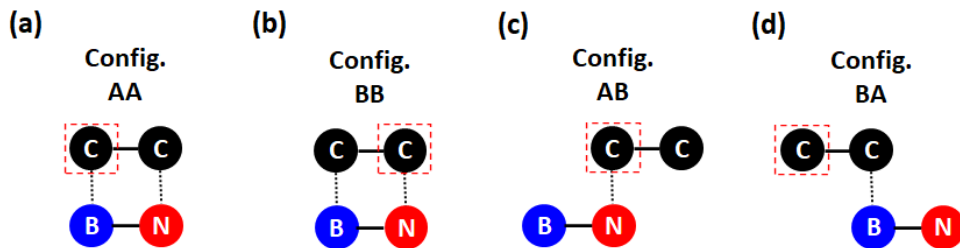

Figure 4.3: *Schematic representation of different symmetric stacking arrangements of G/BN. **(a)-(b)** Each carbon atom is located on top of a nitrogen and a boron atom but the configuration AA ($\xi = 1$) is rotated $60°$ in relation to configuration BB ($\xi = -1$). The square of red dashed lines distinguishes one of the two sublattices of graphene. **(c)** A carbon atom sits on top of a nitrogen atom and a carbon atom is in the middle of the BN's hexagon. **(d)** A carbon atom sits on top of a boron atom and a carbon atom is in the middle of the BN's hexagon.*

The first term in equation (4.1) describes the low-energy N-layer graphene 2×2 Hamiltonian, with the momentum operator $\pi = \nu p_x + i p_y$ where $\nu = 1$ is used for the principal valley K of the graphene. The second term of (4.1) induces the interlayer potential difference which is proportional to the mass term through Δ.

The H_N^R term describes the remote hopping term corrections for N-layers. For TG/BN the H_3^R term is given by [111],

$$H_3^R = \left[\left(\frac{2v_0 v_3 p^2}{t_1} + t_2 \right) \sigma_x \right] + \left[\frac{2v_0 v_4 p^2}{t_1} - \Delta' + \Delta'' \left(1 - \frac{3v_0^2 p^2}{t_1^2} \right) \right] \mathbb{1}, \tag{4.2}$$

where $v_m = \sqrt{3}a|t_m|/2\hbar$ with $a = 2.46$Å. v_0 is the Fermi velocity. ν_3 and ν_4 are the couplings between the low energy and low-high-energy sites located on different layers, respectively. The hopping parameters are given by $t_0 = -2.62$ eV, $t_1 = 0.358$ eV, $t_2 = -0.0083$ eV, $t_3 = 0.293$ eV, $t_4 = -0.144$ eV, $\Delta' = 0.0122$ eV and $\Delta'' = 0.0095$ eV [111, 117].

For BG/BN [118],

$$H_2^{\mathrm{R}} = v_3 p \left(\frac{p}{t_1} - 1 \right) \sigma_x \frac{v_0}{t_1} \left(\frac{\Delta' v_0}{t_1} + 2v_4 \right) \begin{pmatrix} \pi^\dagger \pi & 0 \\ 0 & \pi \pi^\dagger \end{pmatrix}. \tag{4.3}$$

For the case G/BN, $H_1^R = 0$ because there are no intermediate layers between graphene and BN.

Specifically, the last two terms of equation (4.1) are of particular interest to us. The diagonal term H_ξ^V is given by

$$H_\xi^V(\mathbf{r}) = V_{AA/BB}^M(\boldsymbol{r}) \frac{\xi \sigma_z + \mathbb{1}}{2}, \tag{4.4}$$

where

$$V_{AA/BB}^M(\boldsymbol{r}) = 2C_{AA/BB} \mathrm{Re}\left[e^{i\phi_{AA/BB}} f^\xi(\mathbf{r}) \right], \tag{4.5}$$

with $f^\xi(\mathbf{r})$ as the triangular structure factor function, which is given by

$$f(\mathbf{r}) = \sum_{m=1}^{6} e^{i\xi \mathbf{G}_m \cdot \mathbf{r}} \frac{1 + (-1)^m}{2}, \tag{4.6}$$

where $G_m = \hat{R}_{\frac{2\pi m}{6}} \mathbf{G}_1$ is the six moiré reciprocal lattices and $\mathbf{G}_1 = \left[1 - (1+\delta)^{-1} \hat{R}_\theta \right] \left(0, \frac{4\pi}{3a} \right)$ are the moiré pattern harmonics, where the lattice mismatch $|\delta| \ll 1$, the misalignment angle $\theta \ll 1$ and $\hat{R}$ is the anticlockwise rotation matrix i.e. $\hat{R}_{\frac{2\pi m}{6}}$. The equation (4.6) goes into the diagonal terms, and $\frac{\xi \sigma_z + \mathbb{1}}{2}$ implies that, depending on the sign of ξ, only one of the terms of the diagonal of the Hamiltonian is affected.

On the other hands, the intersublattice off-diagonal term H_ξ^A is given by

$$H_\xi^A(\mathbf{r}) = \boldsymbol{A}^\xi(\mathbf{r}) \cdot \sigma_{xy}^\xi, \tag{4.7}$$

where

$$\boldsymbol{A}^\xi(\boldsymbol{r}) = V_{AB}^M \boldsymbol{\nabla}_{\boldsymbol{r}} \mathrm{Re}[e^{i\phi_{AB}} f^\xi(\boldsymbol{r})] \tag{4.8}$$

is the pseudomagnetic vector potential where $\sigma_{xy}^\xi = (\sigma_x, \xi \sigma_y)$ is the Pauli matrix vector and

$$V_{AB}^M = 2C_{AB} \left[\cos\tilde{\theta} \hat{z} \times \frac{\mathbb{1}}{|G|} - \sin\tilde{\theta} \frac{\mathbb{1}}{|G|} \right], \tag{4.9}$$

where $\cos\tilde{\theta} = (\alpha \cos\theta - 1)/\beta$, $\sin\tilde{\theta} = \alpha \sin\theta/\beta$ with $\beta = \sqrt{\alpha^2 - 2\alpha \cos\theta + 1}$ and $\alpha = 1 + \epsilon$ where θ is the relative twist and ϵ is the lattice constant mismatch between the graphene and hBN layers. From *ab initio* calculations [89, 114] the parameters of graphene on hBN are giving by $C_{AA} = -14.88$ meV, $\phi_{AA} = 50.19°$, $C_{BB} = 12.09$ meV, $\phi_{BB} = -46.64°$, $C_{AB} = -11.34$ meV, and $\phi_{AB} = -19.6°$.

Based on the last two terms of the equation (4.1), we will make a brief discussion of symmetric and antisymmetric moiré patterns [113]. For different phase angles, in Figure 4.4 we illustrate the H_ξ^V and H_ξ^A terms corresponding to equations (4.4) and (4.7), respectively.

The diagonal elements of the moiré potential (4.5) is defined as the sum of a symmetric and an antisymmetric function. Indeed, for a configuration $\xi = 1$ where, in general terms $C_{AA/BB} = C_{ii}$
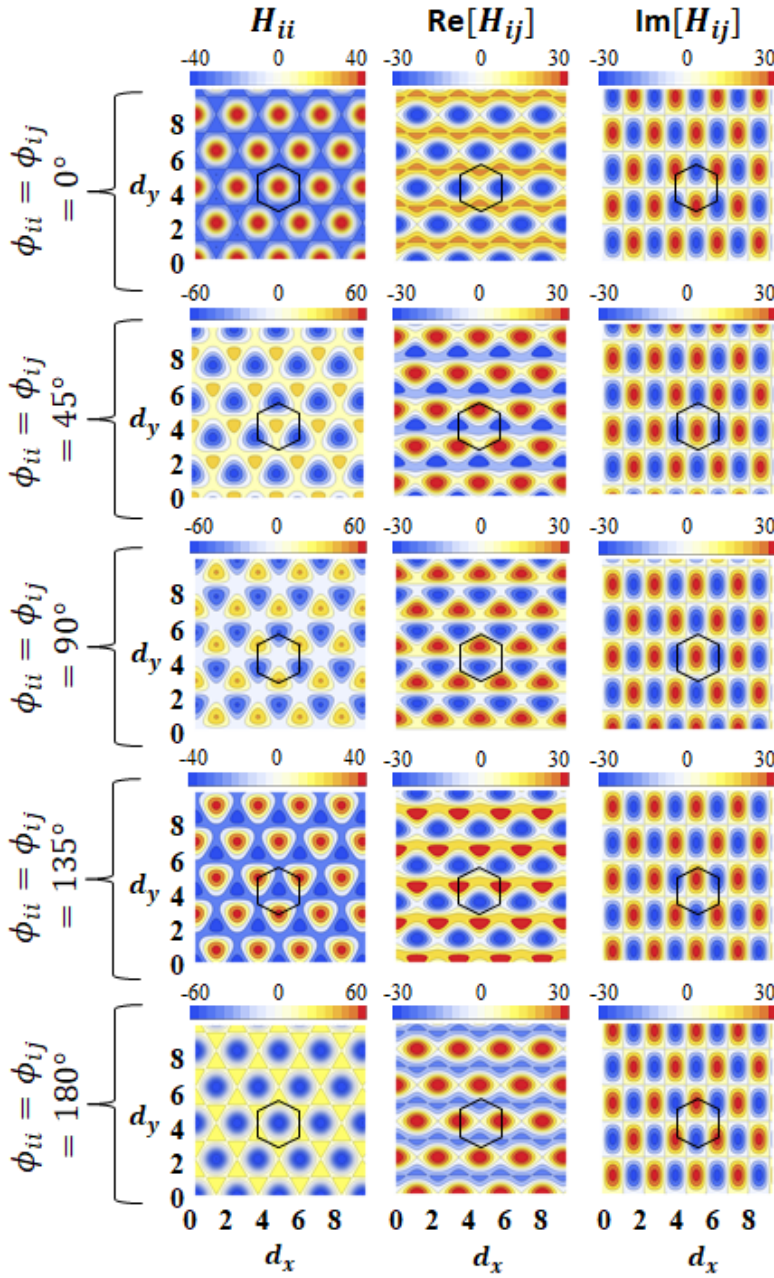
Figure 4.4: $d-$*depend intralayer Hamiltonian elements for different phase angles ϕ_{ii} and ϕ_{ij}. The black line hexagonal represents the real space presentation of extended unit cell. In the real space the neutral potential H_{ii} is associated with $\phi_{ii} = n\pi$ but the neutral potential for H_{ij} is associated with $\phi_{ij} = (2n+1)\pi/2$ with $n = 0, 1, \cdots$.*

and $\phi_{AA/BB} = \phi_{ii}$, we have

$$
\begin{aligned}
M_{ii}(\boldsymbol{r}) &= 2C_{ii}\mathrm{Re}\left[f(\boldsymbol{r})e^{i\phi_{ii}}\right] \\
&= C_{ii}\left(f_1(\boldsymbol{r})\cos\phi_{ii} + f_2(\boldsymbol{r})\cos\phi_{ii}\right),
\end{aligned}
\tag{4.10}
$$

with $f_1(\boldsymbol{r}) = \sum_{m=1}^{6} e^{i\boldsymbol{G}_m \cdot \boldsymbol{r}}$ as a symmetric function and $f_2(\boldsymbol{r}) = i\sum_{m=1}^{6}(-1)^{m-1}e^{i\boldsymbol{G}_m \cdot \boldsymbol{r}}$ as an antisymmetric function. In figure 4.5, we show functions f_1 and f_2. It is important to note the
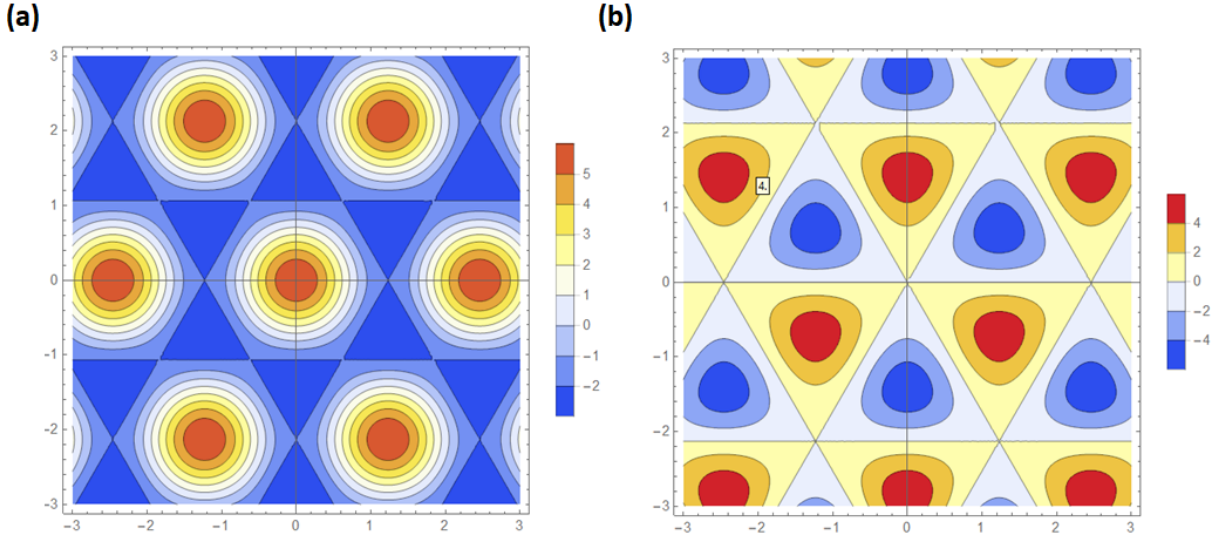
symmetry and antisymmetry around the point $(0,0)$.

(a)

(b)

Figure 4.5: *Symmetric and antisymmetric functions.* **(a)** $f_1(\mathbf{r})$ *and* **(b)** $f_2(\mathbf{r})$.

Hence, the equation (4.10) is symmetric when $\phi_{ii} = n\pi$, antisymmetric when $\phi = (2n+1)\pi/2$, and a combination of the two otherwise, as shown in Figure 4.6.
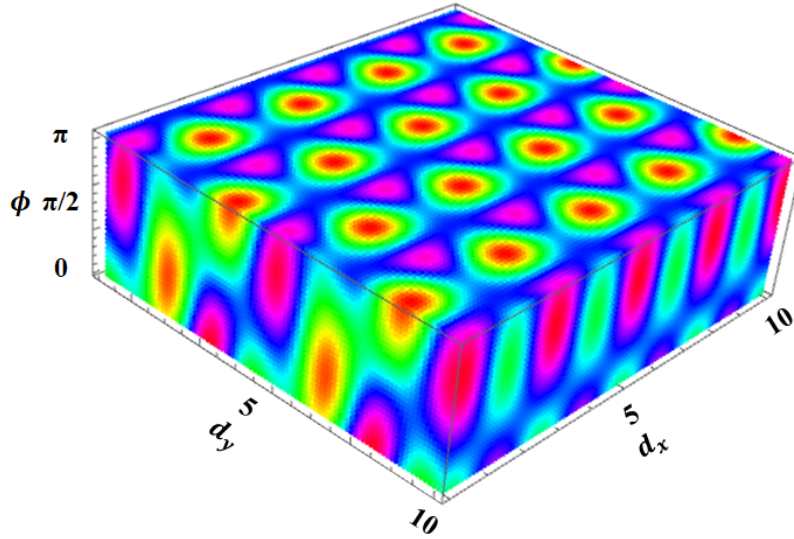

Figure 4.6: *Dependence of the scalar moiré potential term $M(\mathbf{r}) = 2C\mathrm{Re}\left[f(\mathbf{r})e^{i\phi}\right]$ on the phase angle ϕ, the periodicity in the real space is between $0 < \phi < \pi$. Must be noted that the $M(\mathbf{r})$ is a combination of $f_1(\mathbf{r}) = \sum_{m=1}^{6} e^{i\mathbf{G}_m\mathbf{r}}$ (symmetric function) and $f_2(\mathbf{r}) = i\sum_{m=1}^{6}(-1)^{m-1}e^{i\mathbf{G}_m\mathbf{r}}$ (antisymmetric function), it is relevant to the parametrization of the moiré patterns.*

Regarding the off-diagonal terms related to the equation 4.7, it describes the intersublattice tunneling within the graphene or hBN layer. H_ξ^A is related to the potential vector term $\boldsymbol{A}^\xi(\boldsymbol{r})$ which can be represented by its magnitude and orientation, as we show in Figure 4.7 and it is

analytically deduced as

$$
\begin{aligned}
\mathbf{A}^{\xi}(\mathbf{r}) &= V_{AB}^{M} \boldsymbol{\nabla}_{\boldsymbol{r}} \mathrm{Re}[e^{i\phi_{AB}} f(\boldsymbol{r})] \\
&= V_{AB}^{M} \boldsymbol{\nabla}_{\boldsymbol{r}} \mathrm{Re}\left[\sum_{m=1}^{6} e^{i(\boldsymbol{G}_m \cdot \boldsymbol{r} + \phi_{AB})}[1 + (-1)^m]/2\right] \\
&= V_{AB}^{M} \boldsymbol{\nabla}_{\boldsymbol{r}} \sum_{m=2,4,6} \cos(\boldsymbol{G}_m \cdot \boldsymbol{r} + \phi_{AB}) \\
&= V_{AB}^{M} \boldsymbol{\nabla}_{\boldsymbol{r}} \sum_{m=2,4,6} \cos(G_{mx}x + G_{my}y + \phi_{AB}) \\
&= -V_{AB}^{M} \sum_{m=2,4,6} \boldsymbol{G}_m \cdot \sin(\boldsymbol{G}_m \cdot \boldsymbol{r} + \phi_{AB}) \\
&= -V_{AB}^{M} \sum_{m=2,4,6} \sin(\boldsymbol{G}_m \cdot \boldsymbol{r} + \phi_{AB})\{G_{my}, G_{mx}, 0\}.
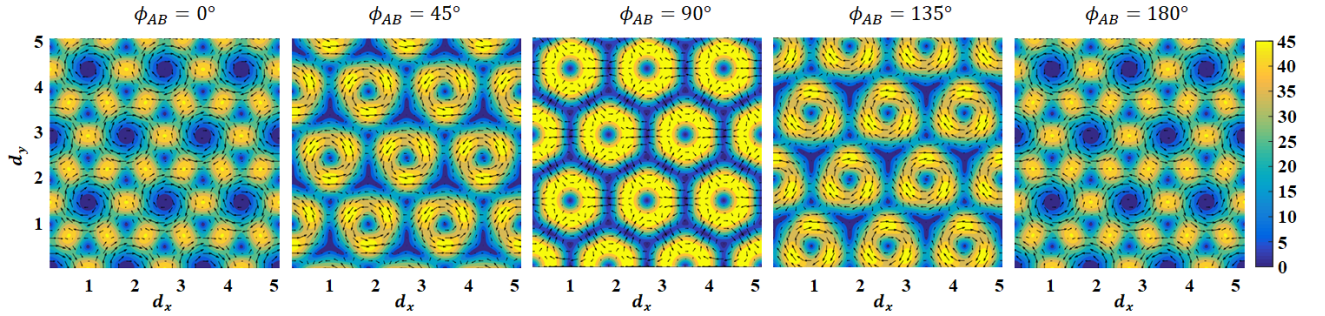\end{aligned}
\tag{4.11}
$$

Figure 4.7: *Dependence of the vector moiré potential $\mathbf{A}(\mathbf{r})$ on phase angle ϕ_{AB}. Due to the moiré superlattices, the inter-sublattice tunneling is behaving like a pseudo magnetic field (arrows) on a surface, which is strongly depends on the phase angle ϕ_{AB} at the Dirac point (See Eq.(4.11)). d_x and d_y are given in nm units.*

The variations of $\boldsymbol{A}^{\xi}(\boldsymbol{r})$ with $\{C_{AB}, \phi_{AB}\}$ and $V_{AA/BB}^{M}$ with $\{C_{AA/BB}, \phi_{AA/BB}\}$, which determine the Coulomb interactions, are determinant in the topological phase transitions that are manifested in the Chern diagrams that we develop in Chapter 6.

4.2 Methodological discussion for Chern diagrams

For a better understanding of the results described in section 6 (Chern diagrams), we will now delve into the procedure used to obtain the bands, the Bloch states and the Berry curvature. Additionally, prior to the presentation of results, we argue about the bands.

For a better understanding about the electronic structure of the model under effects of the off-diagonal moiré pattern that in equation (4.7), in Figure 4.8 we have varied the C_{AB} parameters to verify the effect it would have on the Chern number. In this regard, it is clear that there is a phase transition depending on the band and the C_{AB} value. Therefore, the pseudomagnetic vector potential could explain the phase shift of $|C| \leq N$ that we will see in detail in Chapter 6.

In line with Figure 4.8, in Figure 4.9 we show the band structure for the $\xi = 1$, $N = 3$ and $\Delta = 0.01$ eV configuration while varying the off-diagonal pseudomagnetic field with C_{AB} values
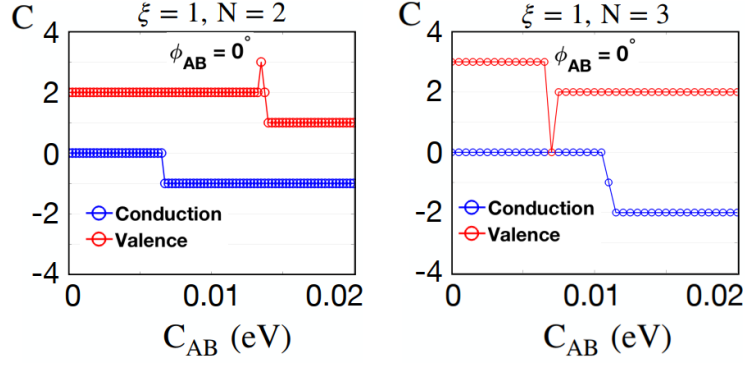
Figure 4.8: *Chern number as a function of C_{AB}, with $\phi_{AB} = 0$ for $N = 3$ and $N = 2$ for $\xi = 1$ and $\Delta = 0.01eV$.*

of $0\ eV$, $0.007\ eV$ and $0.01\ eV$. It is observed that there are changes in the bands, however, we obtained $C = 0$ in conduction band for the 3 cases, while in the conduction band C took the values of 0, 2 and 3 according to the value of C_{AB}.
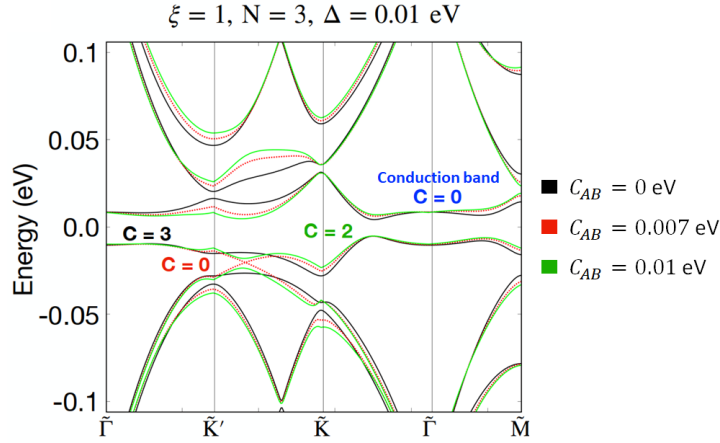

Figure 4.9: *Band structure for different C_{AB} values and 3 layers of graphene on boron nitride in ABC configuration.*

The topological bands are driven for $\Delta \neq 0$. The, under the electric field, the gap at the primary Dirac point and the gaps avoided at the limits of the mini-Brillouin zone (mBZ) of moiré isolate the low-energy bands near charge neutrality. These isolated bands lead the Berry curvatures and turn them to topological Chern bands. The Berry curvatures of the nth isolated bands are calculated using [119]

$$\mathcal{F}_n(\boldsymbol{k}) = -2 \sum_{n' \neq n} \text{Im} \left[\frac{\left\langle u_n \left| \frac{\partial H}{\partial k_x} \right| u_{n'} \right\rangle \left\langle u_{n'} \left| \frac{\partial H}{\partial k_y} \right| u_n \right\rangle}{(E_{n'} - E_n)^2} \right], \tag{4.12}$$

where for every $\boldsymbol{k}$-point we take sums through all the neighboring n' bands, the $|u_n\rangle$ are the moiré superlattice Bloch states and E_n are the eigenvalues. Note that equation 4.12 assumes the sum over the neighboring bands, which is based on the usefulness of this method for numerical calculations, in which the condition of a smooth phase choice of the eigenstates is not guaranteed in the standard diagonalization algorithms. This method is widely used to evaluate the Berry

curvature in crystals with the eigenfunctions provided from first principles calculations [120, 121]. The adiabatic approximation of the equation 4.12 can be considered as a projection operation, in other words, the dynamics of the system is restricted to the nth energy level. Therefore, the Berry curvature can be considered as the result of the "residual" interaction of these projected energy levels [119].

In Figure 4.10 we show the Berry curvature calculated from equation (4.12), where we can see that the three valence bands of Figure 4.9 for different values of C_{AB}. In this regard, we can see that the closure of the Band gap is associated with the topological phase transition and this takes place between $\tilde{K}$ and $\tilde{K}'$. From the Berry curvature, in Section 6 the Chern number of the nth band is obtained from $C = \int d^2\boldsymbol{k} \, \mathcal{F}_n(\boldsymbol{k})/(2\pi)$ integrated in the Brillouin zone.
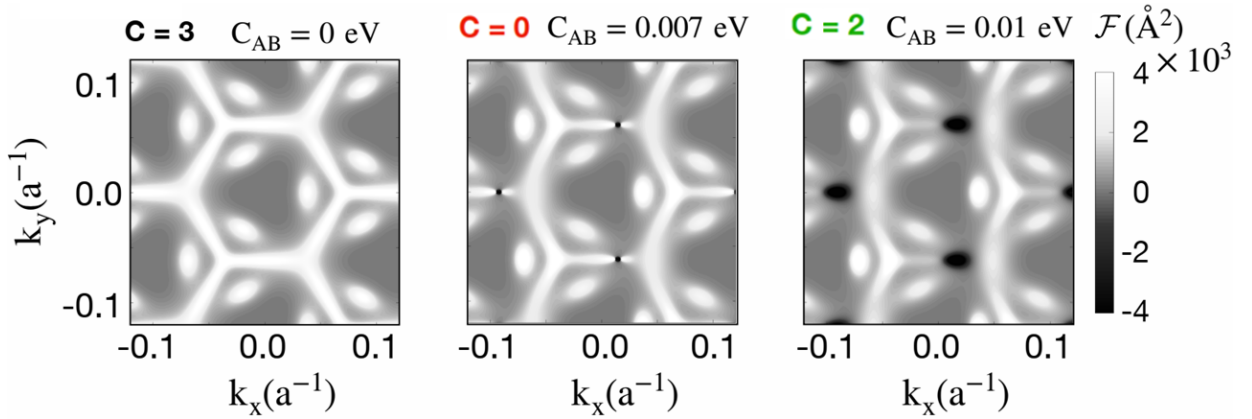

Figure 4.10: *Berry curvature for the three valence bands giving the different Chern numbers.*

Finally, we will discuss the effects of the magnetic vector potential on rotational symmetry. In Figure 4.11(a) we show the Fermi surface in the Van Hove singularity (vHS) for the conduction and valence bands. It is clear that there is a breaking of symmetry when $C_{AB} \neq 0$. This fact is reinforced when calculating the local density of states (LDOS) in real space, as shown in Figure 4.11(b).
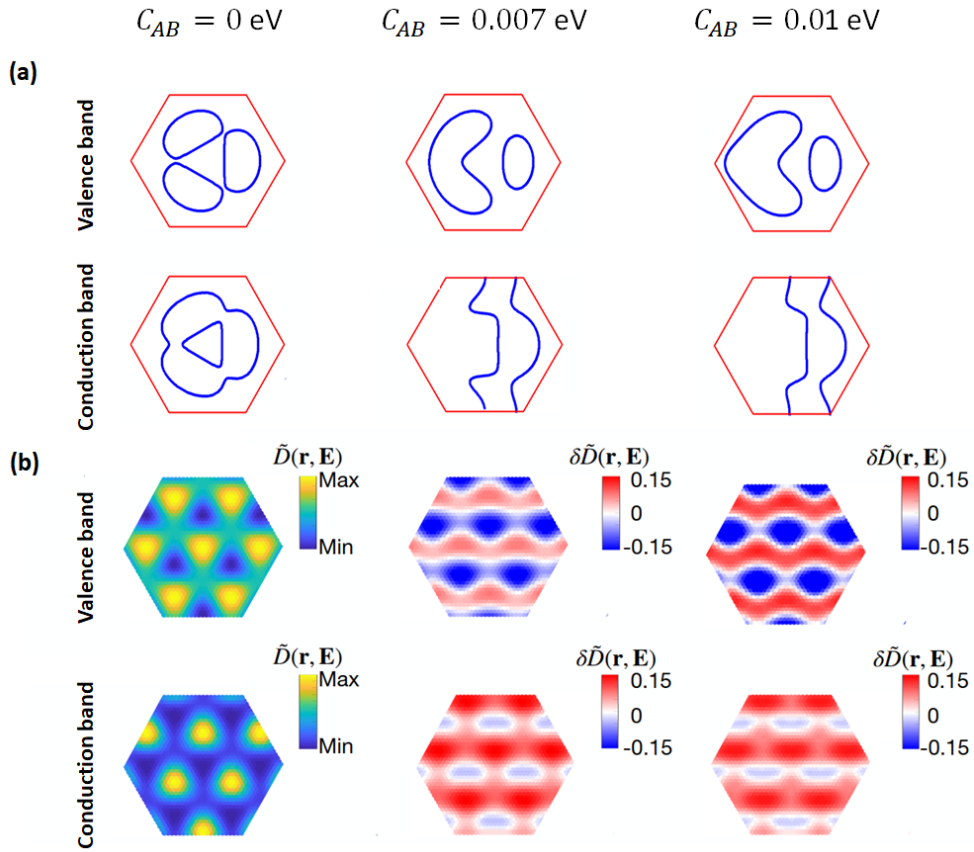
Figure 4.11: *Rotational symmetry breaking due to the effect of the magnetic vector potential. (a) Fermi surface contours in vHS for valence and energy conduction bands. (b) Representation in real space of the local density of states (LDOS) ($\tilde{D}(\boldsymbol{r}, E)$) in each vHS for conduction and valence bands where $\delta\tilde{D}(\boldsymbol{r}, E) = \tilde{D}_{C_{AB}\neq 0}(\boldsymbol{r}, E) - \tilde{D}_{C_{AB}=0}(\boldsymbol{r}, E)$ and the normalized LDOS defined by $\tilde{D}(\boldsymbol{r}, E) = D(\boldsymbol{r}, E/\max[D(\boldsymbol{r}, E)])$.*

Topological circuit of a non-Hermitian SSH quantum system

The SSH model [122] has been widely discussed in the literature [28,123]. It describes spinless hopping in a one-dimensional lattice, as we shown in figure 5.1. Here, we are interested in a new type of non-Hermitian SSH model with complex hoppings [124–126], and specifically in finding a circuit representation that helps us to model the different quantum phenomena and the topological properties.
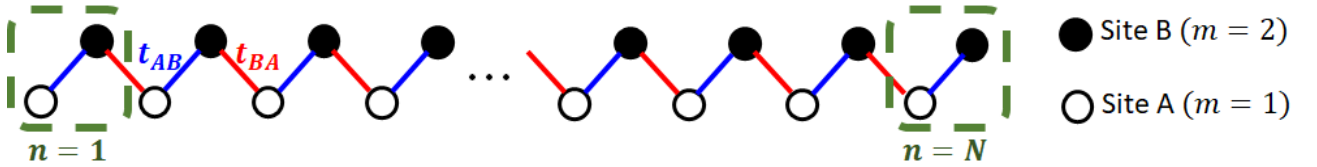

Figure 5.1: *SSH model of N cells and hoppings between sites A and B. Intracell hoppings (t_{AB}) with blue lines and intercell hoppings (t_{BA}) with red lines.*

The representation of quantum phenomena by means of electrical circuits has been recently proposed [127–129]. Topological aspects of the matter have also been modeled with electrical circuits, such as the phase transition in non-Hermitian systems [130] and Chern insulators [131]. In this chapter, we will take as a basis the existence of topological zero mode and the presence of chiral symmetry in non-Hermitian SSH chains. The usefulness of our model, that involves complex hoppings, is given by the possibility of developing long-range hopping in a topological interacting boson chains [125], polariton crystals [126], plasmon chain [124], among others.

Next, we will expose some basic aspects of the SSH model and its circuit representation. Subsequently, we will show the modification that we propose to represent the non-Hermitian SSH model with complex hopping that will allow us to analyze novel topological behaviors.

5.1 Hermitian SSH model

In an SSH chain, like the one shown in figure 5.1, the Hamiltonian is given by

$$\hat{H}_{\text{SSH}} = t_{AB} \sum_{n=1}^{N} \left(|n, B\rangle, \langle n, A| + h.c \right) + t_{BA} \sum_{n=1}^{N-1} \left(|n+1, A\rangle, \langle n, B| + h.c \right), \quad (5.1)$$

where the intracell hopping t_{AB} and the intercell hopping t_{BA} are positive and real. $|n, A\rangle$ and $|n, B\rangle$ with $n \in \{1, 2, \cdots, N\}$ are the states of the lattice where the electron is in a unit cell n, at the site of the sublattice A or B.

In the position space, the Hamiltonian (5.1) is written as a matrix of order $2N \times 2N$

$$H_{SSH} = \begin{pmatrix} 0 & t_{AB} & 0 & 0 & \cdots & 0 & 0 \\ t_{AB} & 0 & t_{BA} & 0 & \cdots & 0 & 0 \\ 0 & t_{BA} & 0 & t_{AB} & \cdots & 0 & 0 \\ \vdots & \vdots & \vdots & \vdots & \vdots & \vdots & \vdots \\ 0 & 0 & 0 & t_{AB} & \cdots & t_{AB} & 0 \end{pmatrix}. \tag{5.2}$$

From the Fourier transform, the Schrödinger equation that defines equation (5.1) in the momentum space is given by [?]

$$\hat{H}(k) \begin{bmatrix} a(k) \\ b(k) \end{bmatrix} = E(k) \begin{bmatrix} a(k) \\ b(k) \end{bmatrix}, \text{ with } \hat{H}(k) = \begin{pmatrix} 0 & t_{AB} + t_{BA}e^{-ik} \\ t_{AB} + t_{BA}e^{ik} & 0 \end{pmatrix}, \tag{5.3}$$

and $E(k) = \pm|t_{AB} + t_{BA}e^{-ik}| = \pm\sqrt{t_{AB}^2 + t_{BA}^2 + 2t_{AB}t_{BA}\cos k}$.

Based on tight binding approximation, Lee [129] and Zhao [128] represented a Hermitian SSH model using electrical circuits with LC components. Zhao used charge and electric flux concepts to deduce the Euler-Lagrange equations. The circuital Hermitian model corresponding to the SSH proposed by Zhao becomes in an LC circuit eigenvalue problem through

$$\left(\frac{\omega^2}{\omega_0^2} - \eta - \eta^{-1}\right) \begin{bmatrix} \varphi_1(k) \\ \varphi_2(k) \end{bmatrix} = \begin{pmatrix} 0 & -\frac{e^{-ik}}{\eta} - \eta \\ -\frac{e^{ik}}{\eta} - \eta & 0 \end{pmatrix} \begin{bmatrix} \varphi_1(k) \\ \varphi_2(k) \end{bmatrix}, \tag{5.4}$$

where $\eta = \sqrt{L_1/L_2}$, $\omega_0 = 1/(C\sqrt{L_1 L_2})$, C is the capacitance connected to ground, and L_i $i = 1, 2$ are the circuit inductors (see Fig. 5.2(a)). The two bands are defined by functions $\omega(k)$,

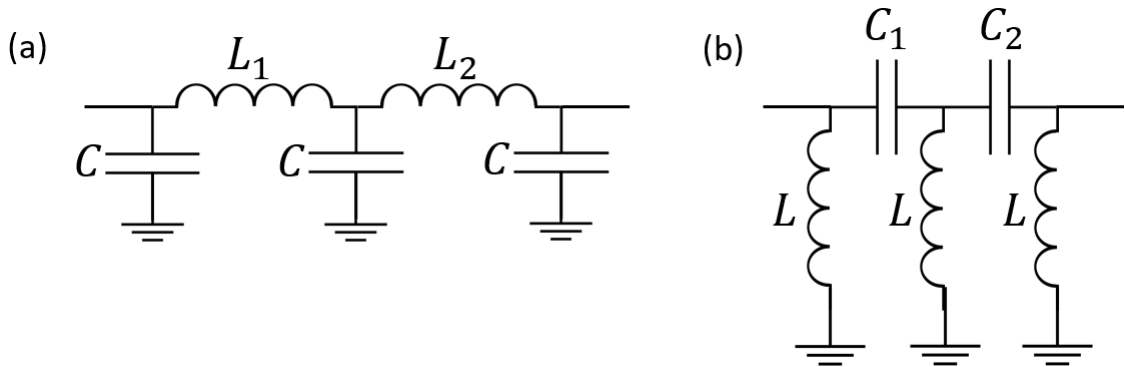$$\frac{\omega_\pm^2(k)}{\omega_0^2} = \eta + \eta^{-1} \pm \sqrt{\eta^2 + \eta^{-2} + 2\cos k}. \tag{5.5}$$

Figure 5.2: *SSH Hermitian circuit proposed by (a) Zhao [128] and (b) Lee et al. [129].*

In Zhao's model, ω_0 does not depend on ω. On the contrary, in our model ω_0 is a function of $\omega(k)$, as we will see in Section 5.2.

Lee *et al.* [129] proposed another Hermitian SSH circuit by swapping capacitor and inductor position relative to Zhao's model, as we show in Fig. 5.2(b). They studied Hermitian SSH chain topological properties by means of the analysis LC electrical circuit impedance with an external voltage source at frequency ω.

Despite the differences between Zhao and Lee's approaches, both models have positive real valued intra and inter-cell hopping correlated through an inverse function, since electrical circuit behavior is governed by the Laplacian, which is analogous to the Hamiltonian that describes the energy of a system [129, 132, 133].

Although the SSH model considers that t_{AB} and t_{BA} are real positives, what happens if these were complex quantities? That is, if these hopping had an associated magnitude and phase?. It is easy to verify that Hamiltonian (5.3) becomes non-Hermitian, also the (5.2) one.

5.2 Non Hermitian model of complex hopping

It is known that the behavior of an electrical circuit is described by its Laplacian, which is analogous to the Hamiltonian, and it describes the energy of the physical system [129, 132–134]. The Laplacian is defined by the structure of the circuit (electrical topology) and it is useful to represent admittance between nodes [132]. Our objective is to represent the topological behavior of a non-Hermitian system through the natural oscillation modes of an RLC circuit.

Thus, we propose a theoretical toy model that makes a bridge between electrical engineering and materials science. It is important to note that the tight binding approach is fundamental for the quantum behavioral representation of a crystal lattice [129, 133]. Therefore, the position eigenstates $|n, j\rangle$, and $j = A, B$, $n = 1, 2, \cdots, N$ are restricted to the lattice sites [63, 135]. In the following lines, we will show the link between these concepts.

To introduce the circuit notation, the impedance Z of an inductance L and a series configuration RC is given by $Z_L = i\omega L$ and $Z_{RC} = R + 1/i\omega C$, respectively. ω is the frequency of an oscillating driving voltage. The admittance is defined as $Y \equiv 1/Z$ and therefore, $Y_L = 1/i\omega L$ is the admittance of an inductor L and $Y_{RC} = \frac{1}{R+(i\omega C)^{-1}}$ is the admittance of a RC series branch.
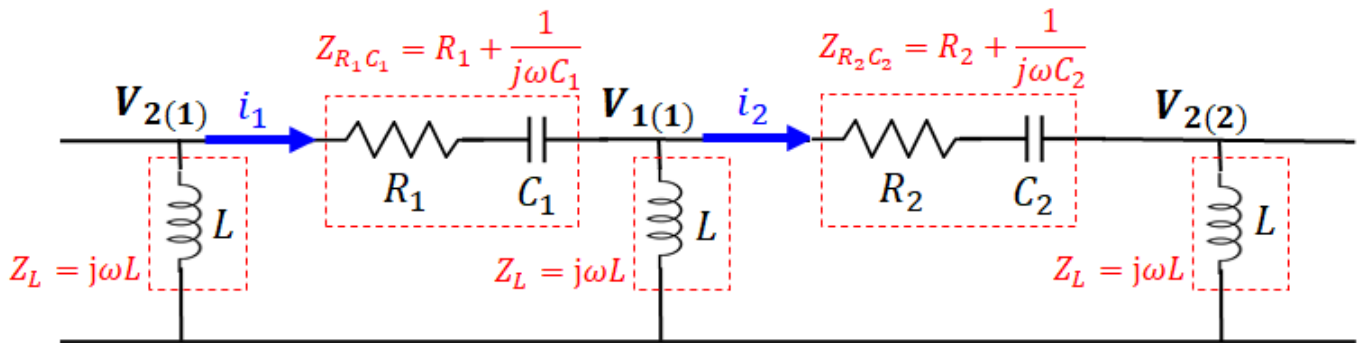

Figure 5.3: *Two-mesh RLC circuit.*

In figure 5.3, we show two meshes of an RLC circuit. The reason for the nomenclature in the voltage nodes will be understood when we make the link between the circuit behavior and a

crystalline lattice. The following equations are obtained from Kirchhoff's first law

$$
\begin{aligned}
i_1 =&[V_{2(1)} - V_{1(1)}]Y_{R_1C_1} = [V_{1(1)} - V_{2(2)}]Y_{R_2C_2} + V_{1(1)}Y_L, \\
i_2 =&[V_{1(1)} - V_{2(2)}]Y_{R_2C_2} = [V_{2(2)} - V_{1(2)}]Y_{R_1C_1} + V_{2(2)}Y_L.
\end{aligned}
\tag{5.6}
$$

As the Fourier transform generates a map in the spectrum of the k wave vector establishing a band structure of the admittances in the circuit and therefore in the lattice [133], we consider the transformations

$$
V_{j(n)}(t) = \frac{e^{-i\omega t}}{\sqrt{N}} \sum_k V_j'(k)e^{ikn},
\tag{5.7}
$$

with $j = 1, 2$. Therefore, we propose the following system of equations

$$
\begin{aligned}
0 =&V_1'\left(Y_{R_1C_1} + Y_{R_2C_2} + \frac{1}{i\omega L}\right) + V_2'\left(-Y_{R_1C_1} - Y_{R_2C_2}e^{ik}\right), \\
0 =&V_1'\left(-Y_{R_1C_1} - Y_{R_2C_2}e^{-ik}\right) + V_2'\left(Y_{R_1C_1} + Y_{R_2C_2} + \frac{1}{i\omega L}\right),
\end{aligned}
\tag{5.8}
$$

that can be written as

$$
\begin{pmatrix} 0 \\ 0 \end{pmatrix} = \begin{pmatrix} \frac{C_1}{\eta_1} + \frac{C_2}{\eta_2} - \frac{1}{\omega^2 L} & -\frac{C_1}{\eta_1} - \frac{C_2}{\eta_2}e^{-ik} \\ -\frac{C_1}{\eta_1} - \frac{C_2}{\eta_2}e^{ik} & \frac{C_1}{\eta_1} + \frac{C_2}{\eta_2} - \frac{1}{\omega^2 L} \end{pmatrix} \begin{pmatrix} V_1'(k) \\ V_2'(k) \end{pmatrix},
\tag{5.9}
$$

where $\eta_1 = i\omega R_1C_1 + 1$ and $\eta_2 = i\omega R_2C_2 + 1$. Note that due to there are $2N$ values of $j(n)$, also k is discretized in $2N$ values.

In particular, a hypothetical current I_j along node j is a component of vector $\boldsymbol{I}$ related to the vector of potential differences $\boldsymbol{V}$ by $\boldsymbol{I} = \mathcal{L}\boldsymbol{V}$, where $\mathcal{L}$ is the circuit Laplacian and it is related to the admittance between nodes; with $\mathcal{L} = D - C + W$, where D is a diagonal matrix containing admittances for each node, C is a matrix with zeroes on the diagonal and admittances between different nodes elsewhere, and W is a matrix that relates the admittances that lead to the ground [129]. Therefore, the Laplacian circuit of Figure 5.3 is given by

$$
\begin{aligned}
\mathcal{L} =& \begin{pmatrix} Y_{R_1C_1} + Y_{R_2C_2} + \frac{1}{i\omega L} & -Y_{R_1C_1} - Y_{R_2C_2}e^{ik} \\ -Y_{R_1C_1} - Y_{R_2C_2}e^{-ik} & Y_{R_1C_1} + Y_{R_2C_2} + \frac{1}{i\omega L} \end{pmatrix} \\
=& i\omega\left(\frac{C_1}{\eta_1} + \frac{C_2}{\eta_2} - \frac{1}{\omega^2 L}\right)\mathrm{I} - i\omega\left[\left(\frac{C_1}{\eta_1} + \frac{C_2}{\eta_2}\cos k\right)\sigma_x + \left(\frac{C_2}{\eta_2}\sin k\right)\sigma_y\right],
\end{aligned}
\tag{5.10}
$$

Comparing the non-Hermitian Laplacian (5.10) with Zhao and Lee *et al.*'s [128, 129], it coincides if $R_1 = R_2 = 0$, i.e., there are no dissipative elements. In other words, their Hemitian model is a particular case of ours when the circuit resistances are zero or approximately zero.

Then, we rewrite equation (5.9) as

$$
\left(\frac{1}{\omega^2 L} - \frac{C_1}{\eta_1} - \frac{C_2}{\eta_2}\right)\begin{pmatrix} V_1' \\ V_2' \end{pmatrix} = \begin{pmatrix} 0 & -\frac{C_1}{\eta_1} - \frac{C_2}{\eta_2}e^{-ik} \\ -\frac{C_1}{\eta_1} - \frac{C_2}{\eta_2}e^{ik} & 0 \end{pmatrix}\begin{pmatrix} V_1' \\ V_2' \end{pmatrix}.
\tag{5.11}
$$

It is important to note the mathematical similarity between the matrix on the right side of

equation (5.11) and the expression for $H(k)$ in equation (5.3), where

$$t_{AB} = -\frac{C_1}{\eta_1} = \sqrt{\frac{C_1^2}{1 + C_1^2 R_1^2 \omega^2}} e^{-i \arctan(C_1 R_1 \omega)}$$

$$t_{BA} = -\frac{C_2}{\eta_2} = \sqrt{\frac{C_2^2}{1 + C_2^2 R_2^2 \omega^2}} e^{-i \arctan(C_2 R_2 \omega)}.$$

(5.12)

Therefore, our model explicitly relates the hopping parameters with the circuit parameters, and additionally, the intra hopping is not necessarily the inverse of the inter hopping as in other models [128, 129], which gives us great versatility. Henceforth, we will call

$$\mathcal{Y}(k) = \begin{pmatrix} 0 & -\frac{C_1}{\eta_1} - \frac{C_2}{\eta_2} e^{-ik} \\ -\frac{C_1}{\eta_1} - \frac{C_2}{\eta_2} e^{ik} & 0 \end{pmatrix}$$

(5.13)

the admittance matrix for the non-Hermitian circuit.

Therefore, from equation (5.11), the eigenvalue

$$\Lambda(\omega) = \frac{1}{\omega^2 L} - \frac{C_1}{1 + i\omega R_1 C_1} - \frac{C_2}{1 + i\omega R_2 C_2}$$

(5.14)

is the sum of the admittances in each node and emulates the bulk bands, where the gap is 2Δ, with $\Delta = \min_k \Lambda$. In Figure 5.4, we make a relationship between the circuit model in Figure 5.3 and the SSH chain shown in Figure 5.1.
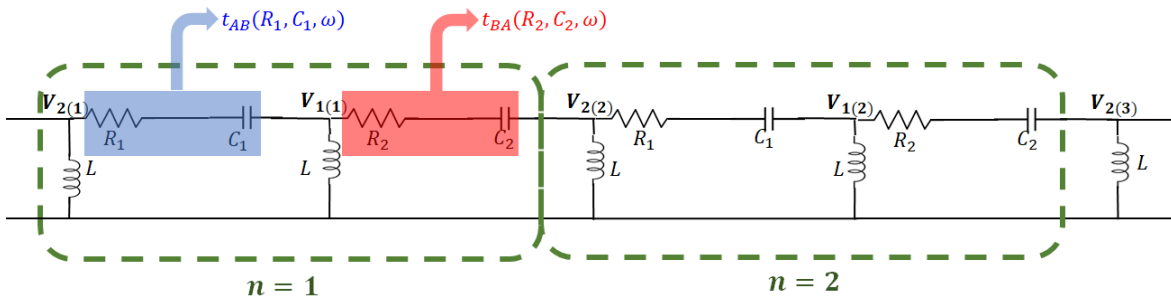

Figure 5.4: *SSH non-Hermitian topoelectric circuit. Each unit cell n consists of a pair of resistors and capacitors with the same inductor L between each RC array. Circuit elements with subscript 1 (highlighted in blue) represent intracell hoppings and circuit elements with subscript 2 (highlighted in red) represent intercell hoppings. An alternating voltage with frequency ω provides a driving voltage. We use the notation $V_{m(n)}$, where n is the cell and m the site.*

From equation (5.14), our system is massless when $L \to \infty$ and $C_i \to 0$. If that happens, the impedance of the circuit would become infinite and there would be no hoppings in the lattice. Therefore, under non-Hermiticity of the system, there is a gap in bulk when there are intra and inter-cell hoppings.

From equation (5.11), it is easy to show that the Bloch bands are obtained from the relation

$$\frac{\omega^2}{\omega_0^2} = \frac{1}{\gamma + \gamma^{-1} + \sqrt{\gamma^2 + \gamma^{-2} + 2\cos k}},$$

(5.15)

where $\omega_0^2 = \frac{\sqrt{\eta_1\eta_2}}{L\sqrt{C_1C_2}}$ and $\gamma = \sqrt{\frac{C_1\eta_2}{C_2\eta_1}}$. The equation (5.15) is a sixth degree for ω as a function of k. Two solutions correspond to bands in complex plane that are independent of the value of k. These two solutions are $\omega_1 = i/R_1C_1$ and $\omega_2 = i/R_2C_2$, and correspond to flat energy bands in the infinite ($\Lambda \to \infty$). Our analysis will focus on the other four solutions $\omega_i(k)$, $i = 3, 4, 5, 6$. Normal oscillation modes ω should not be confused with the number of oscillations in a decreasing complex exponential function from a source connected to the circuit. Rather, this term refers to the index of exponential functions that describe the natural source-free response when capacitors and/or inductors are charged [136].

Although (5.5) and (5.15) have similar mathematical structures, ω_0 is function of ω in (5.15), whereas this does not hold for (5.5). This dependence on ω makes a fundamental difference between Zhao's Hermitian system [128] and the non-Hermitian system proposed here, in addition to hopping properties.

In Chapter 7, we will do the analysis of the model that we explained here. Then, we will calculate the winding numbers, and the evidence of the skin effect, the bulk-edge correspondence, and other aspects of topology in non-Hermitian systems.

Part IV

Results

Chapter 6

Chern diagrams of N-Layer *ABC* graphene boron-nitride moiré superlattices

In this chapter, we will show the results that are derived from the theoretical aspects of Section 4, where we explained that the behavior of the moiré potential is dependent on the choice of C_μ and ϕ_μ for inter-sublatice interactions due to Coulomb interactions in moiré superlattices.

Here, we present the variations in Chern numbers for the N-rhombohedral layer of graphene on hexagonal boron-nitride (hBN) superlattices on the choice of moiré potential parameters. The arrangements of the graphene with boron nitride alignment, that is $\xi = 1$ implies that the potential $C_{BB} = 0$, while $\xi = -1$ implies that the potential $C_{AA} = 0$. Additionally, we include the off-diagonal moiré Hamiltonian terms $\{C_{AB}, \phi_{AB}\} \neq 0$ systematically to understand the new topological phases.

Next, we sweep through continuous values of C_{AA}, C_{BB}, C_{AB}, ϕ_{AA}, ϕ_{BB} and ϕ_{AB}, however, given the number of parameters and for an easy visualization of the Chern diagrams we will take as a basis the parameters $C_{AA} = -14.88$ meV, $C_{BB} = 12.09$ meV, $C_{AB} = 11.34$ meV, $\phi_{AA} = 50.195°$, $\phi_{BB} = -46.636°$ and $\phi_{AB} = 19.6°$ which were defined in recent theoretical works [89,111] that are related to experimental works of Chen *et al.* [137] and Kim *et al.* [138]. In particular, these parameters configure materials with large gaps at the Fermi level, where there are a perfect hBN-Graphene vertical interaction. In Chern diagrams, these values change when the hBN is not perfect or modified through strains, doping, imperfections, charges of B or N. The modified hBN has a different dielectric constant compared to the unmodified.

Before showing the results, in section 4.2 we will make a methodological description for obtaining the diagrams. Then, in section 6.1 we will show the Chern diagrams for $\xi = 1$ and in section 6.2 for $\xi = -1$. Since a contribution of our work is based on the implications of the moiré potentials in the Chern numbers for different configurations of graphene on boron nitride, in Section 6.3 we will describe the implications of including the moiré vector potential from equation (4.7). Finally, in Section 6.4 we summarize the diagrams described in the preceding sections and make some conclusions related to the physics of the diagrams.

6.1 Chern diagram for $\xi = 1$

For a configuration $\xi = 1$, we will vary the parameters of Hamiltonian (4.1), showing the effects on the Chern diagrams. Although here and section 6.2 we will describe the diagrams for

the configuration $\xi = 1$ and $\xi = -1$, respectively, in section 6.3 we will delve into the implications of the terms H_ξ^V and H_ξ^A related to moiré potentials.
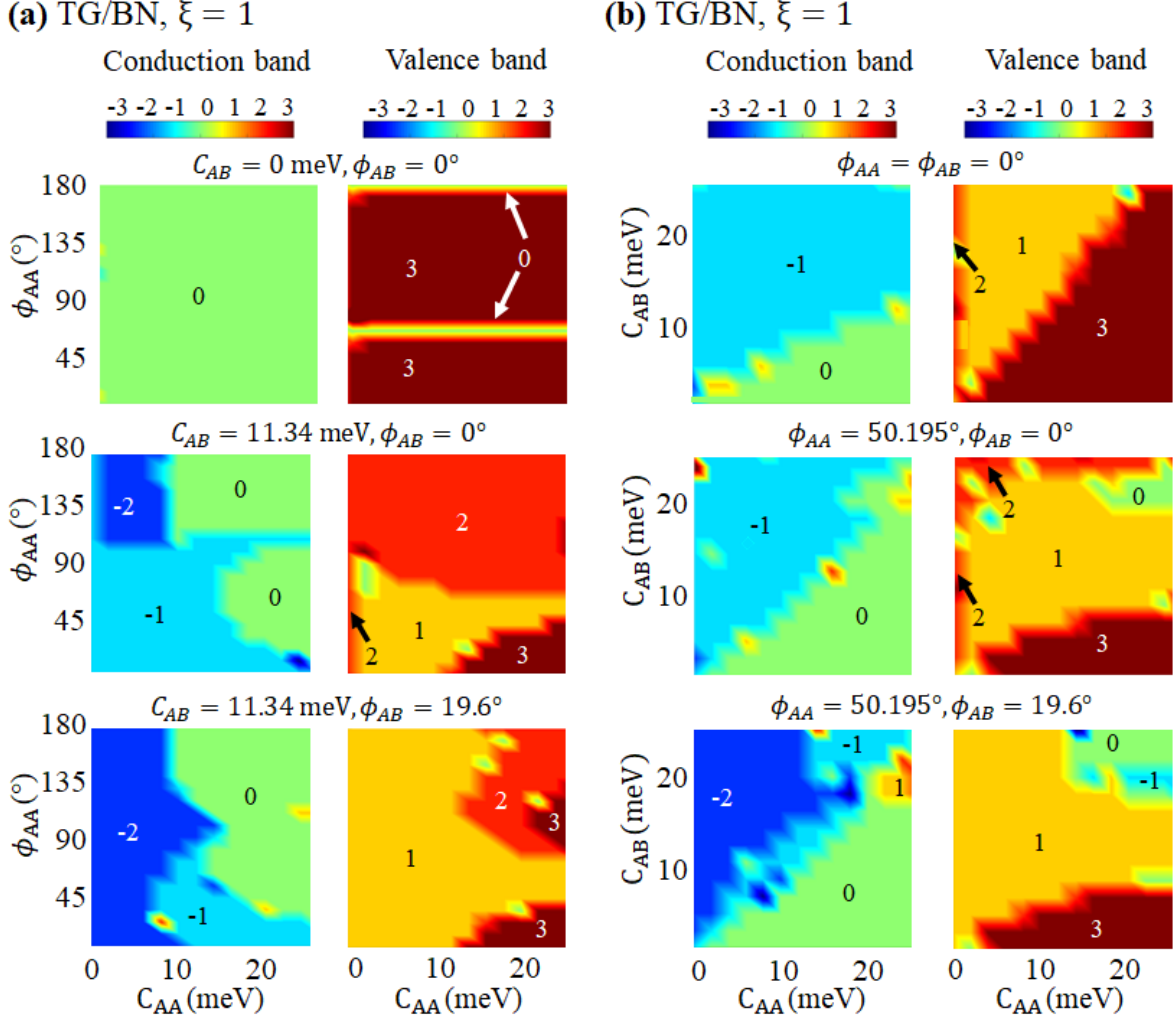

Figure 6.1: *The Chern number phase diagrams of valence and conduction bands for $N = 3$ layers of graphene with $\xi = 1$ alignment on BN. (a) For the parameter space $0 \leq C_{AA} \leq 25meV$, $0° \leq \phi_{AA} \leq 180°$. The top left two panels are obtained with $C_{AB} = 0meV$, $\phi_{AB} = 0°$, the middle left two panel are obtained with $C_{AB} = 11.34meV$, $\phi_{AB} = 0°$ and the bottom left two panels are obtained with $C_{AB} = 11.34meV$, $\phi_{AB} = 19.6°$. (b) for the parameter space $0 \leq C_{AA} \leq 25meV$, $0 \leq C_{AB} \leq 25meV$, the top right two panels are obtained with $\phi_{AA} = \phi_{AB} = 0°$, the middle right two panels are obtained with $\phi_{AA} = 50.195°$, $\phi_{AB} = 0°$, and the bottom right two panels are obtained with $\phi_{AA} = 50.195°$, $\phi_{AB} = 19.6°$.*

For $\phi_{AA} = \phi_{AB} = 0$, the numerical calculations for TG/BN with variation of C_{AA}, C_{AB} with $\phi_{AA} = \phi_{AB} = 0°$ shows Chern number of 0 or -1 in the conduction band and 1, 2 or 3 for the valence band from the C_{AA} and C_{AB} values, as we show in the upper panel of Figure 6.1(b). For smaller values of C_{AB} with increasing value of C_{AA}, it shows Chern value of $C = 0$ for conduction band and $C = 3$ for valence band. Under the same conditions, for BG/BN, the conduction band shows the topological phase of -1 even for a very small value of C_{AB} unlike TG/BN (see the top two panels in Figure 6.2(b)). However, the valence band is consistent with Chern value $C = 2$ when $C_{AA} > C_{AB}$ in the range of 0 to 25 meV. The G/BN has a different behavior as compared
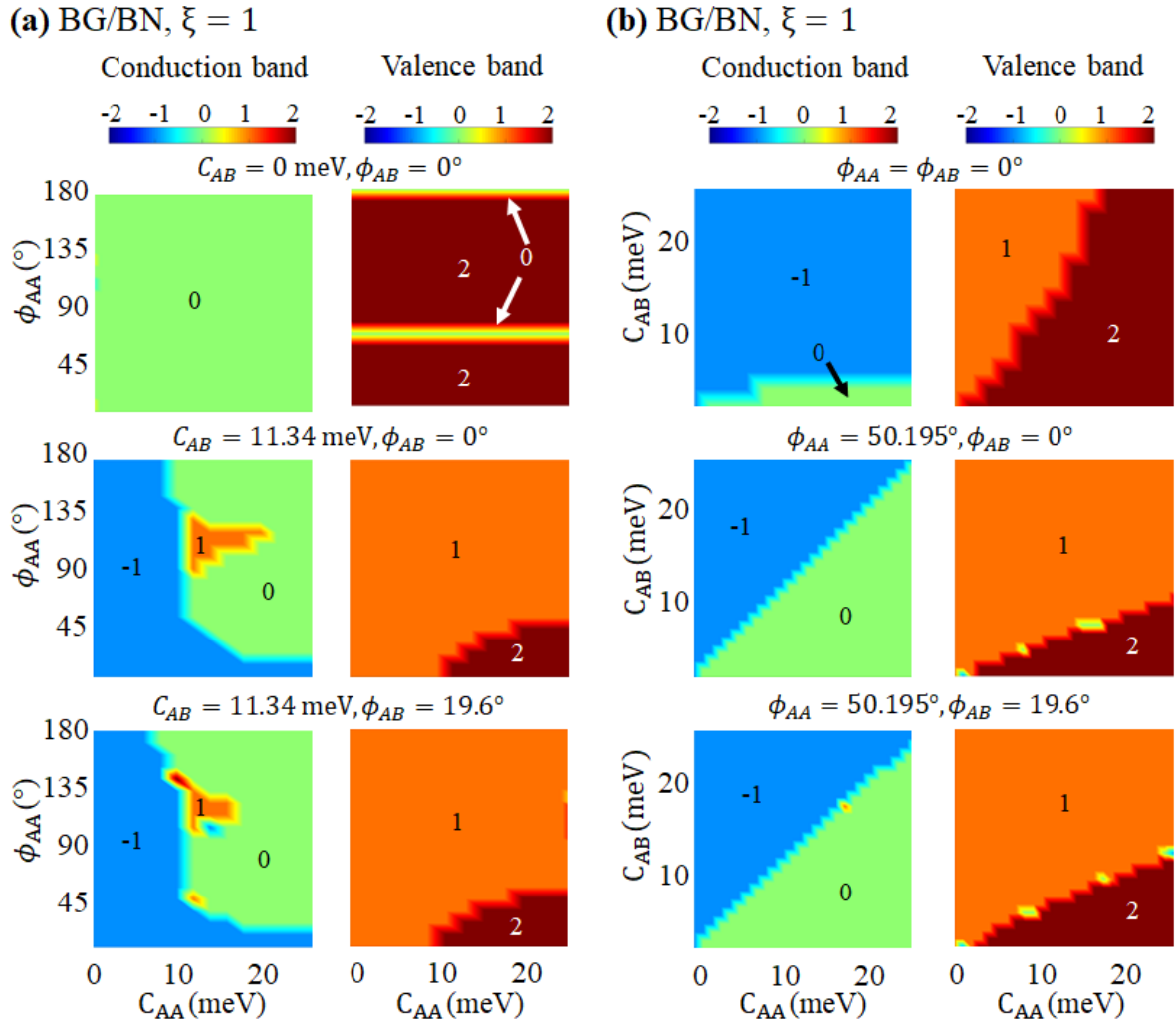
(a) BG/BN, $\xi = 1$

Conduction band   Valence band

(b) BG/BN, $\xi = 1$

Conduction band   Valence band

Figure 6.2: *The Chern number phase diagrams of valence and conduction bands for $N = 2$ layers of graphene with $\xi = 1$ alignment on BN. (a) For the parameter space $0 \leq C_{AA} \leq 25meV$, $0° \leq \phi_{AA} \leq 180°$. The top left two panels are obtained with $C_{AB} = 0meV$, $\phi_{AB} = 0°$, the middle left two panel are obtained with $C_{AB} = 11.34meV$, $\phi_{AB} = 0°$ and the bottom left two panels are obtained with $C_{AB} = 11.34meV$, $\phi_{AB} = 19.6°$. (b) for the parameter space $0 \leq C_{AA} \leq 25meV$, $0 \leq C_{AB} \leq 25meV$, the top right two panels are obtained with $\phi_{AA} = \phi_{AB} = 0°$, the middle right two panels are obtained with $\phi_{AA} = 50.195°$, $\phi_{AB} = 0°$, and the bottom right two panels are obtained with $\phi_{AA} = 50.195°$, $\phi_{AB} = 19.6°$.*

to TG/BN and BG/BN. The topological bands are driven only for higher values of C_{AA} and C_{AB}, moreover, the Chern values are shifted as compared to previous cases like now conduction band show a Chern value of $C = 1$ and the valence band is $C = -1$ (see the top two panels in Figure 6.3(b)).

When we include a phase of $\phi_{AA} = 50.195°$ but keeping $\phi_{AB} = 0$, in the TG/BN case it increases the area of a trivial phase in the conduction band, such that $C = 0$ if $C_{AA} > C_{AB}$ for $0 < C_{AA} < 25meV$. On the other hand, the phase $\phi_{AA} = 50.195°$ reduces the area where $C = 3$ in the conduction band. In Figure 6.1(b)(see the middle two panels), the conduction band has Chern values of $C = \{-1, 0\}$ and the valence band $C = \{0, 1, 2, 3\}$. For the case of BG/BN, in Figure 6.2(b)(see the middle two panels), when $C_{AB} = 0$ the conduction band has $C = 0$ and the
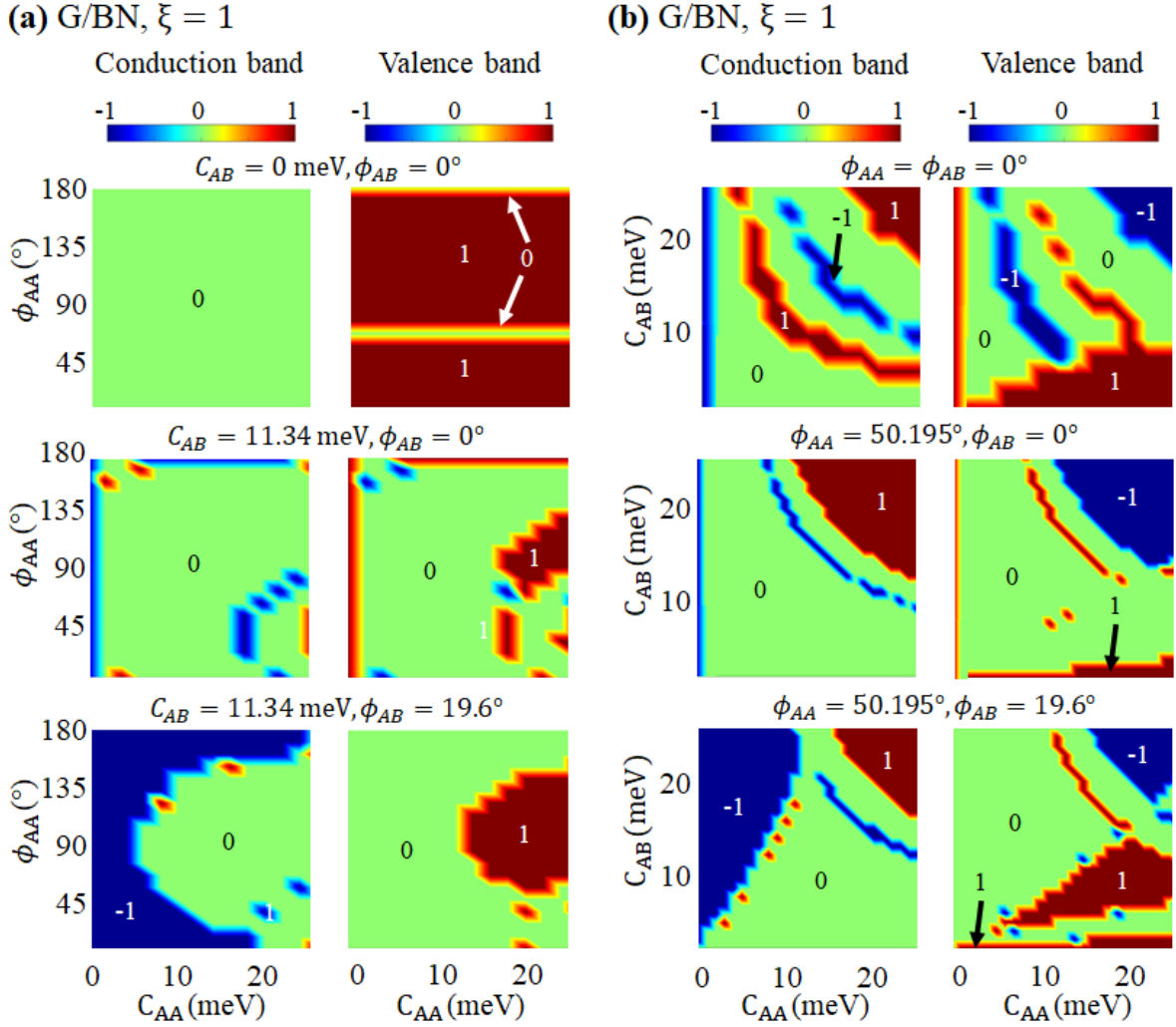
Figure 6.3: *The Chern number phase diagrams of valence and conduction bands for $N = 1$ layers of graphene with $\xi = 1$ alignment on BN. (a) For the parameter space $0 \leq C_{AA} \leq 25 meV$, $0° \leq \phi_{AA} \leq 180°$. The top left two panels are obtained with $C_{AB} = 0 meV$, $\phi_{AB} = 0°$, the middle left two panel are obtained with $C_{AB} = 11.34 meV$, $\phi_{AB} = 0°$ and the bottom left two panels are obtained with $C_{AB} = 11.34 meV$, $\phi_{AB} = 19.6°$. (b) for the parameter space $0 \leq C_{AA} \leq 25 meV$, $0 \leq C_{AB} \leq 25 meV$, the top right two panels are obtained with $\phi_{AA} = \phi_{AB} = 0°$, the middle right two panels are obtained with $\phi_{AA} = 50.195°$, $\phi_{AB} = 0°$, and the bottom right two panels are obtained with $\phi_{AA} = 50.195°$, $\phi_{AB} = 19.6°$.*

valence band $C = 2$ for any value of C_{AA}. On the other hand, when $C_{AA} = 0$, then $C = -1$ in the conduction band and $C = 1$ in the valence band. An interesting effect, which was also observed in the TLG/BN case, is that for BLG/BN the inclusion of the $\phi_{AA} = 50.195°$ phase, increases the area of $C = 0$ in the conduction band for $C_{AA} > C_{AB}$ and also reduce the area of $C = 2$ for $0 < C_{AA} < 25$ meV. In the case of G/BN, the inclusion of the $\phi_{AA} = 50.195°$ phase is manifested with the increase of the area where $C \neq 0$ for both bands, as we show in Figure 6.3(b) (see the two middle panels).

The inclusion of two additional phases, $\phi_{AA} = 50.195°$ and $\phi_{AB} = -19.6°$, allows us to obtain new phases in graphene boron-nitride moiré superlattices. For the case of TG/BN (see the two bottom panels of Figure 6.1(b)), it shows important variations, especially when the value of C_{AB}

increases. In the conduction band, a $C = -2$ appears in the area where before $C = -1$ when $\phi_{AB} = 0$. On the other hand, the valence band shows the absence of a $C = 2$. In the BG/BN case, it is not very sensitive to the phase ϕ_{AB}. In other words, there is no apparent difference between the second and third rows of Figure 6.2(b). In G/BN case, for limited range of parameters space has shown the topological bands, and another region the bands turns out to be trivial, as we can see when comparing rows 2 and 3 of figure 6.3(b).

In summary, if the phases $\phi_{AA} = \phi_{AB} = 0°$ and also $C_{AB} = 0$, then $C = 0$ in the conduction band and $C = N$ in the valence band. Additionally, under the same conditions in the phases, if $C_{AA} = 0$ then the Chern number in the conduction band is given by $C = -1$ and in the valence band $C = N - 1$ (except for $N = 1$ where $C = N$), for any value of C_{AB}.

When $\phi_{AA} \neq 0$, keeping the phase $\phi_{AB} = 0$, does not substantially alter the conclusions that we make in the case of $\phi_{AA} = \phi_{AB} = 0$, since when $C_{AB} = 0$ then $C = 0$ in the conduction band and $C = N$ in the valence band, but when $C_{AA} = 0$ then $C = -1$ in the conduction band and $C = N - 1$ in the valence band, except for G/BN where $C = N$. Finally, it can be seen that despite the inclusion of a $\phi_{AB} \neq 0$, when $C_{AB} = 0$ then $C = 0$ in the conduction band and $C = N$ in the valence band. However, when $C_{AA} = 0$ it is no longer true that $C = -1$ for the conduction band and that $C = N - 1$ for the valence band.

6.2   Chern diagram for $\xi = -1$

Taking into account that in section 6.1 we made a detailed analysis of the Chern diagrams with $\xi = 1$, below we will highlight the most interesting and important aspects of the $\xi = -1$ configuration. In this section we will refer to Figures 6.4, 6.5, and 6.6.

In general terms, when $C_{AB} = 0$ and $\phi_{BB} = \phi_{AB} = 0$ then $C = 0$ in the valence band and $C = -N$ in the conduction band. On the other hand, when $C_{BB} = 0$ but $C_{AB} \neq 0$ then $C = -1$ in the conduction band and $C = N - 1$ in the valence band. However, for the case of G/BN, $C = 0$ (i.e. N-1) in the valence band only when $C_{AB} < 11$meV.

Although in the first instance one could think of the existence of a certain symmetry between the configuration $\xi = 1$ and $\xi = -1$, the binding energy between carbon and boron or nitrogen atoms are different and depends on the distance to each atom. For greater clarity on this point, it is suggested to see figures 4.2 and 4.3.

Since our interest is in the analysis and implications of scalar and vector moiré potential, in section 6.3, we will do a more specific analysis of the inclusion of the terms C_{AB} and ϕ_{AB}, to understand their role in the construction of Chern diagrams.

6.3   Addition of off-diagonal terms

Next, we will vary the parameters C_{AB} and ϕ_{AB} in the Hamiltonian (4.1) and we will show how the different topological phases change. We have showed earlier that the ϕ_{AB} angle has important implications in the symmetric or antisymmetric behavior of the components of the moiré band Hamiltonian (Eq.(4.7)). Additionally, when the moiré potential is included with a ϕ_{AB} phase in the Hamiltonian, then new topological phases appear.

Figure 6.4: *The Chern number phase diagrams of valence and conduction bands for $N = 3$ layers of graphene with $\xi = -1$ alignment on BN. (a) For the parameter space $0 \leq C_{AA} \leq 25meV$, $0° \leq \phi_{AA} \leq 180°$. The top left two panels are obtained with $C_{AB} = 0meV$, $\phi_{AB} = 0°$, the middle left two panel are obtained with $C_{AB} = 11.34meV$, $\phi_{AB} = 0°$ and the bottom left two panels are obtained with $C_{AB} = 11.34meV$, $\phi_{AB} = 19.6°$. (b) for the parameter space $0 \leq C_{AA} \leq 25meV$, $0 \leq C_{AB} \leq 25meV$, the top right two panels are obtained with $\phi_{AA} = \phi_{AB} = 0°$, the middle right two panels are obtained with $\phi_{AA} = 50.195°$, $\phi_{AB} = 0°$, and the bottom right two panels are obtained with $\phi_{AA} = 50.195°$, $\phi_{AB} = 19.6°$.*

When $C_{AB} = 0$ and $\phi_{AB} = 0$, for a specific configuration, i.e $\xi = 1$, numerical calculations in the valence band for TG/BN predict a Chern number $C = \pm 3$, for BG/BN it is $C = \pm 2$ and for G/BN it is $C = \pm 1$ [111]. In the top left two panels of the Figures 6.1(a), 6.2(a) and 6.3(a), the conduction band has Chern number $C = 0$ and the valence band has Chern number of $C = N$. It is noted that when the off-diagonal terms are zero, the Chern numbers are insensitive to the scalar moiré potential parameter space. Interestingly, for $\phi_{AA} \sim 60°$ & $180°$ the valence band Chern number $C = 0$. We further show that the Chern number variation is more sensitive to the moiré potential terms than to the number of layers.

For the TG/BN case (see the middle left two panels of Figure 6.1(a)), the conduction band changes the Chern value from $C = 0$ to $C = -1$ with the addition of $C_{AB} \neq 0$. It also shows
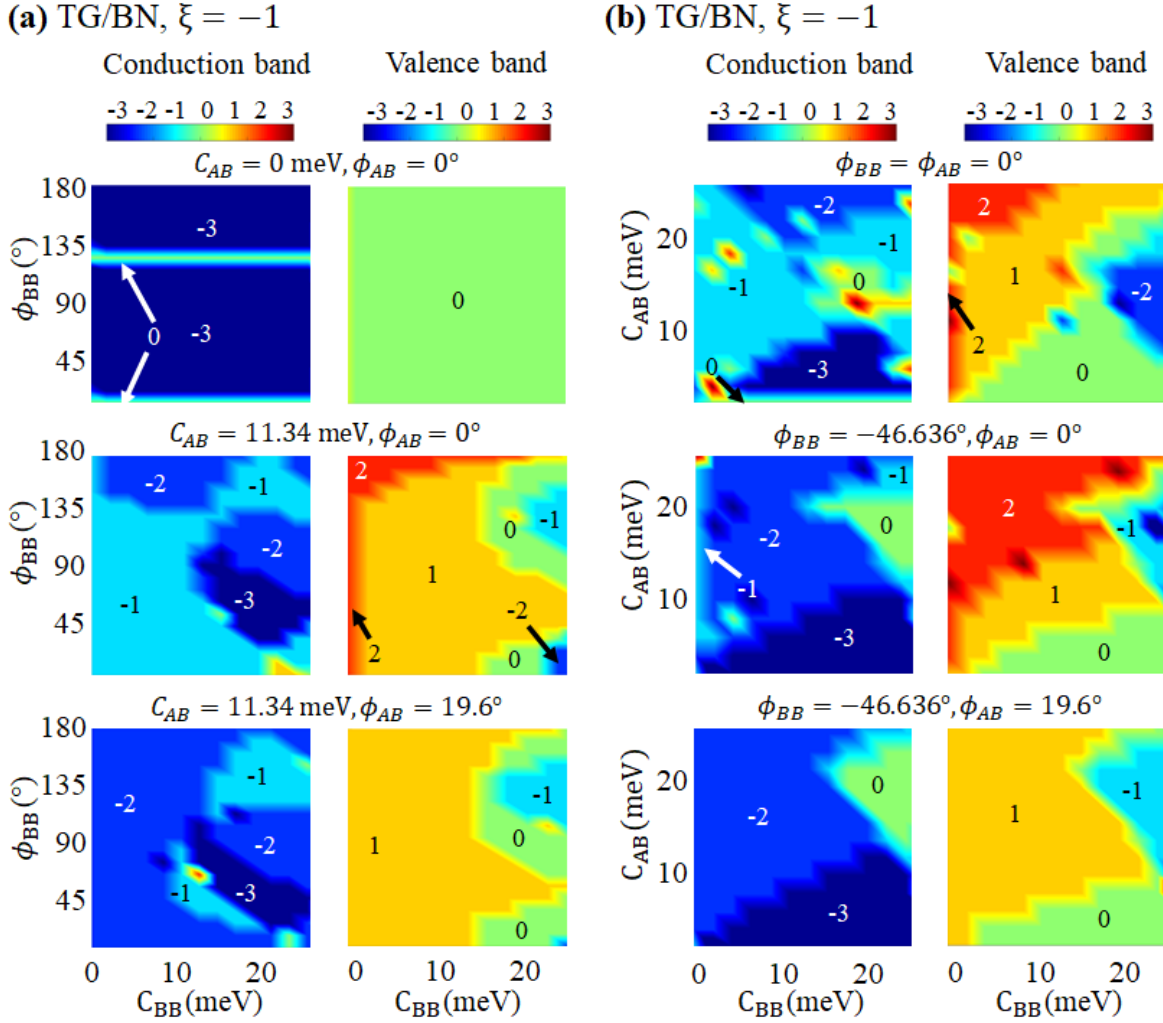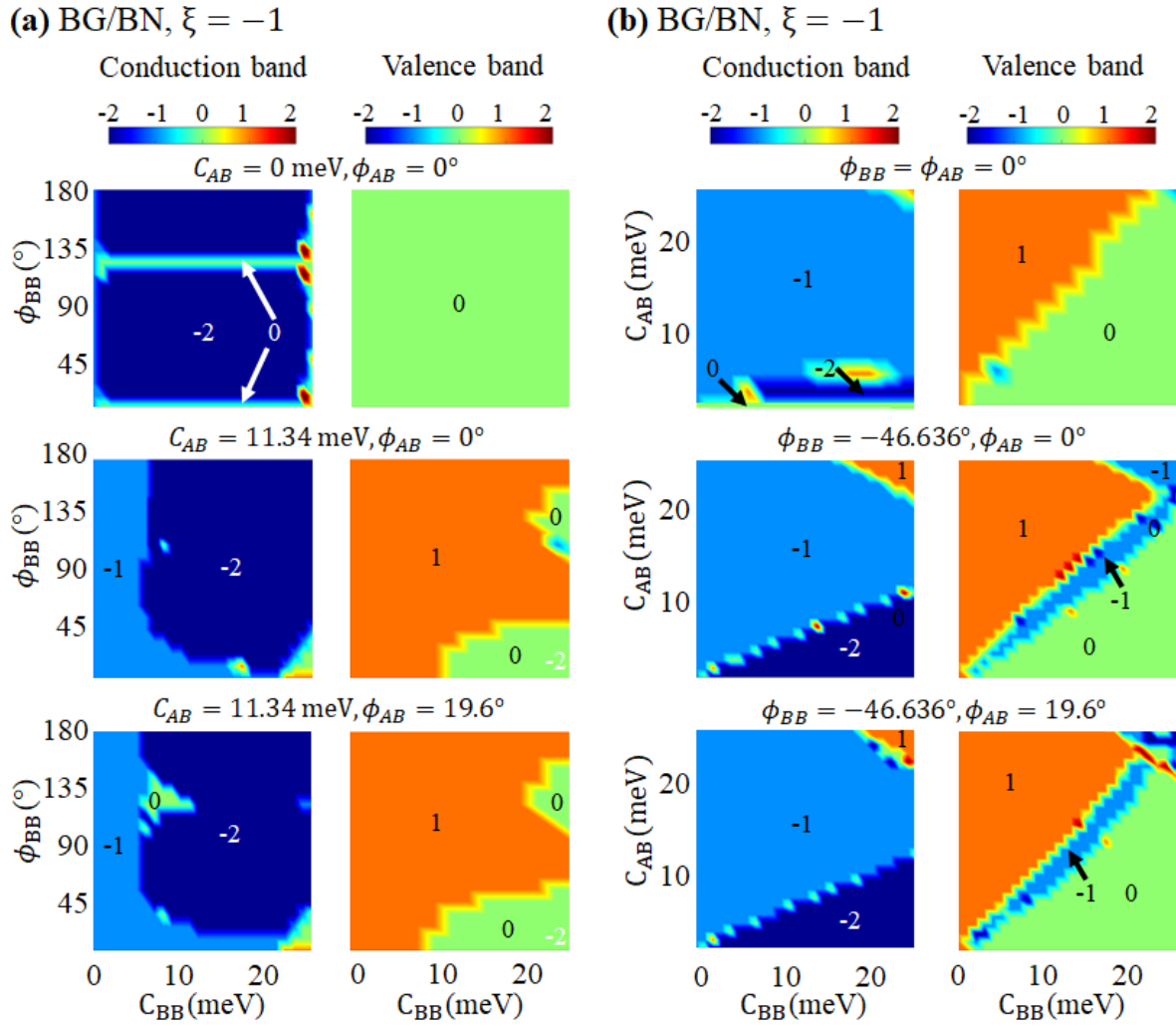
Figure 6.5: *The Chern number phase diagrams of valence and conduction bands for $N = 2$ layers of graphene with $\xi = -1$ alignment on BN. (a) For the parameter space $0 \leq C_{AA} \leq 25 meV$, $0° \leq \phi_{AA} \leq 180°$. The top left two panels are obtained with $C_{AB} = 0 meV$, $\phi_{AB} = 0°$, the middle left two panel are obtained with $C_{AB} = 11.34 meV$, $\phi_{AB} = 0°$ and the bottom left two panels are obtained with $C_{AB} = 11.34 meV$, $\phi_{AB} = 19.6°$. (b) for the parameter space $0 \leq C_{AA} \leq 25 meV$, $0 \leq C_{AB} \leq 25 meV$, the top right two panels are obtained with $\phi_{AA} = \phi_{AB} = 0°$, the middle right two panels are obtained with $\phi_{AA} = 50.195°$, $\phi_{AB} = 0°$, and the bottom right two panels are obtained with $\phi_{AA} = 50.195°$, $\phi_{AB} = 19.6°$.*

a topological phase transition with the variation of ϕ_{AA} with the Chern value $C = -2$ in the conduction band. However, for the higher values of C_{AA}, the Chern value of conduction band show $C = 0$. For the valence band, the Chern values shift from $C = 3$ to $C = \{1, 2, 3\}$, and it has a topological phase transition with the variation of ϕ_{AA}. Figure 6.7(a-b) (first row) shows the behavior when C_{AB} and ϕ_{AB} vary. In accordance with the preceding sections when $C_{AB} = 0$ and $\xi = 1$ then $C = 0$ in the conduction band and $C = N$ in the valence band. But if $\xi = -1$, then $C = -N$ in the conduction band and $C = 0$ in the valence band. On the other hand, from the same figure 6.7, it is clear that in the TLG/BN case the variations of the Chern number with the ϕ_{AB} phase do not occur for small values of C_{AB}.

For the cases BG/BN and G/BN, new topological phases appear by the addition of the moiré
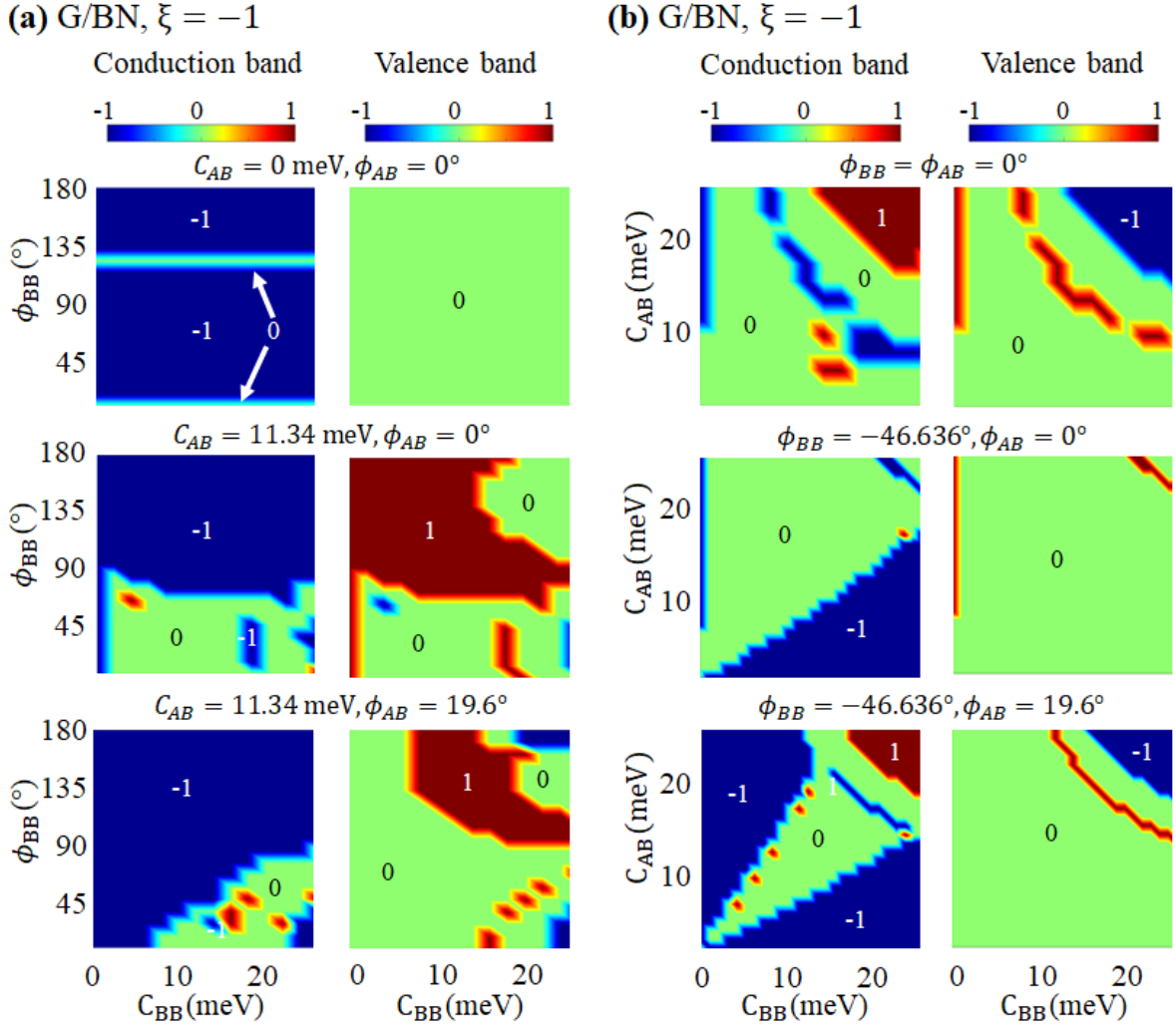
Figure 6.6: *The Chern number phase diagrams of valence and conduction bands for $N = 1$ layers of graphene with $\xi = -1$ alignment on BN. (a) For the parameter space $0 \leq C_{AA} \leq 25meV$, $0° \leq \phi_{AA} \leq 180°$. The top left two panels are obtained with $C_{AB} = 0meV$, $\phi_{AB} = 0°$, the middle left two panel are obtained with $C_{AB} = 11.34meV$, $\phi_{AB} = 0°$ and the bottom left two panels are obtained with $C_{AB} = 11.34meV$, $\phi_{AB} = 19.6°$. (b) for the parameter space $0 \leq C_{AA} \leq 25meV$, $0 \leq C_{AB} \leq 25meV$, the top right two panels are obtained with $\phi_{AA} = \phi_{AB} = 0°$, the middle right two panels are obtained with $\phi_{AA} = 50.195°$, $\phi_{AB} = 0°$, and the bottom right two panels are obtained with $\phi_{AA} = 50.195°$, $\phi_{AB} = 19.6°$.*

vector potential C_{AB}. The Chern number phase diagrams for BG/BN case are shown in Figure 6.2(a) where we can see that the inclusion of a $\phi_{AB} = 19.6°$ phase does not alter significantly the Chern diagram. A different behavior shows the Figure 6.3(a) where in G/BN case the Chern diagrams show new topological phases in conduction band with $\phi_{AB} = 19.6°$. From Figure 6.7 (second row panels) it is clear that in the BG/BN case, there is a low variation of the Chern number with the variation of ϕ_{AB}, while in the G/BN case (third row of figure 6.7) the variations of ϕ_{AB} (keeping the same value of C_{AB}), noticeably change the value of the Chern number.
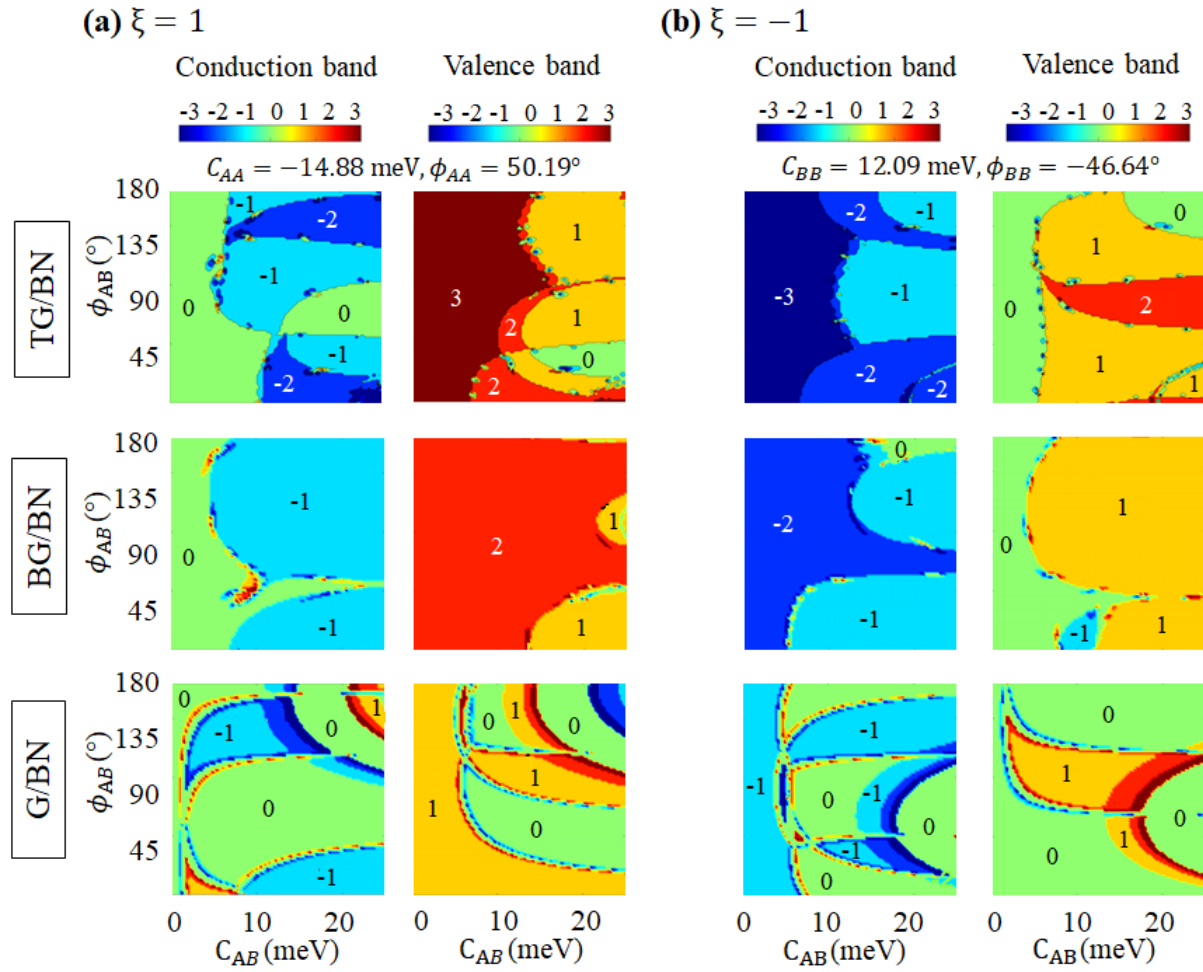
Figure 6.7: *The Chern number phase diagrams of valence and conduction bands for the $N = \{1, 2, 3\}$ layers of graphene on BN for parameter space $0 \leq C_{AB} \leq 25$ meV and $0° \leq \phi_{AB} \leq 180°$ with alignment (a) $\xi = 1$ with parameters $C_{AA} = -14.88$ meV, $\phi_{AA} = 50.19°$ and (b) $\xi = -1$ with parameters $C_{BB} = 12.09$ meV, $\phi_{BB} = -46.64°$.*

6.4   Summary and analysis of Chern diagrams for 1, 2 and 3 layers of ABC-graphene on hBN moire superlattices

It is known that the configurations of 1, 2 or 3 layers graphene on boron nitride host nearly flat topological bands that present spontaneous quantum Hall phases, under an appropriate polarization [93, 111, 139]. From the low-energy model for rhombohedral N-layer graphene ($N = 1, 2, 3$) aligned with hexagonal boron-nitride we verify the importance of the off-diagonal moiré vector potential terms in the configuration of the valley Chern numbers. The terms H_ξ^A and H_ξ^V tends to be overlooked in the literature and those are a possibly explanation for recent experiments for hBN aligned graphene trilayers where $C = 3$ was expected but signatures of $C = 2$ were obtained [102]. Thus, our analyzes suggest that the topological phase transitions of flat bands can be triggered by pseudomagnetic vector field potentials associated with moire strain patterns.

In this work, we have verified that there is a proportionality of $|C| = N$ in the valence or conduction band depending on the configuration $\xi = \pm 1$. According to Chittari *et al.* [111], the

Chern number that is obtained for each combination of parameters is due to the contribution of the primary (due to interlayer potential difference) and secondary (due to moiré potential parameters) Chern weight, $C^{e/h} = w_P^{e/h} + w_S^{e/h}$, where the superscripts e and h refer to electrons and holes, respectively.

As can be seen from figures 6.1, 6.2, and 6.3 for $\xi = 1$ and 6.4, 6.5, and 6.6 for $\xi = -1$, the off-diagonal interlayer coherence moiré pattern term given by $C_{AB} \neq 0$ modifies the Chern diagram, such that $|C| \leq N$. This behavior is due to the moiré vector potential term H_ξ^A of equation (4.7) that we show in figure 4.7 and that defines a pseudospin field of graphene on hBN.Therefore, the introduction of the off-diagonal interlayer coherence moiré patter terms through the C_{AB} magnitude and the phase ϕ_{AB} allows to trigger topological phase transitions. From our results, the vector potential moiré patterns should no longer be ignored in the low energy Hamiltonian models of N-chiral multilayer of graphene on BN superlattices.

As a summary, in tables 6.1, 6.2 and 6.3 we summarize the possible Chern numbers in the conduction and valence bands for potential magnitudes between 0 and 25 meV and phase between 0 and π, according to the ξ alignment and the presence or absence of the potential vector moiré patterns.

| | If $C_{AB} = 0$ | | | |
| | $\xi = 1$ $(C_{AA} \neq 0)$ | | $\xi = -1$ $(C_{BB} \neq 0)$ | |
	Conduction	Valence	Conduction	Valence
TG/BN	0	3	-3	0
BG/BN	0	2	-2	0
MG/BN	0	1	-1	0

Table 6.1: *Chern number with $C_{AB} = 0$ for the alignment $\xi = \pm 1$.*

| | If $C_{AB} \neq 0$ and $\phi_{AB} = 0$ | | | |
| | $\xi = 1$ $(C_{AA} \neq 0)$ | | $\xi = -1$ $(C_{BB} \neq 0)$ | |
	Conduction	Valence	Conduction	Valence
TG/BN	-3, -2, 0	2, 3	-3, -2	0, 1, 2
BG/BN	-1, 0	1, 2	-2, -1	-1, 0, 1
MG/BN	-1, 0, 1	1	-1, 0	0

Table 6.2: *Chern number with $C_{AB} \neq 0$ and $C_{AB} = 0$ for the alignment $\xi = \pm 1$*
.

| | If $C_{AB} \neq 0$ and $\phi_{AB} \neq 0$ | | | |
| | $\xi = 1$ $(C_{AA} \neq 0)$ | | $\xi = -1$ $(C_{BB} \neq 0)$ | |
	Conduction	Valence	Conduction	Valence
TG/BN	-3, -2, -1, 0	0, 1, 2, 3	-3, -2, -1	0, 1, 2
BG/BN	-1, 0	1, 2	-2, -1, 0	-1, 0, 1
G/BN	-1, 0, 1	0, 1	-1, 0	0, 1

Table 6.3: *Chern number with $C_{AB} \neq 0$ and $C_{AB} = 0$ for the alignment $\xi = \pm 1$*
.

Topological properties of non-Hermitian SSH circuit model

Based on the theoretical development of Chapter 5, we will analyze the topological implications of our circuit model. Initially, we do an analysis of the topological implications of the frequency ω in the the non-Hermitian SSH chain model. Then, we will analyze each of the represented topological properties, such as the topological invariant winding number, the edge states, the skin effect and the bulk-edge correspondence with periodic boundary conditions.

7.1   Relationship between frequency ω and hoppings

As we saw in Section 5.1 the non-Hermitian SSH model depends on the frequency ω. In Figure 7.1, we show the behavior of the hoppings t_{AB} and t_{BA} as a function of ω according to equation (5.12).
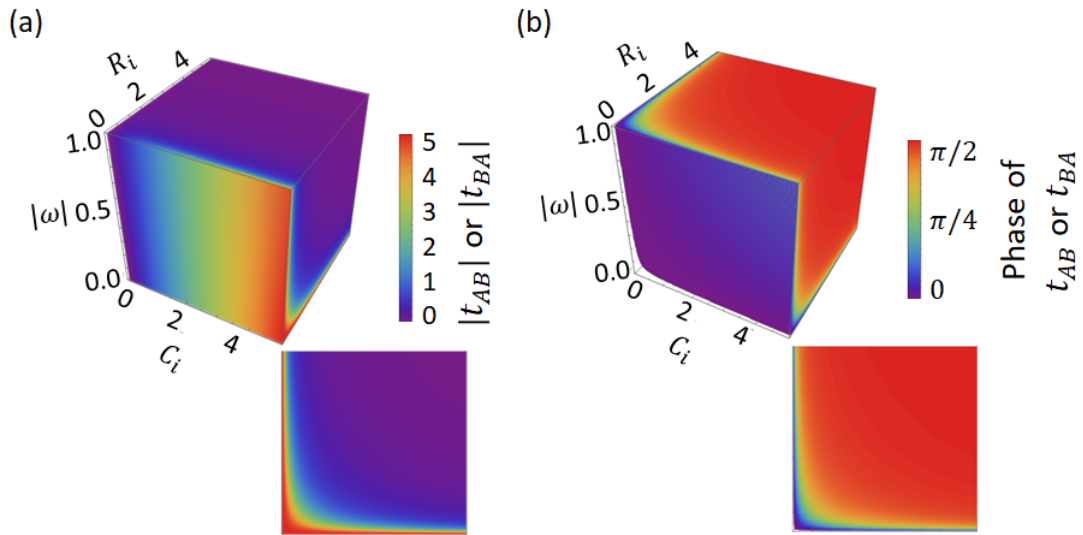
Figure 7.1: *(a) Magnitude and (b) phase of hopping t_{AB} and t_{BA} depending on the values of R_i, C_i and ω. In the lower plane of each figure we show the magnitude and phase in the $R - |\omega|$ plane, respectively.*

It is very interesting that the SSH model of equation (5.9) and its respective solution of $\omega(k)$ in (5.15), has a decay in the magnitude of hoppings t_{AB} and t_{BA} when the frequency ω increases.

An equally interesting aspect is that when R increases the magnitude of t_{AB} and t_{BA} decreases, however, the hoppings rapidly acquire a phase that tends to $\pi/2$. Our model also shows that, for ω close to zero and small values of R_i (compared to capacitance), the behavior of t_{AB} and t_{BA} hoppings is similar to an Hermitian SSH system.

Although (5.11) is true for natural oscillation modes, hopping exhibits a continuum in complex space and $\omega = \omega_R + i\omega_I$ due to freedom in choosing the circuit parameters. In figure 7.2 it is clear that when $\omega \to \infty$, the magnitude of hoppings t_{AB} and t_{BA} tend to zero asymptotically [140]. In the left panel it is observed that when $\omega_I = \text{Im}(\omega) \to -1$ and also $\omega_R = \text{Re}(\omega) \to 0$ the magnitude of the hopping tends to infinity.
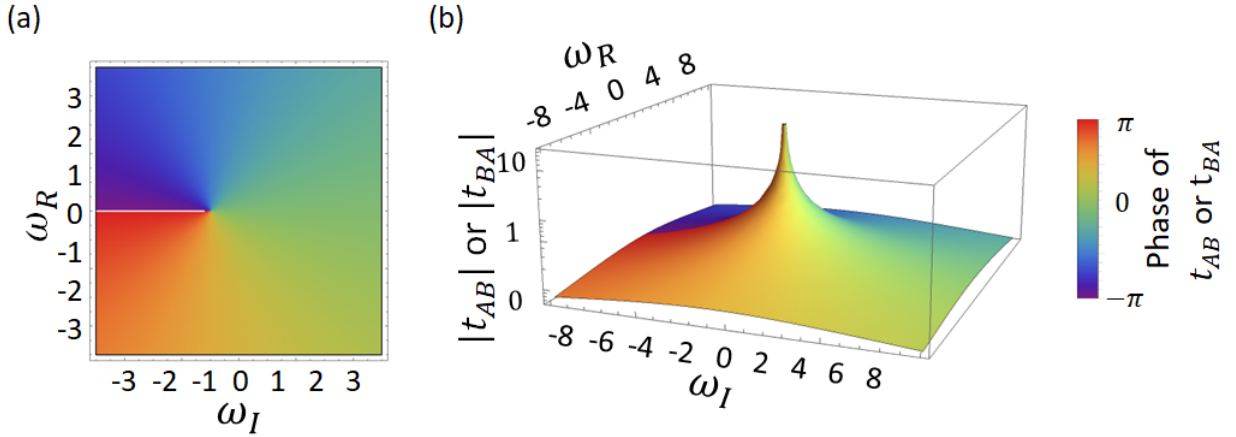

Figure 7.2: *Magnitude (right) and phase (left) of hoppings t_{AB} and t_{BA} as a function of the frequency $\omega = \omega_R + i\omega_I$.*

7.2 Non-Hermitian SSH system topology

A dissipative topolectric model can have real or complex admittance spectra for normal oscillation modes $\omega(k)$. The proposed matrix (5.13) allows both spectral types for Λ. Specifically, Λ is real for the four ω solutions for (5.15) and the parameters described Fig. 7.3; whereas Λ's can be complex for the parameters described in Fig. 7.4.

The eigenstates of $\mathcal{Y}(k)$ (see equations (5.11) and (5.13)), are such that notation $\Lambda_i(k)$, $i = 3, 4, 5, 6$ refers to the ω_i solutions of (5.15). Therefore, $\mathcal{Y}(k)|u_l(k)\rangle = \Lambda_{i,l}(k)|u_l(k)\rangle$, with $l = 1, 2, \cdots, 2N$ where $|\psi_l(k)\rangle = |k\rangle \otimes |u_l(k)\rangle$ with $|u_l(k)\rangle = a_l(k)|A\rangle + b_l(k)|B\rangle$. For a chain of N unit cells, we can write the following eigenvalue equation

$$
\begin{pmatrix}
0 & t_{AB} & 0 & 0 & \cdots & 0 & t_{BA} \\
t_{AB} & 0 & t_{BA} & 0 & \cdots & 0 & 0 \\
0 & t_{BA} & 0 & t_{AB} & \cdots & 0 & 0 \\
\vdots & \vdots & \vdots & \vdots & \vdots & \vdots & \vdots \\
t_{BA} & 0 & 0 & t_{AB} & \cdots & t_{AB} & 0
\end{pmatrix}
\begin{bmatrix}
a(k)e^{ik} \\
b(k)e^{ik} \\
a(k)e^{2ik} \\
b(k)e^{2ik} \\
\vdots \\
a(k)e^{Nik} \\
b(k)e^{Nik}
\end{bmatrix}
= \Lambda(k)
\begin{bmatrix}
a(k)e^{ik} \\
b(k)e^{ik} \\
a(k)e^{2ik} \\
b(k)e^{2ik} \\
\vdots \\
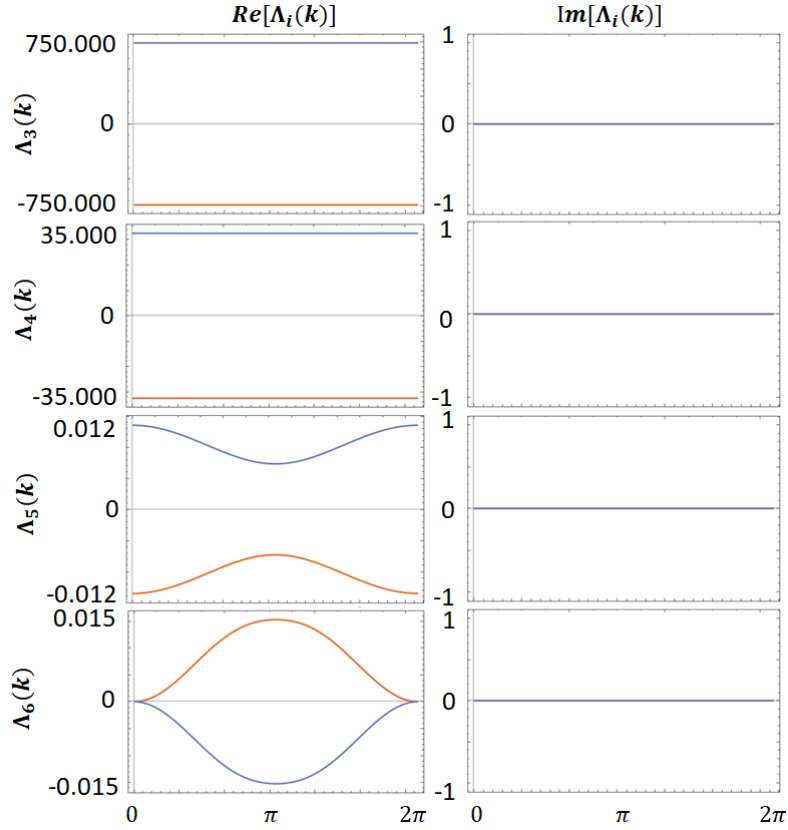a(k)e^{Nik} \\
b(k)e^{Nik}
\end{bmatrix}.
\tag{7.1}
$$

Figure 7.3: *Real eigenvalues $\Lambda(k)$ from equation (5.11) for each solution of ω with parameters $R_1 = 82.4$, $R_2 = 17.3$, $C_1 = 17.3$, $C_2 = 17.3$ and $L = 1.4$.*

Next, we show that our RLC model fits well enough to theoretical topological models. For example, Fu [141] proposed a model that comprising a binary waveguide array with alternating real and imaginary couplings, hence t_{AB} is imaginary ($R_1 \gg C_1$) and t_{BA} is real ($R_2 \to 0$) in our RLC circuit model. The physical model proposed by Pocock *et al.* [124] and subsequently Lieu [142] can also be adjusted to our proposed circuital model results. The non-Hermitian physical models for complex hopping that they analyzed, exhibited bulk-edge correspondence when the next nearest neighbor was zero, i.e., the Hamiltonian diagonal was zero, for any t_{AB} and t_{BA} magnitude and phase. Next, we will delve into the topological properties of our model.

7.2.1 Topological Winding number and protected edge states

Next, we will talk about the winding number in the non-Hermitian SSH model that we have presented here. If we write $\mathcal{Y}(k)$ as a two band non-Hermitian system

$$\mathcal{Y}(k) = h_x\sigma_x + h_y\sigma_y = \left(-\frac{C_1}{\eta_1} - \frac{C_2}{\eta_2}\cos k\right)\sigma_x + \frac{C_2}{\eta_2}\sin k\sigma_y \qquad (7.2)$$

then we can prove that our model has chiral symmetry, which implies that k varies from 0 to 2π
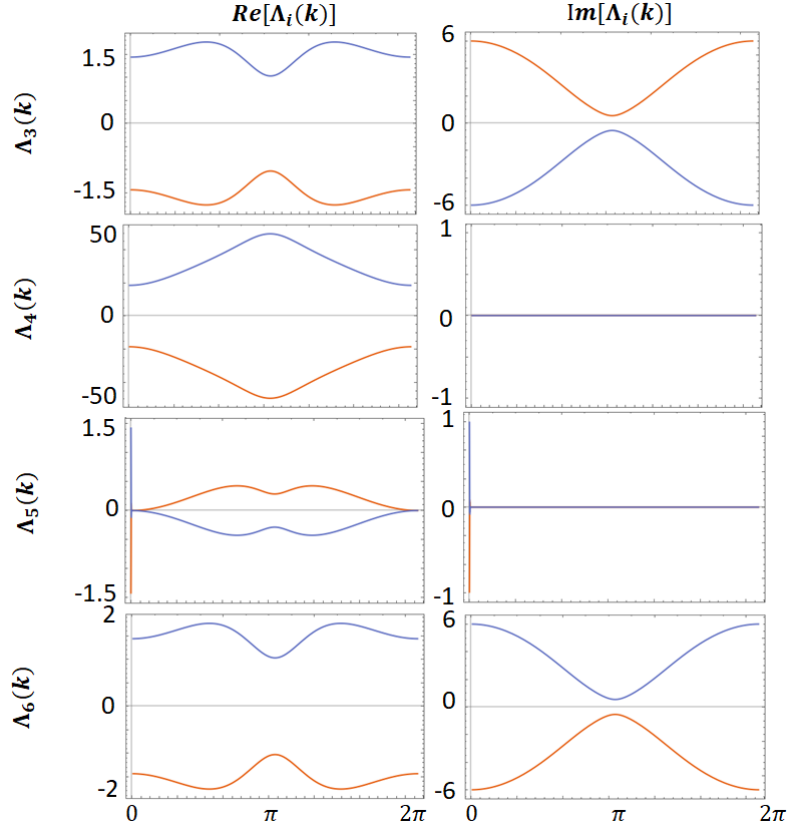
Figure 7.4: *Complex eigenvalues $\Lambda(k)$ from equation (5.11) for each solution of ω with parameters $R_1 = 3.2$, $R_2 = 2.6$, $C_1 = 3.4$, $C_2 = 3.1$ and $L = 2.7$.*

in a closed loop. Indeed

$$
\begin{aligned}
\sigma_z \mathcal{Y}(k)\sigma_z &= \sigma_z \left(\left(-\frac{C_1}{\eta_1} - \frac{C_2}{\eta_2} \cos k \right) \sigma_x + \frac{C_2}{\eta_2} \sin k \sigma_y \right) \sigma_z \\
&= \left(\frac{C_1}{\eta_1} + \frac{C_2}{\eta_2} \cos k \right) \sigma_x - \frac{C_2}{\eta_2} \sin k \sigma_y \\
&= -\mathcal{Y}(k).
\end{aligned}
\tag{7.3}
$$

According equation (2.37), the winding number can be expressed as

$$
\mu = \frac{1}{2\pi} \int_0^{2\pi} dk \frac{\mathcal{Y}_x \partial_k \mathcal{Y}_y - \mathcal{Y}_y \partial_k \mathcal{Y}_x}{\mathcal{Y}_x^2 + \mathcal{Y}_y^2},
\tag{7.4}
$$

where there is a winding number for each family of normal oscillation frequencies ω_i.

We simulate 600 random R_1, R_2, C_1, C_2 and L parameters. For each set of parameters, we compute the evaluated winding number in the allowed solutions of ω. Table 7.1 shows example winding numbers for a particular parameter set.

The percentage distribution of winding numbers in each solution of ω is shown in Figure 7.5. We are surprised that solutions ω_3 and ω_6 have similar winding number distribution. On the other hand, solution ω_5 seems to have a high probability of having winding numbers with values 0 or 1. Solution ω_4 is also interesting because the probability of obtaining a value of 0 or 1 or one other than these two is practically the same. The study of these probabilities is a valuable source of

Table 7.1: *Circuit parameters with respective winding numbers for each solution $\omega_i(k)$.*

$R_1\ [\Omega]$	$R_2\ [\Omega]$	$C_1\ [F]$	$C_2\ [F]$	$L\ [H]$	μ_3	μ_4	μ_5	μ_6
1.34	0.17	0.95	0.45	0.81	-1	1	1	0
0.03	0.14	1.50	0.26	0.57	0	0	2	0
1.45	0.14	0.22	0.54	1.11	1	0	0	1
0.05	1.41	0.03	1.34	1.17	2	1	-1	0

study for further developments related to machine learning [143].
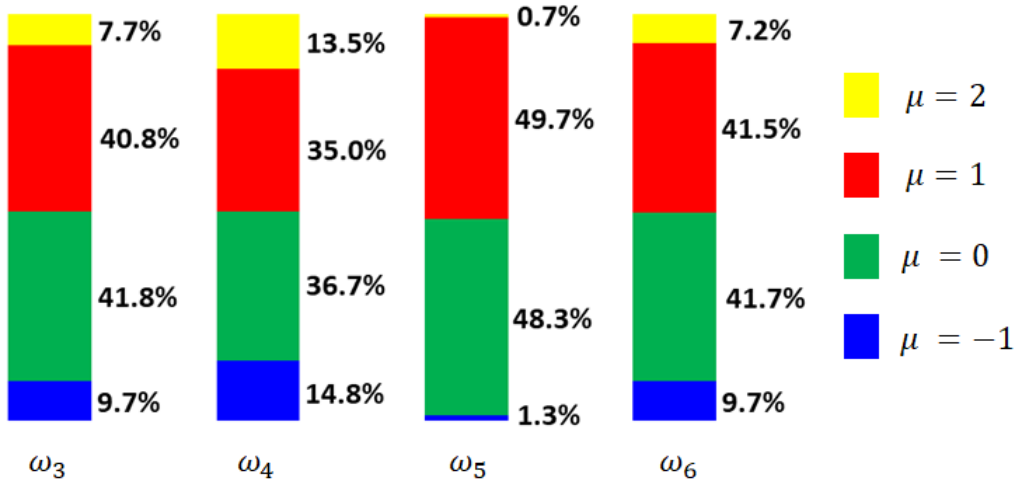

Figure 7.5: *Percentage distribution of the winding number for each solution of ω, from the random selection of 600 parameters.*

Yin *et al.* introduced the complex angle $\tan\phi = \mathcal{Y}_y/\mathcal{Y}_x$ to calculate the winding number in non-Hermitian systems, where ϕ can be decomposed as $\phi = \phi_r + i\phi_i$ and only ϕ_r affects the winding number. Thus,

$$\phi_r = \mathrm{Re}\left[\tan^{-1}\left(-\frac{t_{BA}\sin k}{t_{AB} + t_{BA}\cos k}\right)\right] \tag{7.5}$$

for the system proposed here.

In particular, exceptional point in the real parts of $\mathcal{Y}_x$ and $\mathcal{Y}_y$ occur at $(0,0)$ and $\frac{1}{2\pi}\oint \partial_k\phi_r dk$ takes integer multiples of 2π, which implies that the winding numbers are integers. Hence we obtain four possible values for the winding number for each normal oscillation frequency: $\mu = \{-1, 0, 1, 2\}$, as shown in Fig. 7.6 by trajectories in the plane $\mathrm{Re}[\mathcal{Y}_x]$, $\mathrm{Re}[\mathcal{Y}_y]$ around the exceptional point.

Physical meanings for $\mu = 0$ (trivial) and $\mu = 1$ (topological) in a non-Hermitian SSH model are described elsewhere [81, 140, 144], but we briefly winding numbers $\mu = -1$ and $\mu = 2$.

The winding number in a 1D topological system characterizes topological properties for the $\mathcal{Z}$ class, which is related to the quantized Zak phase. Therefore, a negative winding number ($\mu = -1$) represents a skew polarization [145], i.e., occupied bands are negatively polarized, and hence the admittance matrix winds once in a clockwise direction (considering positive as meaning counterclockwise), as shown in Fig. 7.6(c). On the other hand, winding number $\mu = 2$ is related to a topological phase in the SSH model with non-negligible long range hoppings [146] that connects

sites within the same sublattice, preserving chiral symmetry and allowing edge states.

Matrix $\mathcal{Y}(k)$ represents a non-Hermitian chiral-symmetric system [147], which implies bulk-edge correspondence [148]. We have shown above that the proposed circuit model's admittance matrix adequately represents non-Hermitian SSH system properties. Therefore, non-Hermitian SSH model hopping properties are preserved in the circuit model by hypothetical hopping electrical charge on the capacitors.

Numerical simulations verified that (5.15) generates integer winding numbers characteristic of an extended non-Hermitian SSH model for certain parameters (see Table 7.1). Since ω is a function of k and the circuit parameters, the function is difficult to simplify or generalize, and hence so are the hoppings, since they are a function of ω.

Normalized eigenfunction magnitude tends to accumulate on the edge for the simulated system in Fig. 7.6 in a topological system ($\mu = 1$ or $\mu = -1$), whereas eigenfunction magnitude tends to zero throughout the chain for an ordinary system ($\mu = 0$). In particular, module absolute value decays slowly into the bulk when $\mu = 2$ [149]. Thus, bulk-edge correspondence relates the boundary system winding number to the number of edge protected states, such that the number of states at each edge $= |\mu|$ [148, 150], as shown in Fig. 7.6(a).

Bulk-boundary correspondence shown in Fig. 7.6 is justified from previous studies [81, 151] where the winding number is a topological invariant that characterizes chirality at the exceptional points.
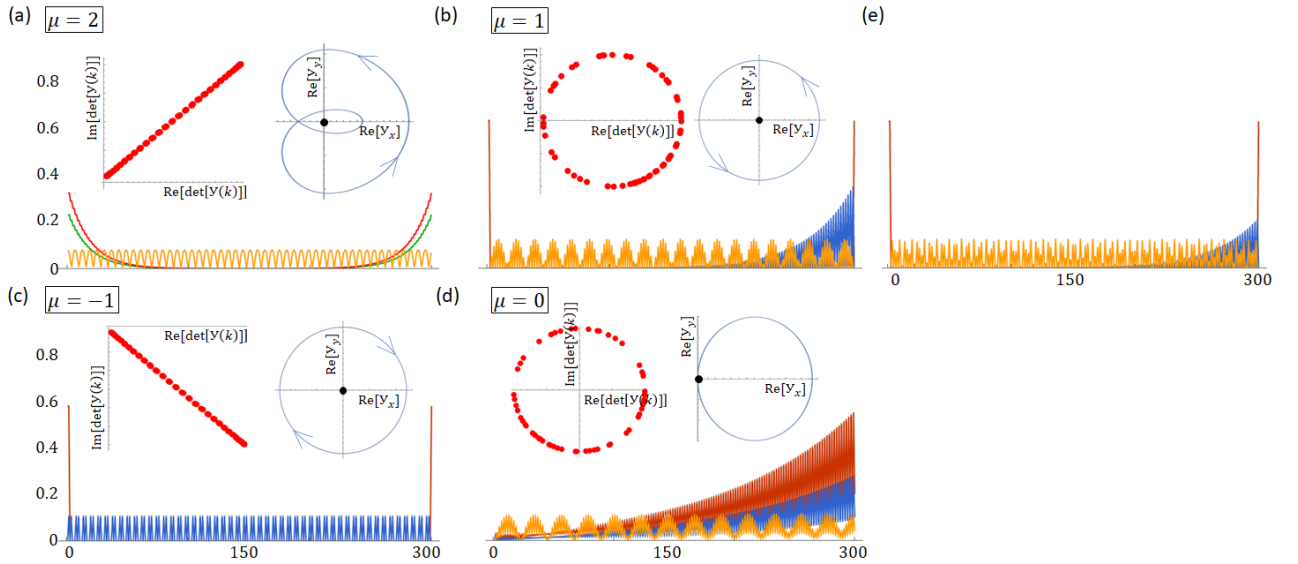
Figure 7.6: *Eigenvector magnitude for the parameter set from Table 7.1, row 4. Each figure shows the admittance matrix determinant for skin effect existence and the trajectory (clockwise or counterclockwise) around the exception point for the real part of $\mathcal{Y}(k)$ to determine the winding number. (a)–(d) show low-energy states, but only (a)–(c) have topological edges states and (b) and (d) show skin effect. (e) shows the counterpart of (b) with small perturbations in some elements of the circuit around the middle of the chain, where the states of the topological edge (red) remain stable while the Bloch states (yellow) and the skin effect (blue) are disturbed.*

7.2.2 Topological skin effect

The skin effect is manifested in the location of the bulk eigenstates that crowd the boundaries for non-reciprocal tight binding lattices with open edges [152], and this non-Hermitian topological effect can be evaluated on the complex plane [153, 154], as we will explain below. By evaluating

$$w(E_0) = \frac{1}{2\pi i} \int_0^{2\pi} dk \frac{d}{dk} \log \det[\mathcal{Y}(k) - E_0], \tag{7.6}$$

the concept can be better understood [153, 154], where k is the momentum and E_0 is any point on the complex energy plane. The non-Hermitian skin effect exists if and only if there is E_0 in the complex energy plane, such that $w(E_0) \neq 0$. Because the trajectory of k from 0 to 2π in the complex plane of $\det[\mathcal{Y}(k) - E_0]$ is a closed curve, then $w(E_0) \neq 0$ if the trajectory does not collapse into an arc or a line, that is, the closed curve has a finite area. In our system, considering the chiral symmetry of the non-Hermitian admittance matrix $\mathcal{Y}$, it is equivalent and convenient to study directly the trajectory of $\det[\mathcal{Y}(k)]$ in the complex plane.

Figure 7.6 clearly shows the skin effect for some solutions of natural frequency in the system with 300 sites and the other parameters as shown in Table 7.1, row 4. The absence or presence of skin effect clearly corroborates with such theoretical prediction. Note that skin states, even if located towards the edges, are distinguished from edge states. To this end, in Figure 7.6(e) we slightly modify the effective jumps t_{AB} and t_{BA} by 5% at the three sites in the center of the chain compared to the case in Figure 7.6(b). While Bloch and especially the blue skin states are altered, the red edge topological state remains stable. This is because the edge states, thanks to the massive edge matching topological protection, are stable against small disturbances. On the other hand, while the existence of the skin effect has a different topological origin, the state of the individual skin is not robust against such disturbances.

Considering 1D non-Hermitian admittance matrix $\mathcal{Y}$ chiral symmetry, $\det[\mathcal{Y}(k)]$ trajectory in the complex plane varies from 0 to 2π. If the closed curve has finite interior area, then there is a skin effect in the system; otherwise the system has no skin effect, i.e., if $\det[\mathcal{Y}(k)]$ collapses in a line. Figure 7.6 shows the skin effect for a system with 300 sites and the other parameters as shown Table 7.1, row 4 occurs for some natural frequency solutions.

Chapter 8

Papers and events

8.1 Paper I

In this work, topological insulators are considered as materials for the development of spintronic devices. First a all, we introduce topological insulator term and we explain its associated properties. Subsequently, the concepts of spin currents on which spintronics is based are studied, then we show some theoretical and experimental developments that have been carried out with the topological insulators. Finally, there is an overview of the challenges and opportunities for the future.

8.2 Paper II

Rhombohedral $N = 3$ trilayer graphene on hexagonal boron nitride (TLG/BN) hosts gate-tunable, valley-contrasting, nearly flat topological bands that can trigger spontaneous quantum Hall phases under appropriate conditions of the valley and spin polarization. Recent experiments have shown signatures of $C = 2$ valley Chern bands at 1/4 hole filling, in contrast to the predicted value of $C = 3$. We discuss the low-energy model for rhombohedral N-layer graphene ($N = 1, 2, 3$) aligned with hexagonal boron nitride (hBN) subject to off-diagonal moire vector potential terms that can alter the valley Chern numbers. Our analysis suggests that topological phase transitions of the flat bands can be triggered by pseudomagnetic vector field potentials associated to moire strain patterns, and that a nematic order with broken rotational symmetry can lead to valley Chern numbers that are in agreement with recent Hall conductivity observations.

8.3 Paper III

"Topological circuit of a versatile non-Hermitian quantum system". Published in **SCIENCE CHINA Physics, Mechanics & Astronomy, DOI: 10.1007/s11433-021-1783-3**

http://engine.scichina.com/doi/10.1007/s11433-021-1783-3

We propose an RLC electrical circuit to theoretically analyse and fully simulate a new type of non-Hermitian Su-Schrieffer-Heeger (SSH) model with complex hoppings. We formulate its construction and investigate its properties by taking the advantage of the circuit's versatility. Rich physical properties can be identified in this system from the normal modes of oscillation of the RLC circuit, including the highly tunable bulk-edge correspondence between topological winding numbers and edge states and even the non-Hermitian skin phenomenon originated from a novel complex energy plane topology. The present study is able to show the wide and appealing possibility of electric circuits in exploring topological physics and is readily generalizable to a plenty of both Hermitian and non-Hermitian nontrivial systems.

8.4 Event I

Name of the event: APS March Meeting 2021
Event date: March 15 - 19, 2021.
Host country: United States
Talk name: Topological phases in N-layer ABC-graphene boron-nitride moire superlattices
Talk date: March 16, 2021
More information in:

- https://meetings.aps.org/Meeting/MAR21/Session/E46.7

- http://meetings.aps.org/Meeting/MAR21/APS_epitome

8.5 Event II

Name of the event: 2021 KPS Spring Meeting
Event date: April 21 - 23, 2021.
Host country: South Korea
Talk name: Topological phases in N-layer rhombohedral graphene boron-nitride moire superlattices
Talk date: April 22, 2021
More information in:

- http://www.kps.or.kr/conference/event/content/content.php?_mid=1140,1154

- http://www.kps.or.kr/conference/event/content/program/search_result_abstract.php?id=3185&tid=367

- http://www.kps.or.kr/conference/event/content/program/search_result_session.php?id=367#

Note: This work was selected to participate in the category "Excellent Presentation Prize"

8.6 Event III

Name of the event: I Postgraduate Symposium of the University of Antioquia
Event date: June 15 - 17, 2021
Host country: Colombia
Talk name: Topological circuit of a non-Hermitian quantum system
Talk date: June 15, 2021
More information in:

- https://bit.ly/3iCantI

- https://www.facebook.com/fcenudea/videos/338267381267099

- https://www.facebook.com/fcenudea/photos/a.246666345454728/6186494828138487/

Note: This work was the winner of the first place for best presentation.

Chapter 9

Summary and outlook

Two scientific contributions were presented in this thesis, both related to topological aspects of the subject. The main conclusions and reflections of these works are expressed below.

9.1 About Chern diagrams in N-Layer ABC-graphene boron-nitride moiré superlattices

Regarding topological phases in N-layer ABC-graphene boron-nitride moiré superlattices, the Chern bands are found for either the valence or conduction bands depending on moiré pattern potential [111]. We have verified up to trilayers that, depending on the system parameters the Chern number is defined as $C = N\nu\xi\delta_{\text{sign}(\Delta)\cdot\xi,b}$ (see Section 6).

The Berry curvature hot spots near the mBZ boundaries and trigonal warping band edges are essential for the non-zero and zero Chern numbers. The zero Chern number is due to the exact cancellation of opposite Berry curvatures at mBZ boundaries that to trigonal warping band edges exactly cancel out. And that unequal weights at these band edges gives out the non-zero Chern numbers. The different Chern numbers within the same direction of the electric field with the inclusion of off-diagonal terms can be quantified with the Chern weights at the primary gap (trigonal warping band edges) and the secondary gaps (mBZ boundaries). In previous studies [111], it is considered that the primary Chern weight $w_P \sim \text{sign}(\Delta)b\nu\, N/2$ near each valley whose sign depends on $\text{sign}(\Delta)$, the hole or electron band character $b = \pm 1$, as well as valley $\nu = \pm 1$. On the other hand, due to moire patterns, the K and K' principal valleys are having gaps near the mBZ boundaries with Chern weights $w_S^{e/h}$, where w_S^e or w_S^h are the secondary Chern weights for electron and hole bands.

According to what we explained in Chapter 6, the secondary Chern weight can be altered by the introduction of the off-diagonal interlayer coherent moiré pattern from the magnitude C_{AB} and the phase ϕ_{AB} and this allows to trigger topological phase transitions, like the ones we present in sections 6.1, 6.2 and 6.3.

9.2 About the topological analysis of a circuit representation of a non-Hermitian SSH model

We proposed an electrical circuit model with R, L and C elements that corresponds to a non-Hermitian quantum model similar to SSH with complex hoopings and it is suitable for both

periodic and open boundary conditions. The proposed model is based on natural oscillation frequencies as a function of the circuit parameters, as we explained in chapters 5 and 7.

Our circuit model, accurately exhibits several interesting topological properties, such as integer winding number, bulk-edge correspondence, and non-Hermitian skin effect. Therefore, the current study on topolectric circuits exemplifies a promising path that relies on the correspondence between readily available electrical circuits and the modeling of topological phenomena in quantum systems.

One of the advantages of the model is that the intra and inter site hoppings can be configured independently, unlike other similar models. This allows high versatility and the theoretical and experimental development of new topological properties.

We worked with a non-Hermitian system with complex hopping amplitudes that converges to a Hermitian system when the resistance disappears. Complex hopping is very useful to help understand different physical phenomena in non-Hermitian systems [124, 126]. The circuit that we propose here provides a useful tool to analyze such systems and will serve to develop more interesting circuits that allow exploring non-Hermitian phenomena.

The existence of the winding number in our model is guaranteed by the existence of chiral symmetry, however, the non-Hermiticity generates novel winding numbers ($\mu = -1$ and $\mu = 2$) that preserve the bulk-edge correspondence. With our model we have found topological ($\mu = 1$) and trivial ($\mu = 0$) configurations, however, other configurations have appeared that produce novel winding numbers. Specifically, for $\mu = -1$ the zero-state densities accumulate at the edge while at bulk it is zero. When $\mu = 2$ the magnitude of the wavefunction decays slowly towards the center of the bulk.

Bibliography

[1] Joseph John Thomson, *A Treatise on the Motion of Vortex Rings - An Essay to Which the Adams Prize was Adjudged in 1882, in the University of Cambridge.* London: Macmillan, 1883.

[2] J. C. Maxwell, "L. On hills and dales," *The London, Edinburgh, and Dublin Philosophical Magazine and Journal of Science*, vol. 40, no. 269, pp. 421–427, 12 1870. [Online]. Available: https://www.tandfonline.com/doi/full/10.1080/14786447008640422

[3] M. Epple, "Topology, Matter, and Space, I: Topological Notions in 19th-Century Natural Philosophy," *Archive for History of Exact Sciences*, vol. 52, no. 4, pp. 297–392, 2 1998. [Online]. Available: http://link.springer.com/10.1007/s004070050019

[4] E. H. Hall, "On a New Action of the Magnet on Electric Currents," *American Journal of Mathematics*, vol. 2, no. 3, p. 287, 9 1879. [Online]. Available: https://www.jstor.org/stable/2369245?origin=crossref

[5] K. v. Klitzing, G. Dorda, and M. Pepper, "New Method for High-Accuracy Determination of the Fine-Structure Constant Based on Quantized Hall Resistance," *Physical Review Letters*, vol. 45, no. 6, pp. 494–497, 8 1980. [Online]. Available: https://link.aps.org/doi/10.1103/PhysRevLett.45.494

[6] R. B. Laughlin, "Anomalous Quantum Hall Effect: An Incompressible Quantum Fluid with Fractionally Charged Excitations," *Physical Review Letters*, vol. 50, no. 18, pp. 1395–1398, 5 1983. [Online]. Available: https://link.aps.org/doi/10.1103/PhysRevLett.50.1395

[7] D. J. Thouless, M. Kohmoto, M. P. Nightingale, and M. den Nijs, "Quantized Hall Conductance in a Two-Dimensional Periodic Potential," *Physical Review Letters*, vol. 49, no. 6, pp. 405–408, 8 1982. [Online]. Available: https://link.aps.org/doi/10.1103/PhysRevLett.49.405

[8] H. Lohani, P. Mishra, A. Banerjee, K. Majhi, R. Ganesan, U. Manju, D. Topwal, P. S. A. Kumar, and B. R. Sekhar, "Band Structure of Topological Insulator BiSbTe1.25Se1.75," *Nat Sci Rep*, vol. 7, no. 4567, 2017. [Online]. Available: http://www.nature.com/articles/s41598-017-04985-y

[9] Y. Xu, I. Miotkowski, C. Liu, J. Tian, H. Nam, N. Alidoust, J. Hu, C. K. Shih, M. Z. Hasan, and Y. P. Chen, "Observation of topological surface state quantum Hall effect in an intrinsic three-dimensional topological insulator," *Nat Phys*, vol. 10, no. 12, pp. 956–963, 11 2014. [Online]. Available: http://www.nature.com/doifinder/10.1038/nphys3140

[10] A. Lau and C. Ortix, "Topological semimetals in the SnTe material class: Nodal lines and Weyl points," *Phys. Rev. Lett.*, vol. 122, no. 186801, pp. 2–4, 2019. [Online]. Available: http://arxiv.org/abs/1804.09574

[11] Y. Ando and L. Fu, "Topological Crystalline Insulators and Topological Superconductors: From Concepts to Materials," *Annu. Rev. Condens. Matter Phys.*, vol. 6, no. 1, pp. 361–381, 2015. [Online]. Available: http://arxiv.org/abs/1501.00531%0Ahttp://dx.doi.org/10.1146/annurev-conmatphys-031214-014501

[12] Y. Tanaka, T. Yokoyama, A. V. Balatsky, and N. Nagaosa, "Topological spin-current in non-centrosymmetric superconductors," *Phys. Rev. B*, vol. 76, no. 6, p. 060505, 2009. [Online]. Available: http://arxiv.org/abs/0806.4639%0Ahttp://dx.doi.org/10.1103/PhysRevB.79.060505

[13] S. Seki and M. Mochizuki, *Skyrmions in Magnetic Materials.* Springer Briefs In Physics, 2016. [Online]. Available: http://link.springer.com/10.1007/978-3-319-24651-2

[14] X.-H. Zhang, X. Li, and J.-B. Hao, "Topological vortices in gauge models of graphene," *Results in Physics*, vol. 9, pp. 636–639, 6 2018. [Online]. Available: https://linkinghub.elsevier.com/retrieve/pii/S2211379718301645

[15] R. Owczarek, "Topological defects in superfluid helium," *International Journal of Theoretical Physics*, vol. 30, no. 12, pp. 1605–1612, 12 1991. [Online]. Available: http://link.springer.com/10.1007/BF00673638

[16] M. Nakahara, *Geometry, Topology and Physics, Second Edition*, 2nd ed. Taylor \& Francis, 2003. [Online]. Available: https://books.google.com.co/books?id=cH-XQB0Ex5wC

[17] S. Lipschutz, *Schaum's outline of theory and problems of general topology*, ser. Springer Series in Statistics. Pennsylvania State University: McGraw-Hill book Company, 1965. [Online]. Available: https://books.google.com.co/books?id=fnTgAAAAMAAJ

[18] M. V. Berry, "Quantal phase factors accompanying adiabatic changes," *Proceedings of the Royal Society of London. A. Mathematical and Physical Sciences*, vol. 392, no. 1802, pp. 45–57, 3 1984. [Online]. Available: https://royalsocietypublishing.org/doi/10.1098/rspa.1984.0023

[19] B. A. Bernevig and T. L. Hughes, *Topological Insulators and Topological Superconductors.* New Jersey: Princeton University Press, 2013.

[20] T. Eguchi, P. B. Gilkey, and A. J. Hanson, "Gravitation, gauge theories and differential geometry," *Physics Reports*, vol. 66, no. 6, pp. 213–393, 12 1980. [Online]. Available: https://linkinghub.elsevier.com/retrieve/pii/0370157380901301

[21] M. Z. Hasan and C. L. Kane, "Colloquium : Topological insulators," *Reviews of Modern Physics*, vol. 82, no. 4, pp. 3045–3067, 11 2010. [Online]. Available: https://link.aps.org/doi/10.1103/RevModPhys.82.3045

[22] M. Sigrist, "Solid State Theory," Institut fur Theoretische Physik, Tech. Rep., 2014. [Online]. Available: https://books.google.com.co/books?id=l8pIAwAAQBAJ&lr=&source=gbs_navlinks_s

[23] M. Born and V. Fock, "Beweis des Adiabatensatzes," *Zeitschrift for Physik*, vol. 51, no. 3-4, pp. 165–180, 3 1928. [Online]. Available: http://link.springer.com/10.1007/BF01343193

[24] M. Franz and L. Molenkamp, Eds., *Topological Insulators*, 1st ed. Elsevier, 2013. [Online]. Available: https://linkinghub.elsevier.com/retrieve/pii/B9780444633149000172

[25] Y. A. Bychkov and I. E. Rashba, "Properties of a 2D electron gas with lifted spectral degeneracy," *JETP Letters*, vol. 39, no. 2, pp. 78–83, 1984. [Online]. Available: http://www.jetpletters.ac.ru/ps/1264/article_19121.shtml

[26] H. L. Stormer, Z. Schlesinger, A. Chang, D. C. Tsui, A. C. Gossard, and W. Wiegmann, "Energy Structure and Quantized Hall Effect of Two-Dimensional Holes," *Physical Review Letters*, vol. 51, no. 2, pp. 126–129, 7 1983. [Online]. Available: https://link.aps.org/doi/10.1103/PhysRevLett.51.126

[27] D. Stein, K. V. Klitzing, and G. Weimann, "Electron Spin Resonance on GaAs-Alx Gal-x As Heterostructures," *Physical Review Letters*, vol. 51, no. 2, pp. 130–133, 7 1983. [Online]. Available: https://link.aps.org/doi/10.1103/PhysRevLett.51.130

[28] J. K. Asbóth, L. Oroszlány, and A. Pályi, *A Short Course on Topological Insulators*, ser. Lecture Notes in Physics. Cham: Springer International Publishing, 2016, vol. 919. [Online]. Available: http://link.springer.com/10.1007/978-3-319-25607-8

[29] E. Hall, "XVIII. On the "Rotational Coefficient" in nickel and cobalt," *The London, Edinburgh, and Dublin Philosophical Magazine and Journal of Science*, vol. 12, no. 74, pp. 157–172, 9 1881. [Online]. Available: https://www.tandfonline.com/doi/full/10.1080/14786448108627086

[30] B. I. Halperin, "Quantized Hall conductance, current-carrying edge states, and the existence of extended states in a two-dimensional disordered potential," *Physical Review B*, vol. 25, no. 4, pp. 2185–2190, 2 1982. [Online]. Available: http://link.aps.org/doi/10.1103/PhysRevB.25.2185

[31] F. D. M. Haldane, "Model for a Quantum Hall Effect without Landau Levels: Condensed-Matter Realization of the "Parity Anomaly"," *Physical Review Letters*, vol. 61, no. 18, pp. 2015–2018, 10 1988. [Online]. Available: https://link.aps.org/doi/10.1103/PhysRevLett.61.2015

[32] M. Dyakonov and V. Perel, "Possibility of orienting electron spins with current," *Soviet Journal of Experimental and Theoretical Physics Letters*, vol. 13, no. 11, p. 467, 6 1971. [Online]. Available: http://www.jetpletters.ac.ru/ps/1587/article_24366.shtml

[33] C. L. Kane and E. J. Mele, "Quantum Spin Hall Effect in Graphene," *Physical Review Letters*, vol. 95, no. 22, p. 226801, 11 2005. [Online]. Available: https://link.aps.org/doi/10.1103/PhysRevLett.95.226801

[34] Wayne M. Saslow, *Electricity, Magnetism, and Light.* Elsevier, 2002. [Online]. Available: https://linkinghub.elsevier.com/retrieve/pii/B9780126194555X50001

[35] R. Karplus and J. M. Luttinger, "Hall Effect in Ferromagnetics," *Physical Review*, vol. 95, no. 5, pp. 1154–1160, 9 1954. [Online]. Available: https://link.aps.org/doi/10.1103/PhysRev.95.1154

[36] M.-C. Chang and Q. Niu, "Berry Phase, Hyperorbits, and the Hofstadter Spectrum," *Physical Review Letters*, vol. 75, no. 7, pp. 1348–1351, 8 1995. [Online]. Available: https://link.aps.org/doi/10.1103/PhysRevLett.75.1348

[37] N. Nagaosa, J. Sinova, S. Onoda, A. H. MacDonald, and N. P. Ong, "Anomalous Hall effect," *Reviews of Modern Physics*, vol. 82, no. 2, pp. 1539–1592, 5 2010. [Online]. Available: https://link.aps.org/doi/10.1103/RevModPhys.82.1539

[38] K. S. Novoselov, Z. Jiang, Y. Zhang, S. V. Morozov, H. L. Stormer, U. Zeitler, J. C. Maan, G. S. Boebinger, P. Kim, and A. K. Geim, "Room-Temperature Quantum Hall Effect in Graphene," *Science*, vol. 315, no. 5817, pp. 1379–1379, 3 2007. [Online]. Available: https://www.science.org/doi/10.1126/science.1137201

[39] R. G. Mani, J. H. Smet, K. von Klitzing, V. Narayanamurti, W. B. Johnson, and V. Umansky, "Zero-resistance states induced by electromagnetic-wave excitation in GaAs/AlGaAs heterostructures," *Nature*, vol. 420, no. 6916, pp. 646–650, 12 2002. [Online]. Available: http://www.nature.com/articles/nature01277

[40] A. Tsukazaki, A. Ohtomo, T. Kita, Y. Ohno, H. Ohno, and M. Kawasaki, "Quantum Hall Effect in Polar Oxide Heterostructures," *Science*, vol. 315, no. 5817, pp. 1388–1391, 3 2007. [Online]. Available: https://www.science.org/doi/10.1126/science.1137430

[41] S. Meng, "Integer Quantum Hall Effect," in *Proseminar in Theoretical Physics.* Zurich: Departement Physik ETH Zurich, 2018, p. 25.

[42] D. C. Tsui, H. L. Stormer, and A. C. Gossard, "Two-Dimensional Magnetotransport in the Extreme Quantum Limit," *Physical Review Letters*, vol. 48, no. 22, pp. 1559–1562, 5 1982. [Online]. Available: https://link.aps.org/doi/10.1103/PhysRevLett.48.1559

[43] J. K. Jain, "Composite-fermion approach for the fractional quantum Hall effect," *Physical Review Letters*, vol. 63, no. 2, pp. 199–202, 7 1989. [Online]. Available: https://link.aps.org/doi/10.1103/PhysRevLett.63.199

[44] C.-Z. Chang, J. Zhang, X. Feng, J. Shen, Z. Zhang, M. Guo, K. Li, Y. Ou, P. Wei, L.-L. Wang, Z.-Q. Ji, Y. Feng, S. Ji, X. Chen, J. Jia, X. Dai, Z. Fang, S.-C. Zhang, K. He, Y. Wang, L. Lu, X.-C. Ma, and Q.-K. Xue, "Experimental Observation of the Quantum Anomalous Hall Effect in a Magnetic Topological Insulator," *Science*, vol. 340, no. 6129, pp. 167–170, 4 2013. [Online]. Available: https://www.sciencemag.org/lookup/doi/10.1126/science.1234414

[45] M. Dyakonov and V. Perel, "Current-induced spin orientation of electrons in semiconductors," *Physics Letters A*, vol. 35, no. 6, pp. 459–460, 7 1971. [Online]. Available: https://linkinghub.elsevier.com/retrieve/pii/0375960171901964

[46] S. Murakami, "Dissipationless Quantum Spin Current at Room Temperature," *Science*, vol. 301, no. 5638, pp. 1348–1351, 9 2003. [Online]. Available: https://www.sciencemag.org/lookup/doi/10.1126/science.1087128

[47] J. Sinova, D. Culcer, Q. Niu, N. A. Sinitsyn, T. Jungwirth, and A. H. MacDonald, "Universal Intrinsic Spin Hall Effect," *Physical Review Letters*, vol. 92, no. 12, p. 126603, 3 2004. [Online]. Available: https://link.aps.org/doi/10.1103/PhysRevLett.92.126603

[48] Y. K. Kato, R. C. Myers, A. C. Gossard, and D. D. Awschalom, "Observation of the Spin Hall Effect in Semiconductors," *Science*, vol. 306, no. 5703, pp. 1910–1913, 12 2004. [Online]. Available: https://www.science.org/doi/10.1126/science.1105514

[49] J. Wunderlich, B. Kaestner, J. Sinova, and T. Jungwirth, "Experimental Observation of the Spin-Hall Effect in a Two-Dimensional Spin-Orbit Coupled Semiconductor System," *Physical Review Letters*, vol. 94, no. 4, p. 047204, 2 2005. [Online]. Available: https://link.aps.org/doi/10.1103/PhysRevLett.94.047204

[50] P. Seifert, K. Vaklinova, S. Ganichev, K. Kern, M. Burghard, and A. W. Holleitner, "Spin Hall photoconductance in a three-dimensional topological insulator at room temperature," *Nature Communications*, vol. 9, no. 1, p. 331, 12 2018. [Online]. Available: http://dx.doi.org/10.1038/s41467-017-02671-1http://www.nature.com/articles/s41467-017-02671-1

[51] W.-K. Tse and S. Das Sarma, "Spin Hall Effect in Doped Semiconductor Structures," *Physical Review Letters*, vol. 96, no. 5, p. 056601, 2 2006. [Online]. Available: https://link.aps.org/doi/10.1103/PhysRevLett.96.056601

[52] T. Jungwirth, J. Wunderlich, and K. Olejník, "Spin Hall effect devices," *Nature materials*, vol. 11, no. 5, pp. 382–390, 2012. [Online]. Available: http://arxiv.org/abs/1411.3249

[53] B. A. Bernevig, T. L. Hughes, and S.-C. Zhang, "Quantum Spin Hall Effect and Topological Phase Transition in HgTe Quantum Wells," *Science*, vol. 314, no. 5806, pp. 1757–1761, 12 2006. [Online]. Available: https://www.sciencemag.org/lookup/doi/10.1126/science.1133734

[54] J. Li, R.-L. Chu, J. K. Jain, and S.-Q. Shen, "Topological Anderson Insulator," *Physical Review Letters*, vol. 102, no. 13, p. 136806, 4 2009. [Online]. Available: https://link.aps.org/doi/10.1103/PhysRevLett.102.136806

[55] R. S. K. Mong, A. M. Essin, and J. E. Moore, "Antiferromagnetic topological insulators," *Physical Review B*, vol. 81, no. 24, p. 245209, 6 2010. [Online]. Available: https://link.aps.org/doi/10.1103/PhysRevB.81.245209

[56] L. Landau, "The Theory of Phase Transitions," *Nature*, vol. 138, no. 3498, pp. 840–841, 11 1936. [Online]. Available: http://link.springer.com/10.1007/BF02734715http://www.nature.com/articles/138840a0

[57] X.-G. Wen, "Topological Order: From Long-Range Entangled Quantum Matter to a Unified Origin of Light and Electrons," *ISRN Condensed Matter Physics*, vol. 2013, pp. 1–20, 2013. [Online]. Available: https://www.hindawi.com/archive/2013/198710/

[58] V. Kalmeyer and R. B. Laughlin, "Equivalence of the resonating-valence-bond and fractional quantum Hall states," *Physical Review Letters*, vol. 59, no. 18, pp. 2095–2098, 11 1987. [Online]. Available: https://link.aps.org/doi/10.1103/PhysRevLett.59.2095

[59] X. G. Wen, F. Wilczek, and A. Zee, "Chiral spin states and superconductivity," *Physical Review B*, vol. 39, no. 16, pp. 11 413–11 423, 6 1989. [Online]. Available: https://link.aps.org/doi/10.1103/PhysRevB.39.11413

[60] C.-K. Chiu and A. P. Schnyder, "Classification of reflection-symmetry-protected topological semimetals and nodal superconductors," *Physical Review B*, vol. 90, no. 20, p. 205136, 11 2014. [Online]. Available: https://link.aps.org/doi/10.1103/PhysRevB.90.205136

[61] A. P. Schnyder, *Lecture notes on: Accidental and symmetry-enforced band crossings in topological semimetals*, M. P. Institut, Ed., Stuttgart, Germany, 2018. [Online]. Available: https://www.fkf.mpg.de/6431357/topo_lecture_notes_schnyder_TMS18.pdf

[62] J. Cayssol, "Various probes of Dirac matter: from graphene to topological insulators," *arXiv:1303.5902v1*, no. November, 3 2013. [Online]. Available: http://arxiv.org/abs/1303.5902

[63] S.-Q. Shen, *Topological Insulators*, ser. Springer Series in Solid-State Sciences. Berlin, Heidelberg: Springer Berlin Heidelberg, 2012, vol. 174. [Online]. Available: http://link.springer.com/10.1007/978-3-642-32858-9

[64] S. Ryu, A. P. Schnyder, A. Furusaki, and A. W. W. Ludwig, "Topological insulators and superconductors: tenfold way and dimensional hierarchy," *New Journal of Physics*, vol. 12, no. 6, p. 065010, 6 2010. [Online]. Available: https://iopscience.iop.org/article/10.1088/1367-2630/12/6/065010

[65] R. M. Kaufmann, D. Li, and B. Wehefritz-Kaufmann, "Notes on topological insulators," *Reviews in Mathematical Physics*, vol. 28, no. 10, p. 1630003, 11 2016. [Online]. Available: https://www.worldscientific.com/doi/abs/10.1142/S0129055X1630003X

[66] E. Prodan and H. Schulz-Baldes, "Non-commutative odd Chern numbers and topological phases of disordered chiral systems," *Journal of Functional Analysis*, vol. 271, no. 5, pp. 1150–1176, 9 2016. [Online]. Available: http://dx.doi.org/10.1016/j.jfa.2016.06.001

[67] P. M. Chaiki and T. C. Lubensky, "Topological defects," in *Principles of Condensed Matter Physics*. Cambridge University Press, 6 1995, pp. 495–589. [Online]. Available: https://www.cambridge.org/core/product/identifier/CBO9780511813467A099/type/book_part

[68] J. C. Y. Teo and C. L. Kane, "Topological defects and gapless modes in insulators and superconductors," *Physical Review B*, vol. 82, no. 11, p. 115120, 9 2010. [Online]. Available: https://link.aps.org/doi/10.1103/PhysRevB.82.115120

[69] A. Altland and M. R. Zirnbauer, "Nonstandard symmetry classes in mesoscopic normal-superconducting hybrid structures," *Physical Review B*, vol. 55, no. 2, pp. 1142–1161, 1 1997. [Online]. Available: https://link.aps.org/doi/10.1103/PhysRevB.55.1142

[70] C.-K. Chiu, J. C. Teo, A. P. Schnyder, and S. Ryu, "Classification of topological quantum matter with symmetries," *Reviews of Modern Physics*, vol. 88, no. 3, p. 035005, 8 2016. [Online]. Available: https://link.aps.org/doi/10.1103/RevModPhys.88.035005

[71] S. Ryu, A. P. Schnyder, A. Furusaki, and A. W. W. Ludwig, "Topological insulators and superconductors: tenfold way and dimensional hierarchy," *New Journal of Physics*, vol. 12, no. 6, p. 065010, 6 2010. [Online]. Available: https://iopscience.iop.org/article/10.1088/1367-2630/12/6/065010

[72] L. Fu and C. L. Kane, "Time reversal polarization and a Z2 adiabatic spin pump," *Physical Review B*, vol. 74, no. 19, p. 195312, 11 2006. [Online]. Available: https://link.aps.org/doi/10.1103/PhysRevB.74.195312

[73] ——, "Topological insulators with inversion symmetry," *Physical Review B*, vol. 76, no. 4, p. 045302, 7 2007. [Online]. Available: https://link.aps.org/doi/10.1103/PhysRevB.76.045302

[74] A. P. Schnyder, S. Ryu, A. Furusaki, A. W. W. Ludwig, V. Lebedev, and M. Feigel'man, "Classification of Topological Insulators and Superconductors," in *AIP Conference Proceedings*, vol. 1134. AIP, 2009, pp. 10–21. [Online]. Available: http://aip.scitation.org/doi/abs/10.1063/1.3149481

[75] R. Bott, "The periodicity theorem for the classical groups and some of its applications," *Advances in Mathematics*, vol. 4, no. 3, pp. 353–411, 6 1970. [Online]. Available: https://linkinghub.elsevier.com/retrieve/pii/0001870870900307

[76] I. Rotter, "A non-Hermitian Hamilton operator and the physics of open quantum systems," *Journal of Physics A: Mathematical and Theoretical*, vol. 42, no. 15, p. 153001, 4 2009. [Online]. Available: https://iopscience.iop.org/article/10.1088/1751-8113/42/15/153001

[77] W. D. Heiss, "The physics of exceptional points," *Journal of Physics A: Mathematical and Theoretical*, vol. 45, no. 44, p. 444016, 11 2012. [Online]. Available: https://iopscience.iop.org/article/10.1088/1751-8113/45/44/444016

[78] H. Shen, B. Zhen, and L. Fu, "Topological Band Theory for Non-Hermitian Hamiltonians," *Physical Review Letters*, vol. 120, no. 14, p. 146402, 2018. [Online]. Available: https://doi.org/10.1103/PhysRevLett.120.146402

[79] A. Ghatak and T. Das, "New topological invariants in non-Hermitian systems," *Journal of Physics: Condensed Matter*, vol. 31, no. 26, p. 263001, 7 2019. [Online]. Available: https://iopscience.iop.org/article/10.1088/1361-648X/ab11b3

[80] S. Yao, F. Song, and Z. Wang, "Non-Hermitian Chern Bands," *Physical Review Letters*, vol. 121, no. 13, p. 136802, 9 2018. [Online]. Available: https://doi.org/10.1103/PhysRevLett.121.136802https://link.aps.org/doi/10.1103/PhysRevLett.121.136802

[81] C. Yin, H. Jiang, L. Li, R. Lü, and S. Chen, "Geometrical meaning of winding number and its characterization of topological phases in one-dimensional chiral non-Hermitian systems," *Physical Review A*, vol. 97, no. 5, p. 052115, 5 2018. [Online]. Available: https://link.aps.org/doi/10.1103/PhysRevA.97.052115

[82] S.-B. Lee, J. Yang, S. Moon, S.-Y. Lee, J.-B. Shim, S. W. Kim, J.-H. Lee, and K. An, "Observation of an Exceptional Point in a Chaotic Optical Microcavity," *Physical Review Letters*, vol. 103, no. 13, p. 134101, 9 2009. [Online]. Available: https://link.aps.org/doi/10.1103/PhysRevLett.103.134101

[83] A. Guo, G. J. Salamo, D. Duchesne, R. Morandotti, M. Volatier-Ravat, V. Aimez, G. A. Siviloglou, and D. N. Christodoulides, "Observation of PT-Symmetry Breaking in Complex Optical Potentials," *Physical Review Letters*, vol. 103, no. 9, p. 093902, 8 2009. [Online]. Available: https://link.aps.org/doi/10.1103/PhysRevLett.103.093902

[84] C. E. Rüter, K. G. Makris, R. El-Ganainy, D. N. Christodoulides, M. Segev, and D. Kip, "Observation of parity-time symmetry in optics," *Nature Physics*, vol. 6, no. 3, pp. 192–195, 2010. [Online]. Available: http://dx.doi.org/10.1038/nphys1515

[85] S. Konschuh, "Spin-Orbit Coupling Effects From Graphene To Graphite," Ph.D. dissertation, Universität Regensburg, 2011. [Online]. Available: https://d-nb.info/1023276178/34

[86] A. J. Leggett, "Lecture 5 : Graphene : Electronic band structure and Dirac fermions," in *Phys 769: Selected Topics in Condensed Matter Physics*, 2010, pp. 1–12. [Online]. Available: http://web.physics.ucsb.edu/~phys123B/w2015/leggett-lecture.pdf

[87] J.-L. Lado, "Topological electronic phases in graphene," Ph.D. dissertation, University of Santiago de Compostela, 2016. [Online]. Available: http://hdl.handle.net/10347/14927

[88] A. K. Geim and I. V. Grigorieva, "Van der Waals heterostructures," *Nature*, vol. 499, no. 7459, pp. 419–425, 7 2013. [Online]. Available: http://www.nature.com/articles/nature12385

[89] J. Jung, A. M. DaSilva, A. H. MacDonald, and S. Adam, "Origin of band gaps in graphene on hexagonal boron nitride," *Nature Communications*, vol. 6, no. 1, p. 6308, 5 2015. [Online]. Available: http://www.nature.com/articles/ncomms7308

[90] Y. Choi, J. Kemmer, Y. Peng, A. Thomson, H. Arora, R. Polski, Y. Zhang, H. Ren, J. Alicea, G. Refael, F. von Oppen, K. Watanabe, T. Taniguchi, and S. Nadj-Perge, "Electronic correlations in twisted bilayer graphene near the magic angle," *Nature Physics*, vol. 15, no. 11, pp. 1174–1180, 11 2019. [Online]. Available: http://www.nature.com/articles/s41567-019-0606-5

[91] I. Brihuega, P. Mallet, H. González-Herrero, G. Trambly de Laissardière, M. M. Ugeda, L. Magaud, J. M. Gómez-Rodríguez, F. Ynduráin, and J.-Y. Veuillen, "Unraveling the Intrinsic and Robust Nature of van Hove Singularities in Twisted Bilayer Graphene by Scanning Tunneling Microscopy and Theoretical Analysis,"

Physical Review Letters, vol. 109, no. 19, p. 196802, 11 2012. [Online]. Available: https://link.aps.org/doi/10.1103/PhysRevLett.109.196802

[92] J. M. B. Lopes dos Santos, N. M. R. Peres, and A. H. Castro Neto, "Continuum model of the twisted graphene bilayer," *Physical Review B*, vol. 86, no. 15, p. 155449, 10 2012. [Online]. Available: https://link.aps.org/doi/10.1103/PhysRevB.86.155449

[93] R. Bistritzer and A. H. MacDonald, "Moire bands in twisted double-layer graphene," *Proceedings of the National Academy of Sciences*, vol. 108, no. 30, pp. 12 233–12 237, 7 2011. [Online]. Available: http://www.ncbi.nlm.nih.gov/pubmed/21730173

[94] G. Li, A. Luican, J. M. B. Lopes dos Santos, A. H. Castro Neto, A. Reina, J. Kong, and E. Y. Andrei, "Observation of Van Hove singularities in twisted graphene layers," *Nature Physics*, vol. 6, no. 2, pp. 109–113, 2 2010. [Online]. Available: http://www.nature.com/nphys/journal/v6/n2/full/nphys1463.html

[95] J. M. B. Lopes dos Santos, N. M. R. Peres, and A. H. Castro Neto, "Graphene Bilayer with a Twist: Electronic Structure," *Physical Review Letters*, vol. 99, no. 25, p. 256802, 12 2007. [Online]. Available: https://link.aps.org/doi/10.1103/PhysRevLett.99.256802

[96] R. Bistritzer and A. H. MacDonald, "Transport between twisted graphene layers," *Physical Review B*, vol. 81, no. 24, p. 245412, 6 2010. [Online]. Available: https://link.aps.org/doi/10.1103/PhysRevB.81.245412

[97] E. V. Castro, K. S. Novoselov, S. V. Morozov, N. M. R. Peres, J. M. B. L. dos Santos, J. Nilsson, F. Guinea, A. K. Geim, and A. H. C. Neto, "Biased Bilayer Graphene: Semiconductor with a Gap Tunable by the Electric Field Effect," *Physical Review Letters*, vol. 99, no. 21, p. 216802, 11 2007. [Online]. Available: https://link.aps.org/doi/10.1103/PhysRevLett.99.216802

[98] X. Duan, C. Wang, J. C. Shaw, R. Cheng, Y. Chen, H. Li, X. Wu, Y. Tang, Q. Zhang, A. Pan, J. Jiang, R. Yu, Y. Huang, and X. Duan, "Lateral epitaxial growth of two-dimensional layered semiconductor heterojunctions," *Nature Nanotechnology*, vol. 9, no. 12, pp. 1024–1030, 12 2014. [Online]. Available: http://www.nature.com/articles/nnano.2014.222

[99] M. E. Dávila, L. Xian, S. Cahangirov, A. Rubio, and G. Le Lay, "Germanene: a novel two-dimensional germanium allotrope akin to graphene and silicene," *New Journal of Physics*, vol. 16, no. 9, p. 095002, 9 2014. [Online]. Available: https://iopscience.iop.org/article/10.1088/1367-2630/16/9/095002

[100] Y. Gong, J. Lin, X. Wang, G. Shi, S. Lei, Z. Lin, X. Zou, G. Ye, R. Vajtai, B. I. Yakobson, H. Terrones, M. Terrones, B. K. Tay, J. Lou, S. T. Pantelides, Z. Liu, W. Zhou, and P. M. Ajayan, "Vertical and in-plane heterostructures from WS2/MoS2 monolayers," *Nature Materials*, vol. 13, no. 12, pp. 1135–1142, 12 2014. [Online]. Available: http://www.nature.com/articles/nmat4091

[101] C. Huang, S. Wu, A. M. Sanchez, J. J. P. Peters, R. Beanland, J. S. Ross, P. Rivera, W. Yao, D. H. Cobden, and X. Xu, "Lateral heterojunctions within monolayer

MoSe2–WSe2 semiconductors," *Nature Materials*, vol. 13, no. 12, pp. 1096–1101, 12 2014. [Online]. Available: http://www.nature.com/articles/nmat4064

[102] G. Chen, A. L. Sharpe, E. J. Fox, Y.-H. Zhang, S. Wang, L. Jiang, B. Lyu, H. Li, K. Watanabe, T. Taniguchi, Z. Shi, T. Senthil, D. Goldhaber-Gordon, Y. Zhang, and F. Wang, "Tunable correlated Chern insulator and ferromagnetism in a moiré superlattice," *Nature*, vol. 579, no. 7797, pp. 56–61, 3 2020. [Online]. Available: http://www.nature.com/articles/s41586-020-2049-7

[103] Y.-H. Zhang, D. Mao, Y. Cao, P. Jarillo-Herrero, and T. Senthil, "Nearly flat Chern bands in moiré superlattices," *Physical Review B*, vol. 99, no. 7, p. 075127, 2 2019. [Online]. Available: https://link.aps.org/doi/10.1103/PhysRevB.99.075127

[104] W. A. de Heer, C. Berger, X. Wu, M. Sprinkle, Y. Hu, M. Ruan, J. A. Stroscio, P. N. First, R. Haddon, B. Piot, C. Faugeras, M. Potemski, and J.-S. Moon, "Epitaxial graphene electronic structure and transport," *Journal of Physics D: Applied Physics*, vol. 43, no. 37, p. 374007, 9 2010. [Online]. Available: https://iopscience.iop.org/article/10.1088/0022-3727/43/37/374007

[105] A. Varykhalov, J. Sánchez-Barriga, A. M. Shikin, C. Biswas, E. Vescovo, A. Rybkin, D. Marchenko, and O. Rader, "Electronic and Magnetic Properties of Quasifreestanding Graphene on Ni," *Physical Review Letters*, vol. 101, no. 15, p. 157601, 10 2008. [Online]. Available: https://link.aps.org/doi/10.1103/PhysRevLett.101.157601

[106] S. Das Sarma, S. Adam, E. H. Hwang, and E. Rossi, "Electronic transport in two-dimensional graphene," *Reviews of Modern Physics*, vol. 83, no. 2, pp. 407–470, 5 2011. [Online]. Available: https://link.aps.org/doi/10.1103/RevModPhys.83.407

[107] J. C. W. Song, P. Samutpraphoot, and L. S. Levitov, "Topological Bloch bands in graphene superlattices," *Proceedings of the National Academy of Sciences*, vol. 112, no. 35, pp. 10 879–10 883, 9 2015. [Online]. Available: http://www.pnas.org/lookup/doi/10.1073/pnas.1424760112

[108] Y.-H. Zhang, D. Mao, and T. Senthil, "Twisted bilayer graphene aligned with hexagonal boron nitride: Anomalous Hall effect and a lattice model," *Physical Review Research*, vol. 1, no. 3, p. 033126, 11 2019. [Online]. Available: https://link.aps.org/doi/10.1103/PhysRevResearch.1.033126

[109] M. Koshino, "Band structure and topological properties of twisted double bilayer graphene," *Physical Review B*, vol. 99, no. 23, p. 235406, 6 2019. [Online]. Available: https://link.aps.org/doi/10.1103/PhysRevB.99.235406

[110] M. Yankowitz, S. Chen, H. Polshyn, Y. Zhang, K. Watanabe, T. Taniguchi, D. Graf, A. F. Young, and C. R. Dean, "Tuning superconductivity in twisted bilayer graphene," *Science*, vol. 363, no. 6431, pp. 1059–1064, 3 2019. [Online]. Available: https://www.sciencemag.org/lookup/doi/10.1126/science.aav1910

[111] B. L. Chittari, G. Chen, Y. Zhang, F. Wang, and J. Jung, "Gate-Tunable Topological Flat Bands in Trilayer Graphene Boron-Nitride Moiré Superlattices," *Physical Review Letters*, vol. 122, no. 1, p. 016401, 1 2019. [Online]. Available: https://link.aps.org/doi/10.1103/PhysRevLett.122.016401

[112] J. R. Wallbank, *Electronic Properties of Graphene Heterostructures with Hexagonal Crystals*, ser. Springer Theses. Cham: Springer International Publishing, 2014. [Online]. Available: http://link.springer.com/10.1007/978-3-319-07722-2

[113] J. R. Wallbank, A. A. Patel, M. Mucha-Kruczyński, A. K. Geim, and V. I. Fal'ko, "Generic miniband structure of graphene on a hexagonal substrate," *Physical Review B*, vol. 87, no. 24, p. 245408, 6 2013. [Online]. Available: https://link.aps.org/doi/10.1103/PhysRevB.87.245408

[114] J. Jung, A. Raoux, Z. Qiao, and A. H. MacDonald, "Ab initio theory of moiré superlattice bands in layered two-dimensional materials," *Physical Review B*, vol. 89, no. 20, p. 205414, 5 2014. [Online]. Available: https://link.aps.org/doi/10.1103/PhysRevB.89.205414

[115] H. Min, *Graphene Nanoelectronics*, ser. NanoScience and Technology, H. Raza, Ed. Berlin, Heidelberg: Springer Berlin Heidelberg, 2012. [Online]. Available: http://link.springer.com/10.1007/978-3-642-22984-8

[116] J. Jung, E. Laksono, A. M. DaSilva, A. H. MacDonald, M. Mucha-Kruczyński, and S. Adam, "Moiré band model and band gaps of graphene on hexagonal boron nitride," *Physical Review B*, vol. 96, no. 8, p. 085442, 8 2017. [Online]. Available: https://link.aps.org/doi/10.1103/PhysRevB.96.085442

[117] J. Jung and A. H. MacDonald, "Accurate tight-binding models for the bands of bilayer graphene," *Physical Review B*, vol. 89, no. 3, p. 035405, 1 2014. [Online]. Available: https://link.aps.org/doi/10.1103/PhysRevB.89.035405

[118] E. McCann and M. Koshino, "The electronic properties of bilayer graphene," *Reports on Progress in Physics*, vol. 76, no. 5, p. 056503, 5 2013. [Online]. Available: https://iopscience.iop.org/article/10.1088/0034-4885/76/5/056503

[119] D. Xiao, M.-C. Chang, and Q. Niu, "Berry phase effects on electronic properties," *Reviews of Modern Physics*, vol. 82, no. 3, pp. 1959–2007, 7 2010. [Online]. Available: https://link.aps.org/doi/10.1103/RevModPhys.82.1959

[120] Y. Yao, L. Kleinman, A. H. MacDonald, J. Sinova, T. Jungwirth, D.-s. Wang, E. Wang, and Q. Niu, "First Principles Calculation of Anomalous Hall Conductivity in Ferromagnetic bcc Fe," *Physical Review Letters*, vol. 92, no. 3, p. 037204, 1 2004. [Online]. Available: https://link.aps.org/doi/10.1103/PhysRevLett.92.037204

[121] Z. Fang, N. Nagaosa, K. S. Takahashi, A. Asamitsu, R. Mathieu, T. Ogasawara, H. Yamada, M. Kawasaki, Y. Tokura, and K. Terakura, "The Anomalous Hall Effect and Magnetic Monopoles in Momentum Space," *Science*, vol. 302, no. 5642, pp. 92–95, 10 2003. [Online]. Available: https://www.science.org/doi/10.1126/science.1089408

[122] W. P. Su, J. R. Schrieffer, and A. J. Heeger, "Soliton excitations in polyacetylene," *Physical Review B*, vol. 22, no. 4, pp. 2099–2111, 8 1980. [Online]. Available: https://link.aps.org/doi/10.1103/PhysRevB.22.2099

[123] D. Xie, W. Gou, T. Xiao, B. Gadway, and B. Yan, "Topological characterizations of an extended Su–Schrieffer–Heeger model," *npj Quantum Information*, vol. 5, no. 1, p. 55, 12 2019. [Online]. Available: http://dx.doi.org/10.1038/s41534-019-0159-6http://www.nature.com/articles/s41534-019-0159-6

[124] S. R. Pocock, P. A. Huidobro, and V. Giannini, "Bulk-edge correspondence and long-range hopping in the topological plasmonic chain," *Nanophotonics*, vol. 8, no. 8, pp. 1337–1347, 4 2019. [Online]. Available: https://www.degruyter.com/view/journals/nanoph/8/8/article-p1337.xml

[125] S. de Léséleuc, V. Lienhard, P. Scholl, D. Barredo, S. Weber, N. Lang, H. P. Büchler, T. Lahaye, and A. Browaeys, "Observation of a symmetry-protected topological phase of interacting bosons with Rydberg atoms," *Science*, vol. 365, no. 6455, pp. 775–780, 8 2019. [Online]. Available: https://www.sciencemag.org/lookup/doi/10.1126/science.aav9105

[126] L. Pickup, H. Sigurdsson, J. Ruostekoski, and P. G. Lagoudakis, "Synthetic band-structure engineering in polariton crystals with non-Hermitian topological phases," *Nature Communications*, vol. 11, no. 1, p. 4431, 12 2020. [Online]. Available: http://dx.doi.org/10.1038/s41467-020-18213-1http://www.nature.com/articles/s41467-020-18213-1

[127] G. Alicata, F. Bagarello, F. Gargano, and S. Spagnolo, "Quantum mechanical settings inspired by RLC circuits," *Journal of Mathematical Physics*, vol. 59, no. 4, p. 042112, 4 2018. [Online]. Available: http://aip.scitation.org/doi/10.1063/1.5026944

[128] E. Zhao, "Topological circuits of inductors and capacitors," *Annals of Physics*, vol. 399, pp. 289–313, 12 2018. [Online]. Available: https://linkinghub.elsevier.com/retrieve/pii/S0003491618302689

[129] C. H. Lee, S. Imhof, C. Berger, F. Bayer, J. Brehm, L. W. Molenkamp, T. Kiessling, and R. Thomale, "Topolectrical Circuits," *Communications Physics*, vol. 1, no. 1, p. 39, 12 2018. [Online]. Available: http://www.nature.com/articles/s42005-018-0035-2

[130] H. Jiang, L.-J. Lang, C. Yang, S.-L. Zhu, and S. Chen, "Interplay of non-Hermitian skin effects and Anderson localization in nonreciprocal quasiperiodic lattices," *Physical Review B*, vol. 100, no. 5, p. 054301, 8 2019. [Online]. Available: https://link.aps.org/doi/10.1103/PhysRevB.100.054301

[131] M. Ezawa, "Electric circuits for non-Hermitian Chern insulators," *Physical Review B*, vol. 100, no. 8, p. 081401, 8 2019. [Online]. Available: https://link.aps.org/doi/10.1103/PhysRevB.100.081401

[132] ——, "Higher-order topological electric circuits and topological corner resonance on the breathing kagome and pyrochlore lattices," *Physical Review B*, vol. 98, no. 20, p. 201402, 11 2018. [Online]. Available: https://link.aps.org/doi/10.1103/PhysRevB.98.201402

[133] T. Helbig, T. Hofmann, C. H. Lee, R. Thomale, S. Imhof, L. W. Molenkamp, and T. Kiessling, "Band structure engineering and reconstruction in electric circuit networks," *Physical Review B*, vol. 99, no. 16, p. 161114, 4 2019. [Online]. Available: https://link.aps.org/doi/10.1103/PhysRevB.99.161114

[134] J. A. Russer and P. Russer, "Lagrangian and Hamiltonian Formulations for Classical and Quantum Circuits," *IFAC Proceedings Volumes*, vol. 45, no. 2, pp. 439–444, 2012. [Online]. Available: https://linkinghub.elsevier.com/retrieve/pii/S1474667016307108

[135] D. Tong, "The quantum Hall effect," Department of Applied Mathematics and Theoretical Physics, Centre for Mathematical Sciences, Cambridge, Tech. Rep., 2016. [Online]. Available: http://www.damtp.cam.ac.uk/user/tong/qhe.html

[136] K. Kumar, *Electric Circuits and Networks*, 1st ed. Pearson Education, 2009.

[137] G. Chen, L. Jiang, S. Wu, B. Lyu, H. Li, B. L. Chittari, K. Watanabe, T. Taniguchi, Z. Shi, J. Jung, Y. Zhang, and F. Wang, "Evidence of a gate-tunable Mott insulator in a trilayer graphene moiré superlattice," *Nature Physics*, vol. 15, no. 3, pp. 237–241, 3 2019. [Online]. Available: http://www.nature.com/articles/s41567-018-0387-2

[138] H. Kim, N. Leconte, B. L. Chittari, K. Watanabe, T. Taniguchi, A. H. MacDonald, J. Jung, and S. Jung, "Accurate Gap Determination in Monolayer and Bilayer Graphene/ h -BN Moiré Superlattices," *Nano Letters*, vol. 18, no. 12, pp. 7732–7741, 12 2018. [Online]. Available: https://pubs.acs.org/doi/10.1021/acs.nanolett.8b03423

[139] S. Javvaji, J. Sun, and J. Jung, "Topological flat bands without magic angles in massive twisted bilayer graphenes," *Physical Review B*, vol. 101, no. 12, p. 125411, 3 2020. [Online]. Available: https://link.aps.org/doi/10.1103/PhysRevB.101.125411

[140] F. Song, S. Yao, and Z. Wang, "Non-Hermitian Skin Effect and Chiral Damping in Open Quantum Systems," *Physical Review Letters*, vol. 123, no. 17, p. 170401, 10 2019. [Online]. Available: https://link.aps.org/doi/10.1103/PhysRevLett.123.170401

[141] Z. Fu, N. Fu, H. Zhang, Z. Wang, D. Zhao, and S. Ke, "Extended SSH Model in Non-Hermitian Waveguides with Alternating Real and Imaginary Couplings," *Applied Sciences*, vol. 10, no. 10, p. 3425, 5 2020. [Online]. Available: https://www.mdpi.com/2076-3417/10/10/3425

[142] S. Lieu, "Topological phases in the non-Hermitian Su-Schrieffer-Heeger model," *Phys. Rev. B*, vol. 97, no. 4, pp. 1–7, 2018.

[143] P. Zhang, H. Shen, and H. Zhai, "Machine Learning Topological Invariants with Neural Networks," *Physical Review Letters*, vol. 120, no. 6, p. 066401, 2 2018. [Online]. Available: https://link.aps.org/doi/10.1103/PhysRevLett.120.066401

[144] C. H. Lee and R. Thomale, "Anatomy of skin modes and topology in non-Hermitian systems," *Physical Review B*, vol. 99, no. 20, p. 201103, 5 2019. [Online]. Available: https://link.aps.org/doi/10.1103/PhysRevB.99.201103

[145] I. Mondragon-Shem, T. L. Hughes, J. Song, and E. Prodan, "Topological Criticality in the Chiral-Symmetric AIII Class at Strong Disorder," *Physical Review Letters*, vol. 113, no. 4, p. 046802, 7 2014. [Online]. Available: https://link.aps.org/doi/10.1103/PhysRevLett.113.046802

[146] B. Perez-Gonzalez, M. Bello, A. Gomez-Leon, and G. Platero, "Interplay between long-range hopping and disorder in topological systems," *Physical Review B*, vol. 99, no. 3, p. 035146, 1 2019. [Online]. Available: https://link.aps.org/doi/10.1103/PhysRevB.99.035146

[147] W. Brzezicki and T. Hyart, "Hidden Chern number in one-dimensional non-Hermitian chiral-symmetric systems," *Physical Review B*, vol. 100, no. 16, p. 161105, 10 2019. [Online]. Available: https://link.aps.org/doi/10.1103/PhysRevB.100.161105

[148] K.-I. Imura and Y. Takane, "Generalized bulk-edge correspondence for non-Hermitian topological systems," *Physical Review B*, vol. 100, no. 16, p. 165430, 10 2019. [Online]. Available: https://link.aps.org/doi/10.1103/PhysRevB.100.165430

[149] B. Perez-Gonzalez, M. Bello, A. Gomez-Leon, and G. Platero, "SSH model with long-range hoppings: topology, driving and disorder," *arXiv:1802.03973 [cond-mat.mes-hall]*, 2 2018. [Online]. Available: http://arxiv.org/abs/1802.03973

[150] M. Maffei, A. Dauphin, F. Cardano, M. Lewenstein, and P. Massignan, "Topological characterization of chiral models through their long time dynamics," *New Journal of Physics*, vol. 20, no. 1, p. 013023, 1 2018. [Online]. Available: https://iopscience.iop.org/article/10.1088/1367-2630/aa9d4c

[151] D. Leykam, K. Y. Bliokh, C. Huang, Y. D. Chong, and F. Nori, "Edge Modes, Degeneracies, and Topological Numbers in Non-Hermitian Systems," *Physical Review Letters*, vol. 118, no. 4, p. 040401, 1 2017. [Online]. Available: https://link.aps.org/doi/10.1103/PhysRevLett.118.040401

[152] V. M. Martinez Alvarez, J. E. Barrios Vargas, M. Berdakin, and L. E. F. Foa Torres, "Topological states of non-Hermitian systems," *The European Physical Journal Special Topics*, vol. 227, no. 12, pp. 1295–1308, 12 2018. [Online]. Available: http://link.springer.com/10.1140/epjst/e2018-800091-5

[153] N. Okuma, K. Kawabata, K. Shiozaki, and M. Sato, "Topological Origin of Non-Hermitian Skin Effects," *Physical Review Letters*, vol. 124, no. 8, p. 086801, 2 2020. [Online]. Available: https://doi.org/10.1103/PhysRevLett.124.086801https://link.aps.org/doi/10.1103/PhysRevLett.124.086801

[154] K. Zhang, Z. Yang, and C. Fang, "Correspondence between Winding Numbers and Skin Modes in Non-Hermitian Systems," *Physical Review Letters*, vol. 125, no. 12, p. 126402, 9 2020. [Online]. Available: https://link.aps.org/doi/10.1103/PhysRevLett.125.126402